PhD thesis

Control Solutions for Multiphase Permanent Magnet Synchronous Machine Drives Applied to Electric Vehicles

Author:
Andres Sierra-Gonzalez

January 9, 2023

Thesis directors:
Edorta Ibarra Basabe
Elena Trancho Olabarri

eman ta zabal zazu

Universidad   Euskal Herriko
del País Vasco   Unibertsitatea

♫"...Cuando escucho un bombo retumbá en la plaza,
me entra un cosquilleo y me traquean los huesos,
pego un güapirreo propio de mi raza,
se me aguan los ojos'e puro sentimiento..." ♪

Fiesta Vieja — Pablo Florez

To my wife, parents, siblings, and nephew. . .

Agradecimientos

En el año 2016, tras sufrir la pronta partida de Caro, juntamos fuerza por ese tristísimo momento y decidimos cruzar el oceano atlántico para cumplir ese anhelo de juventud de hacer un doctorado en el extranjero. Ahora, al acabar la tesis, llega el momento feliz de reconocer a todos aquellos que lo han hecho posible. Quienes me conocen, saben que soy de pocas palabras, pero eso no significa que los sentimientos sean pocos.

Como no podía ser diferente, empiezo agradeciendo a Diana por haberme acompañado en esta aventura, sacrificando tantas cosas y momentos. También quiero gradecer a mi familia grande por ese constante apoyo desde la distancia. En especial a papi, mami, Mafe y Emiliano por el amor, comprensión y alegrías que me han brindado. Igualmente le agradezco mi otra familia, los Ochoa-Tamayo por haberme acogido con tanto cariño. También dejo un agradecimiento a esos amigos que de una forma u otra me han apoyado durante este tiempo.

En un plano ortonormal pero no desacoplado al personal, doy las gracias a mis directores de tesis Edorta Ibarra y Elena Trancho. Sin exagerar, Edorta has sido un oasis en el desierto, sin tu acompañamiento, trabajo hombro a hombro, consejo, protección y un largo etcétera esta tesis no llega a feliz término. Eres un director de tesis único. Elena gracias por haber confiado en mí y acercar esta tesis al mundo de la automoción bizkaina.

Agradezco al centro de investigación Tecnalia por haberme acogido y financiado este proyecto de investigación. En particular, agradezco a todos mis compañeros y excompañeros del área de movilidad sostenible. Agradezco esas voces de aliento, ese interés por el avance, los consejos, las discusiones técnicas y no tan técnicas, puestas a punto de laboratorio, todas esas acciones fueron un gran aporte al trabajo realizado estos años.

Por último y no menos importante, quiero agradecer a los miembros de grupo de investigación APERT de la Universidad del País Vasco por la acogida, acompañamiento y amistad. También quiero reconocer al Programa de Doc-

torado en Electrónica y Telecomunicaciones, en especial a su coordinador José Luis Martin por su constante esfuerzo y rigurosidad para ofrecer un programa con altos estándares de calidad.

<div align="right">

Mila esker,
Many thanks,
Muchas gracias,

</div>

<div align="right">

En Bilbao, Enero de 2023.

</div>

Contents

List of Figures

List of Tables

Abstract

Road transport is one of the main contributors of greenhouse gas emissions. According to the most recent scientific literature, the massive introduction of electric vehicles (EV) is, among other aspects, necessary to effectively mitigate global warming. Therefore, the automotive industry and various national and international government agencies are investing many resources in developing the technologies needed to achieve this goal. Thanks to these efforts, new propulsion systems for EVs are being developed.

Multiphase machines are a promising technology to be included in such novel propulsion systems. They offer several advantages when compared to conventional three-phase machines such as higher power/torque density, fault tolerance, lower torque ripple, and higher efficiency. Among all the available multiphase architectures, dual three-phase permanent magnet synchronous machine (PMSM) drives are mainly selected for EV applications, as the technological transition from three-phase systems is relatively straightforward and their power density is very high. In line with stringent future automotive requirements, the European Union-funded FITGEN project proposes a novel traction solution for next generation EVs. It incorporates a six-phase SiC inverter driving a novel high-speed dual three-phase interior PMSM (IPMSM), which is characterized by its high power density. A dc/dc converter is also included between the battery pack and the power inverter to enable fast dc charging capabilities at high voltage. In order to avoid the utilization of more expensive and less efficient power switches with high blocking voltage values, a cascaded dc-link configuration is adopted for the six-phase inverter.

This thesis is aligned with the aforementioned research project. It aims to design, develop and validate novel control solutions for the dual three-phase drive with cascaded dc-link configuration developed within such project. The controller must provide an accurate torque regulation for a highly coupled dual three-phase topology. Also, the control system must operate at high-speeds (up

to 22.500 rpm) and with switching frequencies up to 24 kHz. Full-speed range operation dealing with high magnetic saturated IPMSM must be also achieved. Finally, the incorporation of an active voltage balancing algorithm is mandatory, due to the nature of the cascaded dc-link configuration.

Taking all the previous into account, a comprehensive analysis and understanding of the mathematical expressions which represent the physical behavior of star-connected n-phase multiphase machines is carried out. This generalized study facilitates the development of accurate electric drive models based on multiphase architectures. In particular, the modeling of multiphase machines in their natural per-phase quantities is presented. Then, this model is simplified through the application of convenient vector transformations. In this part of the thesis, some simulation results are provided for illustrative purposes.

These generalized modeling methodologies are then particularized for automotive symmetrical dual-three phase IPMSM drives, where three modeling approaches are described. The first one represents the drive in its natural per-phase variables, while the rest are based on vector transformations. The *multiphase* model is obtained by applying a six-phase vector transformation that considers the electromagnetic couplings between winding sets. In contrast, the *double three-phase* model is a simplified representation, which is obtained by applying conventional three-phase vector transformations to each three-phase set of the drive. Therefore, three-phase quantities are explicitly represented in the *double three-phase* model. Such models are instrumental, first to assist the design of the novel control solutions proposed in this thesis, and then to perform preliminary simulation validations.

After completing the modeling analysis, three specific vector torque control solutions for symmetrical dual three-phase IPMSMs are presented. First, the *double three-phase* controller allows the independent regulation of the per three-phase set currents. The second one, the *multiphase* controller, allows an accurate torque regulation, as it accounts the effects of electromagnetic coupling between the two three-phase sets of the machine. The last one, named as *hybrid* torque control, is a novel contribution of this thesis. It takes advantage of a novel matrix transformation and combines the vector representations of the other two control solutions to enhance their advantages and overcome their drawbacks. The novel controller incorporates the components required to deal with the particular operating conditions of an automotive drive. For instance, a current set-point generator based on a speed normalization block, a voltage constraint tracking loop and 2D Look-up Tables (LUTs) is presented. This component aims to provide the required current references for accurate torque regulation over the entire speed range, while addressing the high magnetic saturation of

the machine, cross coupling effects and field weakening operation. Also, current regulation loops and modulation algorithms adapted to the dual three-phase scenario are presented.

An accurate mathematical model of the cascaded dc-link configuration for a dual three-phase drive is also presented. Aided by this mathematical representation, a novel active voltage balancing algorithm is developed to operate the drive within the full speed and torque range. Then, this algorithm is incorporated into the *hybrid* and *double three-phase* torque controllers. Simulation results show that the *hybrid* solution is superior to the *double three-phase* one. It is also demonstrated that the incorporation of the balancing algorithm is mandatory for the drive including a cascaded dc-link configuration, as its deactivation leads to instabilities that jeopardize the integrity of the propulsion system.

Finally, the proposed *hybrid* torque control solution with voltage balancing capabilities is experimentally validated. Initially, the proposed controller is integrated in a dSPACE MicroAutoBox II Rapid Control Prototyping (RCP) real-time digital platform. Then, the control system is validated at TRL-6 over a laboratory test bench, incorporating a full-scale prototype with a peak power of 135 kW, developed within the context of the FITGEN project. These initial tests show the need of implementing an interleaved PWM modulation scheme due to the presence of overlapping windings in the machine's stator. After this modification, the controller is extensively tested in the laboratory under various operation profiles, including four driving cycles. Next, the drive prototype is integrated in a real EV, and the novel controller is validated at TRL-7, both in dynamometer and on-road tests. Thanks to this, the industrial applicability of dual three-phase IPMSM drives with cascaded dc-link configuration is assessed, and the proposed control solutions are fully validated for their utilization in real automotive applications.

Abstract

Resumen

El sector transporte es el segundo mayor productor gases de efecto invernadero con un 25 % del total de las emisiones. En particular, el transporte terrestre es el responsable del 77 % de estas emisiones. Según la literatura científica más reciente, la introducción masiva de vehículos eléctricos es, entre otros aspectos, necesaria para mitigar eficazmente el calentamiento global. Por ello, la industria automovilística y diversos organismos gubernamentales nacionales e internacionales están invirtiendo muchos recursos en el desarrollo de las tecnologías necesarias para alcanzar este objetivo. Por ejemplo, entre 2014 y 2020, la Unión Europea ha invertido 3.070 millones de euros en proyectos de investigación destinados a la electrificación del transporte terrestre. Gracias a estos esfuerzos, se están desarrollando nuevos sistemas de propulsión para vehículos eléctricos.

Las máquinas multifásicas son una tecnología prometedora para ser incluida en estos novedosos sistemas de propulsión. Ofrecen varias ventajas en comparación con las máquinas trifásicas convencionales, como son una mayor densidad de potencia/par, tolerancia a fallos, menor rizado del par y mayor eficiencia. Entre todas las arquitecturas multifásicas disponibles, los accionamientos trifásicos-duales basados en máquina síncrona de imanes permanentes (PMSM, por sus iniciales en inglés) son los preferidos para aplicaciones de vehículo eléctrico, ya que la transición tecnológica desde los sistemas trifásicos es relativamente sencilla y su densidad de potencia es muy elevada. Por ejemplo, el uso de dos inversores trifásicos convencionales es una solución directa para alimentar una máquina de seis fases. También desde el punto de vista de sistemas de control, muchas técnicas de control son adaptables de una forma directa a máquinas trifásicas-duales.

Alineado con los exigentes requisitos que tiene la electrificación del transporte para el futuro próximo, el proyecto financiado por la Unión Europea FIT-GEN propone una novedosa solución de tracción para la próxima generación de

vehículos eléctricos. Este sistema de propulsión incorpora un inversor SiC de seis fases que alimenta una novedosa PMSM trifásica-dual de imanes interiores (IPMSM, por sus iniciales en inglés) y alta velocidad, que se caracteriza por su alta densidad de potencia. También se incluye un convertidor de potencia CC/CC entre el módulo de baterías y el inversor. La inclusión de este convertidor habilita la capacidad embebida de carga rápida en CC a alta tensión. Para evitar la utilización de interruptores de potencia más costosos y menos eficientes debido a su mayor valor de tensión de bloqueo, en dicho proyecto se adopta una configuración en cascada para el bus CC en el inversor de seis fases.

Esta tesis se desarrolla en el marco del proyecto de investigación FITGEN. El objetivo de la tesis es diseñar, desarrollar y validar nuevas soluciones de control para el accionamiento trifásico-dual con configuración en cascada desarrollado dentro de dicho proyecto. Este controlador debe proporcionar una regulación precisa del par para una topología trifásica-dual altamente acoplada. Además, el sistema de control debe funcionar a altas velocidades (hasta 22.500 rpm) y con una frecuencia de conmutación de hasta 24 kHz. También debe conseguirse un correcto funcionamiento en todo el rango de velocidad teniendo en cuenta la alta saturación magnética. Por último, la incorporación de un algoritmo de equilibrado activo de tensión es obligatoria, debido a la naturaleza inestable de la configuración en cascada del bus CC.

Teniendo en cuenta todo lo anterior, se lleva a cabo un exhaustivo análisis y comprensión de las expresiones matemáticas que representan el comportamiento físico de las máquinas multifásicas de n-fases conectadas en estrella. Este estudio generalizado facilita el desarrollo de modelos precisos de accionamientos eléctricos basados en arquitecturas multifásicas. En particular, se presenta el modelado de máquinas multifásicas en sus variables naturales por fase. Estos modelos demuestran ser complejos y altamente acoplados, pero facilitan la emulación de la operación postfalta en máquinas multifase. A continuación, este modelo en variables naturales se simplifica mediante la aplicación de transformaciones vectoriales apropiadas. Estas transformaciones se obtienen mediante la multiplicación de dos matrices. La primera de estas matrices es la llamada matriz de desacople, la cual descompone los vectores n-dimensionales (variables por fase) de acuerdo a sus componentes armónicas. La segunda matriz es la llamada matriz de rotación, pues proyecta las componentes armónicas a subespacios que giran a la misma frecuencia de la respectiva componente armónica. Estos modelos vectoriales están desacoplados y sus variables (ficticias) en lugar de ser señales alternas son continuas. La mayor simplicidad de estos modelos los convierte en la mejor alternativa para el diseño de los sistemas de control. Una vez descritos los modelos genéricos, se proporcionan algunos resultados de

simulación particulares con fines ilustrativos.

Estas metodologías de modelado generalizadas se particularizan para accionamientos eléctricos basados en IPMSM trifásicos-duales y simétricos para aplicaciones de automoción. Para este tipo de accionamientos se presentan tres enfoques de modelado. El primero representa el accionamiento en sus variables naturales por fase, mientras que los otros dos utilizan transformaciones vectoriales para representar la máquina de una forma más simple. El modelo vectorial *multifase* se obtiene al aplicar una transformación vectorial de seis fases que tiene en cuenta los acoplamientos electromagnéticos entre los conjuntos trifásicos de bobinados. Este método de modelado descompone la máquina de 6 fases en cuatro subespacios. En el primero se proyectan las componentes fundamentales, en el segundo el quinto y séptimo armónico y en el tercer y cuarto subespacio las componentes de secuencia cero o homopolares. Por otro lado, el modelo *doble trifásico* es una representación vectorial que se obtiene al aplicar transformaciones vectoriales trifásicas convencionales (transformadas de Clarke y Park) a cada conjunto trifásico del accionamiento. Este método de modelado descompone la máquina de 6 fases en cuatro subespacios. En el primero se proyectan las variables relacionadas con el primer conjunto trifásico, en el segundo subespacio las variables de segundo conjunto trifásico y en el tercer y cuarto subespacio las componentes de secuencia cero o homopolares. Por lo tanto, en el modelo *doble trifásico*, las magnitudes trifásicas son explicitas. Estos modelos son fundamentales, en primer lugar, para ayudar al diseño de las novedosas soluciones de control propuestas en esta tesis y, luego, para realizar validaciones preliminares de simulación.

Tras completar el análisis acerca del modelado de la máquina, tres soluciones específicas de control vectorial de par para IPMSMs trifásicos-duales y simétricos son presentadas. En primer lugar, el controlador *doble trifásico* permite el seguimiento independiente de las corrientes de consigna por cada conjunto trifásico. La segunda solución es el controlador *multifásico*. Este permite una regulación precisa del par, ya que tiene en cuenta los efectos del acoplamiento electromagnético entre los dos conjuntos trifásicos de la máquina. El último, denominado control *híbrido* de par, es una aportación novedosa de esta tesis. Este controlador aprovecha una novedosa transformación matricial y combina las otras dos soluciones de control vectorial para potenciar sus ventajas y evitar sus inconvenientes. Este controlador novedoso incorpora los componentes necesarios para hacer frente a las condiciones de funcionamiento particulares de un accionamiento para automoción. Por ejemplo, incluye un generador de consignas de corriente basado en un bloque de normalización de la velocidad, un lazo de seguimiento a las restricciones de tensión del estator (VCT,

25

por sus iniciales en inglés) y tablas de consulta (traducción del término inglés "*look-up table*", abreviado como LUT) de dos dimensiones. El objetivo de este componente es proporcionar las referencias de corriente necesarias para una regulación precisa del par en todo el rango de velocidad, teniendo en cuenta, al mismo tiempo, la alta saturación magnética de la máquina, los efectos de acoplamiento cruzado y la operación en debilitamiento de campo. También se incluyen los lazos de regulación de corriente del estator basados en controladores proporcionales-integrales (PI) que regulan independientemente las corrientes de estator de cada conjunto trifásico. Además, se incluyen los algoritmos de modulación PWM, basados en portadora y con inyección de voltajes de secuencia cero para un mejor aprovechamiento del bus CC, adaptados al escenario trifásico-dual.

También se presenta un modelo matemático de alta precisión del bus CC con configuración en cascada para un accionamiento trifásico-dual. En particular, este modelo representa el comportamiento de las tensiones de entrada de cada inversor trifásico ante cambios en las corrientes de estator de la máquina. El análisis de esta representación matemática muestra una relación no lineal entre las corrientes de estator y las tensiones CC. Con la ayuda de esta representación matemática y el análisis realizado, se desarrolla un novedoso algoritmo de equilibrado activo de tensión. Este algoritmo varía las referencias de corriente en el eje q de cada conjunto trifásico para realizar el equilibrado de tensión, evitando modificar las corrientes relacionadas con el flujo (eje d). Adicionalmente, el algoritmo ajusta su comportamiento considerando si la máquina opera en modo motor o modo generador. Todo esto permite el funcionamiento del conjunto convertidor-máquina en el rango completo de par y velocidad.

Posteriormente, el algoritmo de balanceo se incorpora a los controladores *híbrido* y *doble trifásico* de par y ambos controladores son evaluados mediante simulación. Los resultados de simulación muestran que la solución *híbrida* realiza una regulación más precisa de par que el controlador *doble trifásico* y con una mejor regulación de las tensiones de estator durante operación en debilitamiento de campo. Así, los resultados de simulación muestran que es más conveniente utilizar el esquema *híbrido* de regulación de par propuesto en esta tesis que el enfoque convencional *doble trifásico*. En consecuencia, se descarta el enfoque *doble trifásico*, y la validación experimental se centra en el enfoque *híbrido* de regulación del par. También se demuestra que la incorporación del algoritmo de equilibrado es obligatoria para los accionamientos con una configuración en cascada del bus CC, ya que su desactivación provoca inestabilidades que ponen en peligro la integridad del sistema de propulsión.

A continuación, se valida experimentalmente la solución propuesta de con-

trol *híbrido* de par con capacidad de equilibrado de tensión. Inicialmente, el controlador propuesto se implementa en una plataforma digital de prototipado rápido de control en tiempo real dSPACE MicroAutoBox II. Posteriormente, el sistema de control se valida, en TRL-6, sobre un banco de ensayos de laboratorio, incorporando un prototipo a escala real del accionamiento eléctrico con una potencia máxima de 135 kW, desarrollado en el contexto del proyecto FITGEN. Estas pruebas iniciales muestran un alto rizado de corriente de alta frecuencia causado por la presencia de bobinados solapados en el estator de la máquina. Para mitigar este problema se implementa un esquema de modulación PWM entrelazado. Este esquema consiste en utilizar señales portadoras desfasadas 180 grados para cada conjunto trifásico. Tras esta modificación, el controlador se prueba exhaustivamente en laboratorio bajo diversos perfiles de funcionamiento, incluyendo cuatro ciclos de conducción. Estos perfiles permiten comprobar el correcto funcionamiento del controlador, tanto en estado estacionario como en régimen transitorio. También se evalúa la respuesta del accionamiento ante condiciones de conducción en vehículo mediante la emulación de los ciclos de conducción estandarizados WLTP y US06, además de dos ciclos de conducción que emulan dos trayectorias urbanas en la ciudad de Turín.

Finalmente, el accionamiento eléctrico se integra en un vehículo eléctrico real, y el nuevo controlador se valida a nivel TRL-7. Es decir, el accionamiento es validado en un entorno hostil real en cuanto a condiciones de conducción, vibraciones, altas temperaturas e interferencias electromagnéticas (EMI, por sus iniciales en inglés). Para esto, se realizan tanto pruebas de dinamómetro como en carretera. En estas pruebas el accionamiento eléctrico y su sistema de control es testeado en condiciones de conducción intraurbana, suburbana y extraurbana, con velocidades de hasta 120 km/h. Gracias a ello, se evalúa la aplicabilidad industrial de los accionamientos IPMSM trifásicos duales con configuración de bus CC en cascada, y las soluciones de control propuestas quedan plenamente validadas para su utilización en aplicaciones reales de automoción.

Resumen

Laburpena

Errepideko garraioa da berotegi-efektuko gasen isurketen arduradun nagusienetako bat. Literatura zientifiko berrienaren arabera, ibilgailu elektrikoak (EV, *electric vehicle*, ingelesez) masiboki merkaturatzea beharrezkoa izango da, besteak beste, aldaketa klimatikoari aurre egiteko. Beraz, automobilgintzaren industria eta zenbait estatu mailako eta naizoarteko gobernu-erakunde baliabide ugari inbertitzen ari dira helburu hori lortzeko. Esfortzu horiei esker, ibilgailu elektrikoetarako propultsio-sistema berriak garatzen ari dira.

Fase anitzeko motor elektrikoak etorkizun handiko teknologiak dira ibilgailu elektrikoen propultsio-sistema berrietan integratzeko. Zenbait abantaia dituzte teknologia horiek hiru fasedun makina konbentzionalekin konparatuz gero, hala nola potentzia-dentsitate altuagoa, hutsegite tolerantzia, kizkurdura baxuagoa momentu elektromagnetikoan, eta eraginkortasun altuagoa. Eskuragarri diren fase anitzeko arkitekturen artean, iman iraunkorreko makina sinkrono (PMSM, *Permanent Magnet Synchronous Machine*, ingelesez) dual trifasikoak nabarmendu daitezke ibilgailu elektrikoetan ezartzeko, gauzatu beharreko trantsizio teknologikoa nahikoa zuzena baita hiru faseko teknologietatik abiatuta. Etorkizuneko ibiligailuek izango dituzten eskakizun zorrotzak kontuan hartuta, hurrengo belaunaldiko ibilgailu elektrikoetan erabiltzeko trakziorako soluzio berria proposatzen du Europar Batasunak finantzatutako FITGEN proiektuak. Sei fase dituen Silizio Karburozko (SiC) inbertsorea erabiltzen da abiadura handiko hiru faseko IPMSM motor berri bati eragiteko, ezaugarri nagusi bezala potentzia-dentsitate altua duena. Horrez gain, dc/dc bihurgailu bat ezartzen da baterien eta potentzia-inbertsorearen artean, dc karga azkarrak ahalbideratuz. Garestiak diren eta eraginkortasun baxua duten blokeatze-tentsio altuko gailu erdieroaleen erabilera ekiditzeko, turrustan konektatutako dc-*link* konfigurazioa erabiltzen da sei fasetako inbertsorean.

Aurretik aipatutako proiektuarekin erlazionatzen da tesi hau. Tesiaren helburua da turrustan konektatutako kondentsadoreak dituzten eragile trifasiko

dualen kontrolerako soluzio berriak diseinatzea, garatzea eta balioztatzea. Momentu elektromagnetikoaren erregulazio zehatza eskaini behar du kontrolak, kontuan hartuta motor trifasiko dualak akoplamendu handia duela talde trifasikoen artean. Horrez gain, abiadura altuetan operatu behar du kontrolak (22.500 rpm-artekoak), 24 kHz-etara arteko kommutazio-mahiztasunekin lan eginez. Abiadura-eremu osorako kontrola gauzatu behar da, IPMSMaren saturazio magnetiko handia kontuan hartuta. Azkenik, derrigorrezkoa da turrustan konektatutako dc-*link*eko tentsioak orekatzen dituen algoritmo aktiboa integratzea, konfigurazio horren portaera dela-eta.

Hori guztia kontuan hartuta, izar konexioa duten n fasedun motorren portaera fisikoa deskribatzen duten formula matematikoen analisi sakona gauzatzen da. Azterketa orokortu horrek erraztu egiten du fase anitzeko arkitekturen modeloen inplementazioa. Hain zuzen ere, fase anitzeko motorren modelizazioa azaltzen da horien fase-magnitude naturaletan. Ondoren, modeloa sinplifikatu egiten da transformazio bektorial egokiak erabiliz. Tesiaren atal horren amaieran zenbait simulazio-emaitza aurkezten dira modelizaziorako prozedura orokortua ilustratzeko.

Behin hori guztia eginda, automobilerako IPMSM simetriko dual trifasikoetara partikularizatzen dira aurretik gauzatutako modelo orokortuak. Alde horretatik, hiru hurbilketa aztertzen dira modelizaziorako. Lehenak bere fasezko aldagai naturaletan errepresentatzen du motorra. Hurrengo biek, aldiz, transformazio bektorialak erabiltzen dituzte. Fase anitzeko modeloa lortzeko, bobinatu-taldeen arteko akoplamendu magnetikoa kontsideratzen duen sei fasedun transformazio bektoriala ezartzen da. Aldiz, hiru fase bikoitzeko modeloa errepresentazio sinplifikatu bat da, bobinatu-talde bakoitzari hiru faserako transformazio bektorial konbentzionalak ezarriz lortzen dena. Beraz, magnitude trifasikoak esplizituki adierazten dira hiru fase bikoitzeko modeloan. Garatutako modelo guztiak instrumentalak dira, kontrolerako soluzio berriak garatzen laguntzeko, eta baita ere horien simulazio bidezko aurretiko balioztapena gauzatzeko erabilgarri direnak.

Modelizazioari dagokion analisia amaitu ondoren, momentu elektromagnetikoaren kontrolerako hiru algoritmo bektorial aurkezten dira, IPMSM dual trifasiko simetrikoetarako balio dutenak. Lehenik, hiru fase bikoitzeko kontrola aztertzen da, set trifasiko bakoitzaren korronteen erregulazio independentea ahalbideratzen duena. Bigarrenak, fase anitzeko kontrolagailu deritzonak, posible egiten du momentu elektromagnetikoaren erregulazio zehatza, bi set trifasikoen akoplamendu magnetikoa kontuan hartzen baitu. Azkenik, momentu elektromagnetikoaren kontrolerako algoritmo hibridoa deritzona proposatzen da tesi honen kontribuzio nagusienetakoa bezala. Transformazio matrizial berri bat

erabiltzen du soluzio horrek, eta aurretik aipatutako bi kontrol-soluzioen errep-resentazio bektorialak konbinatzen ditu. Horrela, horien abantaiak aprobetx-atzen dira, desabantaiak ekidinez. Automobilerako eragile baten beharrizanak betetzeko derrigorrezkoak diren osagaiak biltzen ditu kontrolagailu berri horrek. Hori da, korronte-erreferentziak sortzeko algoritmoa dauka, abiaduraren normal-izaziorako bloke batetan, tentsioaren limitearen jarraipenerako bloke batetan eta 2D tauletan (LUT, *Look-up Table*, ingelesez) oinarritzen dena. Osagai horren bidez posible da beharrezkoak diren korronte-erreferentziak sortzea, abidura-eremu guztian zehar, saturazio magnetikoa eta akoplamenduak kontuan hartuta, momentu elektromagnetikoa modu zehatzean sortu ahal izateko. Horrez gain, bai korronte-erreguladoreak eta baita ere modulazio-algoritmoa fase anitzeko egoerara moldatzen dira.

Turrustan konektatutako dc-*link* konfigurazioa sistema trifasiko dualetan xehetasun handiarekin errepresentatzen duen modelo matematikoa aurkezten da ere. Modelo matematiko horren laguntzaz, tentsioak orekatzeko helburua duen algoritmo berria garatzen da, motorraren abiadura-eremu osoan lan egiten duena. Ondoren, aurretik proposatutako kontrolagailu hibrido bektorialean eta hiru fase bikoitzekoan integratzen da soluzio hori. Simulazio-emaitzek frogatzen dutenez, soluzio hibridoak emaitza askoz hobeak lortzen ditu. Horrez gain, tentsioak orekatzeko algoritmoa erabiltzea derrigorrezkoa dela frogatzen da, hori desaktibatuz gero sortzen diren ezegonkortasunek propultsio-sistemaren integri-tatea arriskuan jartzen baitute.

Azkenik, esperimentalki balioztatzen dira proposatutako momentu elektro-magnetikoaren kontrolerako algoritmo hibridoa eta tentsioak orekatzeko algo-ritmoa. Hasiera batean, proposatutako soluzioak prototipatze azkerreko kon-trolerako (RCP, *Rapid Control Prototyping*, ingelesez) dSPACE MicroAutoBox II denbora errealeko gailu digitalean integratzen dira. Ondoren, TRL-6 mailan balioztatzen da kontrol-sistema laborategian, 135 kW-ko potentzia maximoa duen prototipoan, FITGEN proiektuaren testuinguruan garatutakoa. Hasie-rako entseguek erakusten duten moduan, beharrezkoa da gurutzatutako PWM teknika bat erabiltzea, estatoreko harilkatuan faseen artean den gainezartzea dela-eta. Aldaketa hori gauzatu ondoren, kontrolagailua estentsiboki frogatzen da laborategian hainbat operazio-profil erabiliz, lau gidatze-ziklo horien artean. Test horiek amaitu ondoren, ibilgailu elektriko erreal batetan integratzen da eragilearen prototipoa, eta kontrol-soluzio berriak TRL-7 mailan balioztatzen dira, dinamometro batetan eta baita ere bidean. Horri guztiari esker, dc-*link*a turrustan duten IPMSM dual trifasikoen aplikabilitate industriala frogatzen da, eta proposatutako kontrolerako soluzioak guztiz balioztatzen dira, horiek auto-mozioko aplikazio errealetan erabili ahal izateko.

Chapter 1

Introduction and contextualization

1.1 Climate change and transport electrification

Climate change has become a first-order societal problem, where the anthropogenic Green House Gas (GHG) emissions are responsible for global warming. In this sense, NASA's terrestrial observatory has monitored the temperature anomalies throughout the planet, assessing that mean global temperature has increased up to 0.8°C from 1880 to present[1]. This is due to the fact that atmospheric concentrations of CO_2, CH_4, and NO_x particles have significantly increased. For example, according to the United States National Oceanic and Atmospheric Administration (NOAA), CO_2 levels have increased from 280 ppm to 406 ppm in the last 150 years[2].

To address this issue, 195 countries adopted the first-ever universal legally binding global climate deal in the Paris Climate Conference (COP) in December 2015. Its primary goal was to limit the rise in global mean surface air temperature at 2°C since pre-industrial times to the year 2100, following the RCP2.6 pathway [4]. Toward that end, the reduction of GHGs is required, with full decarbonization by 2070.

After electricity and heat generation, the transport sector is the largest producer of CO_2 worldwide, representing 25 % of total emissions in 2019 [5]. Fur-

---

[1]https://svs.gsfc.nasa.gov/4964
[2]https://gml.noaa.gov/ccgg/trends/history.html

thermore, the International Energy Agency (IEA) projects an average annual global transport energy demand increase of 1.6 % between 2007 and 2030. In particular, from the total emissions generated by the transport sector, road vehicles represent a 77 %, followed by aviation with a 12 % [5]. For this reason, the automotive industry is one of the most active sectors involved in the reduction of such emissions. Besides, the massive introduction of electric vehicles (EV) is expected, as it is crucial for achieving the emission reduction targets [6, 7].

Considering all the previous, many resources are being invested in the development of new transport technologies. For example, from 2014 to 2020, the European Union has invested 3.07 billion euros in transport electrification research projects [8]. New challenges and opportunities are arising for mechanical and electronics control engineers. One of the most demanding research areas includes the development of efficient, low-cost, optimized, and reliable electric propulsion systems.

Several technological targets must be considered during the development of such new propulsion systems, which involve power electronics converters and electric machines. These figures are generally specified by a number of stakeholders/programmes, such as the United States Council for Automotive Research (USCAR), the United Nations Economic and Social Commission for Asia (UN ESCAP), and the European Union's H2020 programme, among others. In this context, some of the most relevant targets are the followings [9, 10]:

(a) Increase of torque generation capabilities of the electric machine by 30 %.

(b) Increase of the rotational speed of the electric machine by 50 %.

(c) Reduction of machines' copper and iron losses of 50 %.

(d) Increase of the power density of power converters of 50 %.

(e) Reduction of power converter losses (conduction and switching) of 50 %.

(f) Overall efficiency optimization of 20 %.

(g) Overall weight and volume reduction of the whole powertrain of 40 %.

(h) Four times cost reduction within the power electronics and the electric machine.

(i) Simplification of the cooling system, using onboard coolants, minimizing, as possible, additional components.

All these stringent demands require a significant evolution from current to future propulsion technologies. A number of advances are needed, such as the utilization of new wide-bandgap (WBG) power semiconductor devices [9,11–13], advanced cooling technologies [7, 13–16], new generation High-Speed Electric Machines (HSEM) [17–19], the reduction of the dependence on rare-earths, such as Nd, Dy and T_b [20–23], and the design of advanced control solutions [13, 24–26], among others.

1.2   Multiphase electric drives

Regarding the electric machine technology, electrical propulsion systems powered by multiphase drives are gaining attention over conventional three-phase solutions thanks to their advantages [24, 27–31]:

- A reduced harmonic distortion in the stator currents, leading to a low ripple in the produced electromagnetic torque, allowing a smoother machine operation [32–35].

- A reduction of the harmonic content in the dc bus current. This decreases the operating temperature of the dc-link capacitor(s), improving efficiency and extending lifespan or reducing component costs [1, 36, 37].

- A reduction of the per-phase peak currents and power ratings. This can significantly improve the system's overall efficiency, reducing costs, allowing the utilization of a simpler cooling system, and extending the lifespan of the semiconductor devices [3, 28, 38, 39].

- An increase in the reliability and availability of the vehicle, thanks to the intrinsic fault tolerance of multiphase machines. Furthermore, the additional degrees of freedom of such multiphase systems allow the utilization of specific control algorithms that can improve the operation of the EV after the occurrence of a fault [24, 25, 40, 41].

- An improvement of the machine's power density/torque generation capabilities, reducing the drive's volume and weight [31, 42–44].

Most of these performance benefits align with the previously summarized requirements for future EV drivetrains, making multiphase technologies attractive for automotive traction solutions.

(a) Star-connected symmetrical.

(b) Open-end winding.

(c) Multiple three-phase.
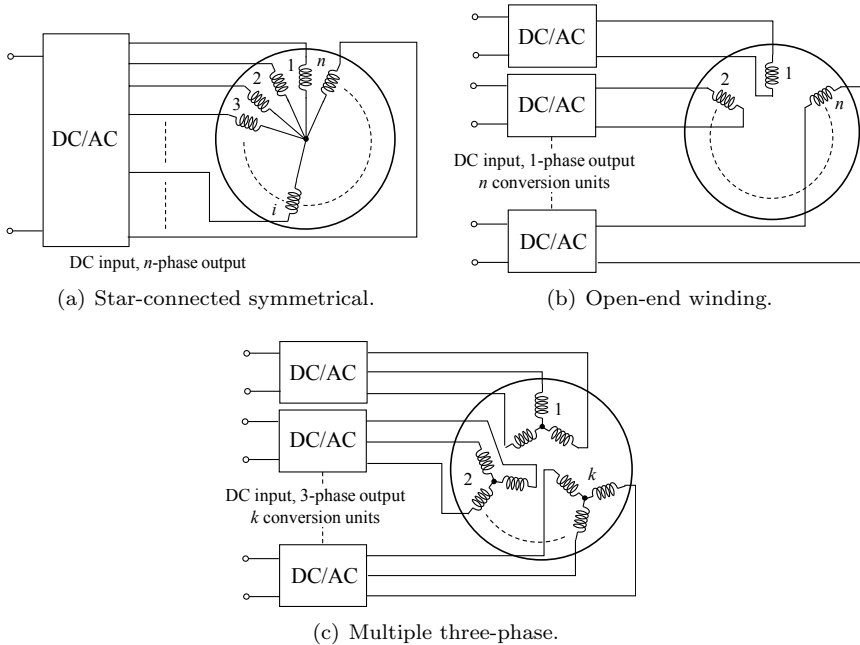
Fig. 1.1: Most common multiphase electric drive topologies [1].

Three main topologies for multiphase electric drives (Fig. 1.1) are widely studied in the scientific literature [1,29,45,46]. The first one is the star-connected symmetrical multiphase configuration. In this topology, all n phases are star-connected and are symmetrically distributed in the transversal plane of the machine [Fig. 1.1(a)]. That is, the angle between two adjacent phases is $2\pi/n$. This machine type is usually fed by an inverter with n half-bridge legs [47, 48]. In such systems, their additional degrees of freedom can be exploited for fault-tolerant operation [49–52] and torque production enhancement [2,3,43,53, 54]. Star-connected symmetrical multiphase drives can be found in a variety of transport applications such as in aircraft Electromechanical Actuators (EMAs) [46,55,56], and in EV propulsion systems [36,57,58].

The second multiphase topology is the one known as the open-end winding configuration [Fig. 1.1(b)]. In this case, each phase is fed by its own independent

full- or H-bridge power converter. This configuration offers the best performance in terms of fault tolerance [1, 59]. Another advantage of this topology is that it allows a greater utilization of the dc bus since the maximum voltage per phase is the dc voltage itself [1, 60]. However, this comes at the cost of increasing complexity and doubling the number of power electronics switches required to control the machine [1, 29, 45], making it attractive for applications with high safety demands, such as for aerospace applications [61, 62] but, as the automotive sector is highly cost-sensitive, they are not a common alternative found in EVs.

The third topology is known as the multiple three-phase configuration [63, 64]. As the name indicates, it consists of k sets of three-phase windings with isolated neutral points [Fig. 1.1(c)]. Within each set, the three phases are uniformly distributed in space, i.e., the angle between two adjacent phases is $2\pi/3$. In general, conventional three-phase power inverter units feed each set. The total number of phases in this type of machine is $n = 3k$. Between each set, there is a displacement angle. Therefore, depending on the value of such displacement angle, the phases are symmetrically or asymmetrically distributed in space. Traditionally, the asymmetrical configuration was preferred over the symmetrical configuration because the former eliminates the sixth harmonic pulsating torque component when operated with a six-step inverter [65, 66]. However, [67, 68] show that symmetrical machines offer the same torque performance as asymmetrical machines when operated with actual high-frequency PWM modulation techniques. In fact, for fault-tolerant operation, the symmetrical configuration is preferred [68].

The simplest multiple three-phase configuration is obtained when $k = 2$. These are the so-called dual three-phase machines and are the most widely used among the multiple three-phase ones [1, 69]. From all the available multiphase architectures, dual three-phase Permanent Magnet Synchronous Machine (PMSM) drives are preferred for near-future EV applications, as the technological transition from three-phase systems is relatively straightforward, and their power/torque density is among the highest [9, 69]. For example, the company DANA-TM4 commercializes dual three-phase drives for class 2 to 6 commercial vehicles and light to medium bus platforms[3].

1.3 Context of the Thesis

This Ph.D. thesis focuses on the development of novel control solutions for multiphase EV drive systems, with special emphasis on symmetrical dual three-

---

[3]https://www.danatm4.com/products/systems/sumo-md/

phase PMSM architectures. The Thesis has been carried out in the Industry and eMobility unit of Fundación Tecnalia Research and Innovation, Derio, Spain. In particular, most parts of this Thesis have been conducted within the Clean Powertrain & Electrification Group of Tecnalia. The main current activities of this group are:

(i) Electric propulsion systems: In this activity, both EV (from light duty to heavy duty) and aerospace systems are researched and developed. Main sub-activities include dimensioning of the propulsion system, control of transmission and torque management, energy management systems in Hybrid and full EVs, powertrain-level controllers, etc.

(ii) Control of electric drives (PMSM, Synchronous Reluctance and induction machine drives): Focusing on advanced field weakening control solutions, multiphase control, sensorless control, fault-tolerant control, diagnosis, monitoring, etc.

(iii) Modeling and simulation: Plant modeling (vehicle and environment) and development of Hardware-in-the-Loop (HiL) tools.

(iv) Software and hardware development: ECU development for prototypes and industrialized and certifiable solutions (automotive grade), Model-Based Design (MBD) programming approaches following the V-methodology, etc.

In particular, this Thesis was developed within the context of the European Union's FITGEN (Functionally Integrated E-axle Ready for Mass Market Third Generation Electric Vehicles) project[4]. This project has received funding from the European Union's H2020 research and innovation programme under Grant Agreement no. 824335.

This project's key performance indicators, regarding the state-of-the-art of EV powertrains at the project's start, were [70]:

- A 40 % increase in the power density of the electric machine, with a rotational speed up to 22500 rpm.

- A 50 % increase in the power density of the inverter, thanks to the adoption of SiC components.

---

[4]fitgen-project.eu/
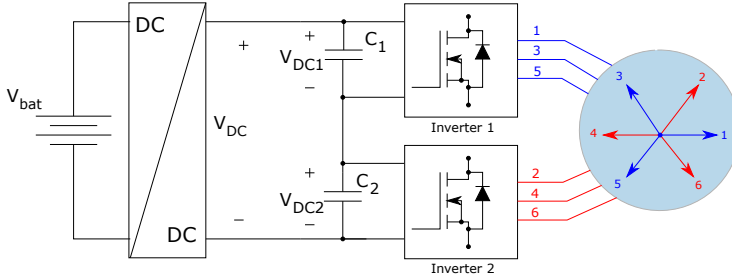
Fig. 1.2: General diagram of a dual three-phase IPMSM drive architecture with cascaded dc-link capacitors and dc/dc converter.

- An affordable super-fast charging capability (120 kW peak) thanks to the incorporation of a dc/dc converter and up to 11 kW domestic charging through innovative onboard charger topologies.

- An increase of the EV driving range from 740 to 1050 km (including 75 minutes of charging time) in real-world freeway driving.

Several national and international partners participated within the Horizon 2020 FITGEN project: The Austrian Institute of Technology (AIT), Fundación Tecnalia Research and Innovation (member of the Basque Research Technology Alliance, BRTA), Centro Ricerche FIAT SCPA (CRF), Brusa Elektronik AG, Politecnico di Torino (POLITO), STMI Electronic, GKN Driveline International GmbH, and Vrije Universiteit Brussel (VUB). The project started on January 1st, 2019 and finished on September 30th, 2022. The project was funded with a total of 5.841.242,50 €[5].

A dual three-phase Interior PMSM (IPMSM) technology has been selected, developed, and manufactured within the project to constitute the electric drive and meet the aforementioned requirements. The power electronics, based on WBG SiC semiconductors, incorporate a cascaded dc-link configuration, requiring particular control solutions.

Fig. 1.2 illustrates the dual three-phase IPMSM drive architecture with such a cascaded dc-link and a dc/dc converter. This cascaded configuration was initially proposed for transformer-less wind turbines [71–79]. In these works, the cascaded configuration allowed high ac-dc boosting capability, which facilitates

---

[5]https://cordis.europa.eu/project/id/824335/es

a transformer-less system operation. Then, this type of configuration was proposed for EVs [80–82] and adjustable speed drives [83, 84]. In [85] and [86], machine design considerations and modulation techniques for the cascaded configuration are analyzed. The cascaded configuration is proposed for electric drives as it offers modularity and allows the incorporation of devices with low voltage ratings. However, to the author's best knowledge, this Thesis and its related publications are the first ones where that the cascade configuration is combined with a full-scale automotive IPMSM.

This Thesis contributes with a novel control solution for this type of specialized drive. The proposal is validated by simulations, laboratory test bench experimental results (in Tecnalia Derio and AIT Wien), and, finally, in-vehicle experimentation at the CRF facilities in Torino.

In addition, the Thesis was done within the Doctoral Programme of Electronics and Telecommunications of the University of the Basque Country (UPV/EHU)[6]. The Thesis was supervised by a professor/researcher of the Applied Electronics Research Team (APERT)[7] of the UPV/EHU. Among other activities, the APERT group researches electronics for EVs' traction and charging infrastructure and power electronics converters.

Once the key points of this Thesis are introduced, and the industrial/research context is detailed, its objectives are summarized.

1.4 Objectives

The main objective of this Thesis is to investigate, propose and validate, at TRL-7 (Technology Readiness Level)[8], novel control solutions for dual three-phase IPMSM drives considering precision in torque regulation, full speed range operation and voltage balancing requirements of a cascaded dc-link configuration.

To meet this main goal, the following secondary objectives have been defined:

1. The development of accurate electric drive models, per-phase and vector modeling approaches, for the preliminary analysis of the proposed control solutions. This requires a comprehensive analysis and understanding of the mathematical expressions that represent the physical behavior of the drive.

---

[6]https://www.ehu.eus/en/web/doktoregoa/doctorate-electronics-telecommunications
[7]https://www.ehu.eus/en/web/apert/start
[8]System prototype demonstration in an operational environment. From: https://ec.europa.eu/research/participants/data/ref/h2020/wp/2014_2015/annexes/h2020-wp1415-annex-g-trl_en.pdf

2. The proposal of specific control solutions for dual three-phase IPMSMs considering different vector transformation representations and also considering the particular operating conditions of the drive: high magnetic saturation, field weakening, etc.

3. The development of an accurate mathematical model of the cascaded dc-link configuration for dual three-phase drives.

4. The proposal of a novel dc-link voltage balancing algorithm for cascaded dc-link configurations, with the aim to operate the drive within the full speed and torque range.

5. The complete experimental verification of the solution at TRL-7 for its future industrialization in real EVs.

The content of the Ph.D. thesis' document is organized following the logical sequence provided by the aforementioned sub-objectives to facilitate its reading.

1.5   Structure of the document

This document is constituted of five chapters. Their content can be summarized as follows:

1. **Introduction** First, a general context of the research activities carried out within this Thesis is presented in this chapter, highlighting their relevance in the current climatic emergency situation, and also presents a summary of the state of the art regarding multiphase electric drives. The main research project related to this Thesis and the institutions in which the work has been carried out are also briefly described. Then, the objectives are outlined, and the structure of the document is summarized.

2. **Modeling of star-connected symmetrical multiphase PMSMs**. In this chapter, the two main modeling approaches for symmetrical n-phase star-connected PMSMs are presented. The first modeling approach describes the dynamics of the machines using the natural per-phase electromagnetic variables. The second modeling approach uses vector transformations to simplify the mathematical description of the machine. Such vector transformation combines two matrices, the decoupling and the rotational ones. Both matrices are detailed, and their mathematical and electro-physical interpretation is provided. Finally, and for illustrative

purposes, the simulation model of a five-phase star-connected BLDC machine is developed, and some simulation results are provided.

3. **Modeling and control of dual three-phase IPMSMs**. In this chapter, three mathematical modeling approaches are presented and analyzed to represent dual three-phase IPMSMs. First, the modeling in natural per-phase variables is addressed. Then, two vector modeling approaches are presented, and their advantages and disadvantages are analyzed. Next, the components required to implement a full-speed range vector torque controller are described. Additionally, general guidelines for tuning and implementing such components are provided.

   Next, three alternatives for the vector torque control of dual three-phase IPMSMs are studied. A comparison of the pros and cons of each alternative is carried out. The first two solutions are directly derived from the two vector models mentioned above, while the third one is a novel proposal that seeks to combine the advantages of the two previous ones while mitigating their downsides.

4. **Torque control of automotive dual three-phase IPMSM with a cascaded dc-link**. This chapter presents the main contribution of this Thesis. It proposes a novel full-speed range torque control solution for an automotive dual three-phase IPMSM drive. For the design of such a control algorithm, first, a detailed mathematical model of the cascaded dc-link configuration is provided. Then, a novel dc-link voltage balancing algorithm is proposed and described. This new approach is combined with two torque controller approaches.

   Finally, preliminary simulation results are provided, and a comparison of the torque regulation solution alternatives that incorporate voltage balancing capabilities is carried out. The selected alternative is then fine-tuned and validated in a TRL-6 test bench. Finally, the features of the novel control solution are validated in a commercial EV, reaching TRL-7 and demonstrating the feasibility of the industrial utilization of the proposal.

5. **Conclusions and future work**. This chapter summarizes the conclusions obtained from this work, together with its novel contributions. The publication and dissemination activities resulting from this work are also presented in this chapter. Finally, future research lines are provided.

In addition, two appendices complement the content of the previously described chapters.

A. **Voltage vector saturation.** In this appendix, three voltage vector saturation algorithms are described for PMSM FOC controllers.

B. **SMC per three-phase set with harmonic injection capabilities**. This appendix presents a novel control solution for dual three-phase machines based on first-order sliding mode control techniques. Then, an algorithm for the injection of triplen voltage harmonics to enhance the dc-link voltage utilization is presented.

Chapter 2

Modeling of star-connected symmetrical multiphase PMSMs

Modeling and simulation of multiphase machines have been widely investigated in the scientific literature [29,30,33,37,87–94], as the utilization of accurate models allows control engineers to properly develop their solutions, in a simulation environment, before their experimental validation. In this context, the multiple-machine concept is commonly used to model the behavior of star-connected symmetrical multiphase machines. This model uses fictitious voltages and currents that allow simplifying the representation of the system. In contrast, the utilization of models implemented in natural machine variables facilitates the simulation of the system under faults, which is necessary for the convenient simulation of fault-tolerant controllers when needed.

This chapter focuses on both modeling approaches, providing the fundamental and the mathematical basis required to understand better the technical content of the next chapters and the implemented simulation models. Finally, some simulation results are incorporated for illustrative purposes.

2.1 Modeling in natural machine variables

This approach relies on describing the model using the natural variables of the machine, i.e., per-phase voltages, currents, inductances, and permanent magnet flux linkages.

2.1.1 Electromagnetic model in per-phase variables

As a first step to model an n-phase star connected PMSM, the well-known voltage equation of the machine stator windings is defined:

$$\mathbf{V} = \mathbf{RI} + \frac{d\mathbf{\Psi}}{dt},$$

(2.1)

where $\mathbf{V}$ and $\mathbf{I}$ are n-dimensional vectors, represented by (2.2) and (2.3). The elements of these vectors (v_j and i_j, $j \in [1, n]$) are the per-phase voltages and currents, respectively. $\mathbf{R}$ is an $n \times n$ diagonal matrix, where each diagonal element represents the phase resistance. Suppose all phases are assumed identical (same materials, an equal number of turns, and the same distribution). In that case, all diagonal elements of such matrix have the same R_s value, as shown in (2.4).

$$\mathbf{V} = [v_1, v_2, v_3, \ldots, v_n]^T,$$

(2.2)

$$\mathbf{I} = [i_1, i_2, i_3, \ldots, i_n]^T,$$

(2.3)

$$\mathbf{R} = \begin{bmatrix} R_s & 0 & 0 & \ldots & 0 \\ 0 & R_s & 0 & \ldots & 0 \\ 0 & 0 & R_s & \ldots & 0 \\ \vdots & \vdots & \vdots & \ddots & 0 \\ 0 & 0 & 0 & 0 & R_s \end{bmatrix}.$$

(2.4)

On the other hand, $\mathbf{\Psi}$ represents the airgap flux linkage and is defined by:

$$\mathbf{\Psi} = \mathbf{LI} + \mathbf{\Psi}_{PM},$$

(2.5)

where $\mathbf{L}$ is the $n \times n$ stator inductance matrix. Each element L_{ij} ($i, j \in \{1, 2, ...n\}$) represents the self- ($i = j$) and mutual-inductances ($i \neq j$) between phases i and j. Considering the spatial distribution of the windings (Fig. 2.1),

(a) Five-phase.

(b) Six-phase.
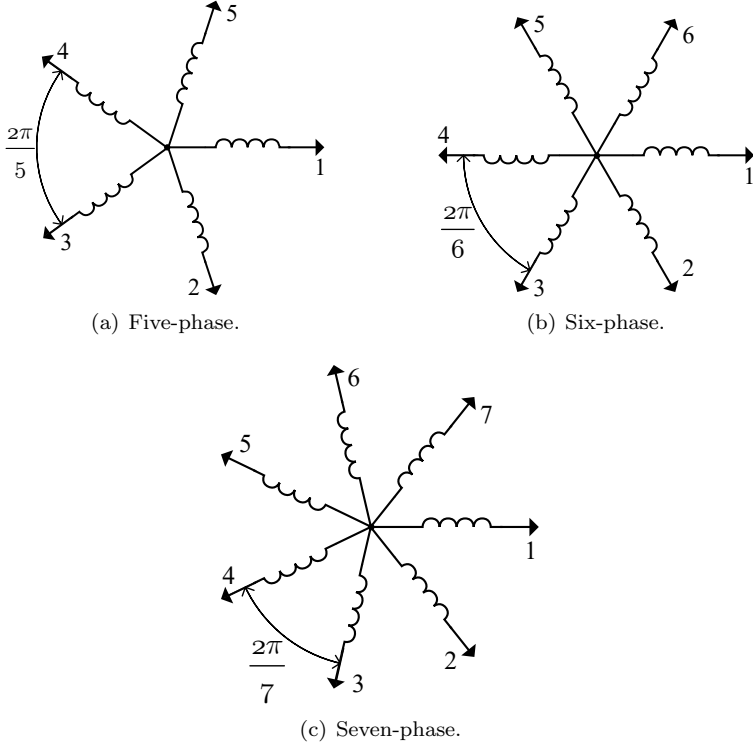
(c) Seven-phase.

Fig. 2.1: Spacial distribution of n-phase star-connected windings particularized for a five-phase, a six-phase, and a seven-phase PMSM.

$\mathbf{L}$ is symmetric. The elements of $\mathbf{L}$ can be constant or can vary with the rotor electrical angle θ_e, depending on the magnet configuration of the machine:

(a) The elements of $\mathbf{L}$ can be considered constant for surface-mounted PMSMs (SM-PMSM), as the surface-placed magnets have a permeability near that of the air. Therefore, an SM-PMSM behaves like a non-salient pole synchronous machine [95]. As all phases are considered identical, the mutual inductances between any phase-pair separated with the same electrical angle are equal, i.e., $L_{12} = L_{1n} = L_{21} = L_{23} = L_{n1} = L_{jk}$ (if $|j - k| = 1$) or $L_{13} = L_{31} = L_{2n} = L_{n2} = L_{jk}$ (if $|j - k| = 2$). Similarly, all the self-

inductances are equal ($L_{11} = L_{22} = \cdots = L_{nn}$). This type of matrix is known as a circulant matrix and has some special properties [96]. Hence, the inductance matrix of an n-phase SM-PMSM is as follows:

$$
\mathbf{L} =
\begin{bmatrix}
L_{11} & L_{12} & L_{13} & \dots & L_{1n} \\
L_{21} & L_{22} & L_{23} & \dots & L_{2n} \\
L_{31} & L_{32} & L_{33} & \dots & L_{3n} \\
\vdots & \vdots & \vdots & \ddots & \vdots \\
L_{n1} & L_{n2} & L_{n3} & \dots & L_{nn}
\end{bmatrix}
=
\begin{bmatrix}
L_{11} & L_{12} & L_{13} & \dots & L_{12} \\
L_{12} & L_{11} & L_{12} & \dots & L_{13} \\
L_{13} & L_{12} & L_{11} & \dots & \vdots \\
\vdots & \vdots & \vdots & \ddots & \vdots \\
L_{12} & L_{13} & \dots & \dots & L_{11}
\end{bmatrix}.
$$

$$(2.6)$$

(b) For IPMSMs, the mutual and self-inductances vary according to θ_e due to the variable magnetic reluctance of such rotor configuration [95]. More precisely, each element of $\mathbf{L}$ has a constant ($l_{ij}^{(0)}$) and a variable (m_{ij}) part:

$$
L_{ij}(\theta_e) = l_{ij}^{(0)} + m_{ij}(\theta_e). \tag{2.7}
$$

The constant part $l_{ij}^{(0)}$ has a circulant structure as for SM-PMSMs. The variable components m_{ij} are periodical even functions, with a period equal to the pole pitch (π electrical radians) [34, 97], which can be represented by a Fourier series of even harmonics:

$$
m_{ij}(\theta_e) = \sum_{k=2}^{\infty} l_{ij}^{(k)} \cos\left[k(\theta_e - \delta_{ij})\right], \tag{2.8}
$$

where, δ_{ij} is related with the phase angle between phases i and j, and $l_{ij}^{(k)}$ is the weight of the k-th harmonic ($k \in \{2, 4, 6, \dots\}$). For machines with symmetrical windings, $\delta_{ij} = (i + j - 2)\, 2\pi/n$. Due to the sinusoidal stator winding distribution and symmetry of the rotor, the second harmonic in (2.8) is usually the dominant one. Therefore, it is common to find the following simplification of the variable terms m_{ij} [34, 94, 97–99]:

$$
m_{ij}(\theta_e) = l_{ij}^{(2)} cos\left[2(\theta_e - \delta_{ij})\right]. \tag{2.9}
$$

The term $\mathbf{\Psi}_{PM}$ in (2.5) is the n-dimensional flux linkage vector ($\mathbf{\Psi}_{PM} = [\Psi_{PM1}, \Psi_{PM2}, \Psi_{PM3}, \dots, \Psi_{PMn}]^T$) produced due to the permanent magnets.

Such elements vary with θ_e. Each $\Psi_{PMi}(\theta_e)$ is a periodic even function [100,101]; therefore, can be represented by a Fourier series:

$$\Psi_{PMi}(\theta_e) = \sum_{l=1}^{\infty} \psi_l \cos\left[l(\theta_e - \phi_{1i})\right], \tag{2.10}$$

where $\phi_{1i} = (i-1)\,2\pi/n$. Considering rotor symmetry, all sine terms and even cosine terms are neglected. Therefore, $l \in \{1, 3, 5, \dots\}$ [47, 100]. The weight of each harmonic component ψ_l depends on the design and manufacture of the machine. For example, the first harmonic is the highest for a machine with a sinusoidal electromotive force (EMF), while the rest of the harmonics are small enough to be neglected. In contrast, in brushless DC (BLDC) configurations, the EMF is quasi-trapezoidal, and the main harmonic components of the permanent magnet flux linkage are the fundamental and third ones [3, 53, 93]. In this case, the fundamental component has an amplitude of approximately 120 % of the total, while the third harmonic has an amplitude of around 27 %. The rest of the harmonics have an amplitude smaller than 4 % and are usually neglected. Other combinations are possible. For example, in [43, 54], machines with fundamental and third harmonic with almost equal magnitudes are proposed.

The next step for modeling a star-connected n-phase PMSM is to replace (2.5) into (2.1):

$$\mathbf{V} = \mathbf{R}\mathbf{I} + \frac{d\mathbf{L}\mathbf{I}}{dt} + \frac{d\mathbf{\Psi}_{PM}}{dt}. \tag{2.11}$$

Then, applying the derivative of the product of two functions, the following is achieved:

$$\mathbf{V} = \mathbf{R}\mathbf{I} + \frac{d\mathbf{L}}{dt}\mathbf{I} + \mathbf{L}\frac{d\mathbf{I}}{dt} + \frac{d\mathbf{\Psi}_{PM}}{dt}. \tag{2.12}$$

This equation reveals a complex, coupled, multi-variable dynamic system. However, the following observations can help to understand and simplify the model. First, the expression $\mathbf{R}\mathbf{I}$ does not lead to any coupling among the phases, as $\mathbf{R}$ is a diagonal matrix. By contrast, expressions including $\mathbf{L}$ lead to coupling among phases. For SM-PMSMs, the term $(d\mathbf{L}/dt)\mathbf{I}$ is equal to zero, because the elements of $\mathbf{L}$ are constant. However, for IPMSMs, this term has to be considered. For both possible representations described by (2.8) and (2.9), the chain rule can be applied:

$$\frac{dm_{ij}(\theta_e)}{dt} = -\omega_e \frac{dm_{ij}(\theta_e)}{d\theta_e} = -\omega_e \sum_{k=2}^{\infty} k l_{ij}^{(k)} \sin\left[k(\theta_e - \delta_{ij})\right], \qquad (2.13)$$

where w_e is the electrical speed of the machine.

Finally, the term $d\mathbf{\Psi}_{PM}/dt$ represents the back-EMF voltage. As for the previous, the application of the chain rule can be followed:

$$\frac{\Psi_{PMi}(\theta_e)}{dt} = -\omega_e \sum_{l=1}^{\infty} l\psi_l \sin\left[l(\theta_e - \phi_{1i})\right]. \qquad (2.14)$$

2.1.2 Electromechanical model in per-phase variables

Once the dynamic model that relates voltages and currents is settled, the following step is to find the expression for the electromagnetic torque (T_{em}) produced by the machine. To do so, the expression of electrical power ($\mathbf{P} = \mathbf{I}^T\mathbf{V}$) is used. From (2.12), the input electrical power of the machine is:

$$P = \mathbf{I}^T\mathbf{R}\mathbf{I} + \mathbf{I}^T\frac{d\mathbf{L}}{dt}\mathbf{I} + \mathbf{I}^T\mathbf{L}\frac{d\mathbf{I}}{dt} + \mathbf{I}^T\frac{d\mathbf{\Psi}_{PM}}{dt}. \qquad (2.15)$$

Here, the term $\mathbf{I}^T\mathbf{R}\mathbf{I}$ represents machine copper losses, which do not contribute to the production of torque. Similarly, neither the power used to change the magnetic energy contributes to the torque production [92, 94, 102, 103]. To calculate this power, the expression of the magnetic energy E_{mag} is used, which is given by:

$$E_{mag} = \frac{1}{2}\mathbf{I}^T\mathbf{L}\mathbf{I}. \qquad (2.16)$$

Thus, the amount of power used to change the magnetic energy is:

$$\frac{dE_{mag}}{dt} = \frac{1}{2}\mathbf{I}^T\frac{d\mathbf{L}}{dt}\mathbf{I} + \mathbf{I}^T\mathbf{L}\frac{d\mathbf{I}}{dt}. \qquad (2.17)$$

Once Joule and magnetic power losses are subtracted from (2.15), and neglecting Foucault and hysteresis losses, the power that is effectively converted into electromechanical power is:

$$P_{em} = \frac{1}{2}\mathbf{I}^T\frac{d\mathbf{L}}{dt}\mathbf{I} + \mathbf{I}^T\frac{d\mathbf{\Psi}_{PM}}{dt}. \qquad (2.18)$$
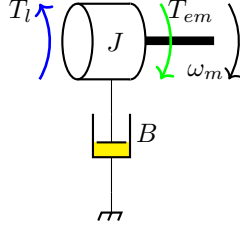
Fig. 2.2: Diagram of the mechanical model of the machine.

By using the well-known relation among power, torque, and mechanical rotation speed ($P_{em} = T_{em}\omega_m$), the expression for the electromagnetic torque is derived:

$$T_{em} = \frac{\frac{1}{2}\mathbf{I}^T\frac{d\mathbf{L}}{dt}\mathbf{I} + \mathbf{I}^T\frac{d\mathbf{\Psi}_{PM}}{dt}}{\omega_m} = \frac{1}{2}\mathbf{I}^T\frac{d\mathbf{L}}{d\theta_m}\mathbf{I} + \mathbf{I}^T\frac{d\mathbf{\Psi}_{PM}}{d\theta_m}, \qquad (2.19)$$

where the term $\frac{1}{2}\mathbf{I}^T(d\mathbf{L}/d\theta_m)\mathbf{I}$ is the reluctant torque [88]. This component is present in salient pole machines (IPMSM). By contrast, there is no reluctance torque in SM-PMSMs, as $d\mathbf{L}/d\theta_m = 0$. The second term $\mathbf{I}^T d\mathbf{\Psi}_{PM}/d\theta_m$ represents the magnetic torque produced thanks to the permanent magnets of the rotor.

The final step consists of modeling the mechanical behavior of the machine. To do so, the conventional rotating mass model shown in Fig. 2.2 has to be used, where speed dynamics are given by:

$$T_{em} - T_l = J\frac{d\omega_m}{dt} + B\omega_m, \qquad (2.20)$$

where T_l is the load torque, J is the moment of inertia of the rotating masses, and B is the viscous friction coefficient. The speed is related to the electrical angle through the following expression:

$$\theta_e = N_p \int_0^t \omega_m dt, \qquad (2.21)$$

where N_p is the machine pole-pair number.
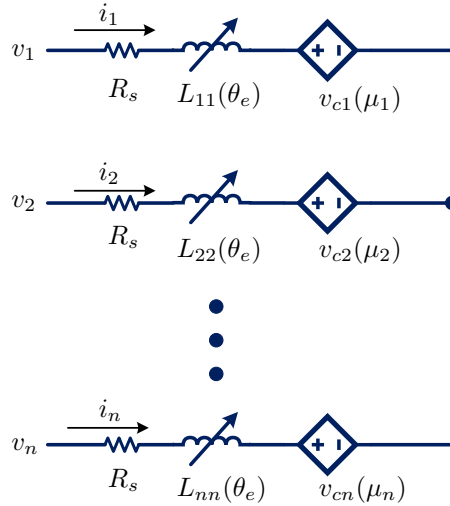
Fig. 2.3: Diagram of the implementation of a star-connected multiphase PMSM in the simulation environment MATLAB/Simscape$^{\mathrm{TM}}$.

2.1.3 Per-phase model implementation in specialized software

In this thesis, the mathematical modeling of the studied star-connected n-phase PMSMs have been implemented in MATLAB/Simulink$^{\circledR}$ by using the Simscape$^{\mathrm{TM}}$ toolbox. This tool allows building a multi-domain physical model through an extensive library of standard components. Besides, the Simscape language allows creating custom components as is required for multiphase machines. Fig. 2.3 shows the diagram of the implemented model considering a star connected n-phase configuration.

To deal with harmonics and the spatial distribution of mutual-inductances, self-inductances, and back-EMF, the text-based programming language of Simscape$^{\mathrm{TM}}$ has been used. This language allows creating custom inductor elements as described by (2.6), (2.8), and (2.9). Similarly, Simscape$^{\mathrm{TM}}$ allows implementing custom voltage sources that emulate back-EMF and phase coupling.

From (2.12), the expression that relates the phase voltage and current for a given phase k is obtained:

$$v_k = R_s i_k + \frac{dL_{kk}}{dt} i_k + L_{kk} \frac{di_k}{dt} + \frac{d\Psi_{PMk}}{dt}$$
$$+ \sum_{j \neq k}^{n} \frac{dL_{kj}}{dt} i_j + \sum_{j \neq k}^{n} L_{jk} \frac{di_j}{dt}. \tag{2.22}$$

The voltage between the terminals of inductor $L_k(\theta_e)$ (Fig. 2.3) is:

$$\frac{dL_{kk}}{dt} I_k + L_{kk} \frac{dI_k}{dt}. \tag{2.23}$$

As mentioned before, if the machine is of SM-PMSM type, then $dL_{kk}/dt = 0$. Consequently, L_k can be modeled as a conventional inductor. By contrast, if the machine is an IPMSM, it is necessary to use the specialized modeling language of Simscape^{TM} to create a custom inductor that considers the variation of the inductance as a function of θ_e. For this case, the inductor voltage is given by:

$$\omega_e \frac{dL_{kk}(\theta_e)}{d\theta_e} I_k + L_{kk}(\theta_e) \frac{dI_k}{dt}. \tag{2.24}$$

The code that has been implemented to create a variable custom inductor is:

Listing 2.1: Custom inductor code.

```
component inductor_motor
    % Inductor_motor
    % Models a non-linear inductor.
    %  V=r*I+L*dI/dt +I*dL/dt where L is inductance[H].
    inputs
        we = { 0.0, 'rad/s' }; % We: left
    end
    nodes
        p = foundation.electrical.electrical; % +:left
        n = foundation.electrical.electrical; % -:right
    end
    parameters
        ls  = { 1e-6, 'H' };        % Inductance fix
        lm  = { 1e-6, 'H' };        % Inductance variable
        ph  = { 0, 'rad' };         % Spatial phase
        r   = { 0, 'Ohm' };         % Series resistance
    end
    variables
        theta = { 0.0, 'rad' };        % Theta electric
        i     = { 0.0, 'A' };          % Inductor current
        v     = { 0.0, 'V' };          % Voltage
    end
    branches
        i : p.i -> n.i;
```

```
25        end
26        equations
27            v   == p.v − n.v;
28            we == theta.der;
29            v   == i*r+(ls+lm*cos(2*(theta+ph)))*i.der+i*(−2*we*lm*sin(2*(
                  theta+ph)));
30        end
31    end
```

Finally, the terms which are not associated with the current i_k are grouped in the controlled voltage source $v_{ck}(\mu_k)$, as shown in Fig. 2.3. The output voltage of this source is given by:

$$v_{ck} = \frac{d\Psi_{PMk}}{dt} + \sum_{j \neq k}^{n} \frac{dL_{kj}}{dt} i_j + \sum_{j \neq k}^{n} L_{jk} \frac{di_j}{dt}, \qquad (2.25)$$

where μ_k stands for all the currents of the other phases and the back-EMF of phase k. Therefore, $\mu_k = \{i_j, \Psi_{PMk}\}$ $(j \neq k)$.

Though complex, the model described above has the advantage that allows simulating both normal and faulty operation conditions in a straightforward way. This model has been built through the interconnection of several electrical elements blocks of Simscape$^{\text{TM}}$. This equivalent electrical circuit emulates the real electrical interconnection among the elements of a physical machine. Thus, it is easy to simulate several open and short-circuit faults between these elements. Consequently, this model can be considered a valuable tool to test and validate fault-tolerant control strategies and can be used to carry out the future research lines defined in chapter 5. Herein, modeling following a vector approximation is presented, which is more convenient for carrying out the simulations required in the early development stages of the control contributions proposed in this thesis.

2.2 Modeling following the vector approach

In this section, the vector modeling approach for star-connected multiphase systems is analyzed. This popular approach makes use of vector transformations to represent the multiphase system in various synchronous reference frames, simplifying the machine's mathematical representation.

As presented in the previous section, (2.12) describes a coupled, nonlinear model. For example, the voltage equation of phase 1 is:

$$v_1 = R_s i_1 + \frac{dL_{11}}{dt} i_1 + \frac{dL_{12}}{dt} i_2 + ... + \frac{dL_{1n}}{dt} i_n +$$
$$+ L_{11} \frac{di_1}{dt} + L_{12} \frac{di_2}{dt} + ... + L_{1n} \frac{di_n}{dt} + \frac{d\Psi_{PM1}(\theta_e)}{dt}. \tag{2.26}$$

As the number of machine phases increases, it becomes clear that the complexity of the model significantly increases. Thus, a simpler model that facilitates the design of the controller is desirable. Various approaches that allow simplifying the mathematical representation of ac machines can be found in the scientific literature:

(a) Complex vector space decomposition [33, 91, 103–107].

(b) Matrix formalism [98, 108–110].

(c) The multi-machine approach [32, 42, 92, 100–102, 111–117].

All these methods make use of vector transformations, transforming the real machine variables into fictitious ones decoupled from each other. These transformations are represented by matrices and are grouped into (i) decoupling and (ii) rotation transformations.

2.2.1 Decoupling transformation

The target of this transformation is to decouple voltages and currents by diagonalizing the inductance matrix $\mathbf{L}$. This matrix is symmetric and circulant, see (2.6), which guarantees that $\mathbf{L}$ is orthogonally diagonalizable by a transformation represented by a real matrix of $n \times n$ [92, 118].

Phase variables (voltages or currents) of a multiphase machine can be seen as components of a vector in the space of n dimensions. In this regard, the decoupling transformation aims to decompose the n dimensional space vector into vectors in orthogonal subspaces decoupled from each other [98]. The number of decoupled subspaces depends on the multiplicity of the characteristic values of $\mathbf{L}$. If the such matrix has m different eigenvalues, it has associated m orthogonal subspaces, each one with a dimension equal to the multiplicity of the corresponding eigenvalue.

The number of characteristic values of $\mathbf{L}$ and their respective multiplicity meet specific properties since $\mathbf{L}$ is a circulant matrix. Due to this feature, $\mathbf{L}$ has $(n-1)/2$ eigenvalues/subspaces with multiplicity/dimension 2 and one

eigenvalue/subspace with multiplicity 1, in case n is odd. If n is even, $\mathbf{L}$ has $(n-2)/2$ eigenvalues/subspaces with multiplicity/dimension 2 and two eigenvalues/subspaces with multiplicity/dimension 1 [92, 102]. After the application of the transformation, each bi- or mono-dimensional resultant vector is orthogonal/decoupled from each other.

According to the multi-machine approach [92], each two-dimensional subspace is equivalent to a two-phase virtual machine, while each one-dimensional subspace is equivalent to a virtual single-phase machine. For example, a conventional three-phase machine splits into one two-phase virtual machine $(d - q)$ and one single-phase machine (homopolar component) whose currents cannot be excited due to the star connection. For an even n-phase machine, it splits into $(n-2)/2$ bi-phase machines and 2 single-phase machines. For example, a 4-phase machine is transformed into one bi-phase machine and two single-phase machines. Again and due to the star connection, the current of one of the single-phase virtual machines cannot be excited, although the other one can be. This has the disadvantage that single-phase machines cannot produce constant torque. Hence, star-connected machines are usually designed and manufactured with an odd number of phases. Conversely, the machines with an even number of phases have, in general, several star points to avoid the excitation of the one-dimensional subspaces. For example, 6-phase machines usually have two neutral points (this type of machine will be studied in chapter 3). In the remainder of this chapter, star-connected machines with an odd phase-number are considered, although most of the analysis can be extended to machines with an even phase-number.

Another critical point addressed in the literature refers to the number of possible decoupling transformations or matrices [92, 102]. If the multiplicity of one of the characteristic values of $\mathbf{L}$ is greater than 1, then there are infinite orthonormal transformations/matrices that diagonalize it. For that reason, many decoupling transformations are reported in the scientific literature about multiphase machines. One of the most studied decoupling matrices is the one presented in [92,98,102,119] as a generalization of the original three-phase Clarke

transformation [120]:

$$\mathbf{D_1} = K_{D1} \begin{bmatrix} 1 & cos(\alpha) & cos(2\alpha) & \dots & cos((n-1)\alpha) \\ 0 & (-1)^b sin(\alpha) & (-1)^b sin(2\alpha) & \dots & (-1)^b sin((n-1)\alpha) \\ 1 & cos(2\alpha) & cos(4\alpha) & \dots & cos(2(n-1)\alpha) \\ 0 & (-1)^b sin(2\alpha) & (-1)^b sin(4\alpha) & \dots & (-1)^b sin(2(n-1)\alpha) \\ 1 & cos(3\alpha) & cos(6\alpha) & \dots & cos(3(n-1)\alpha) \\ 0 & (-1)^b sin(3\alpha) & (-1)^b sin(6\alpha) & \dots & (-1)^b sin(3(n-1)\alpha) \\ \vdots & \vdots & \vdots & \ddots & \vdots \\ 1 & cos(g\alpha) & cos(g2\alpha) & \dots & cos(g(n-1)\alpha) \\ 0 & (-1)^b sin(g\alpha) & (-1)^b sin(g2\alpha) & \dots & (-1)^b sin(g(n-1)\alpha) \\ \frac{1}{K_{D2}} & \frac{1}{K_{D2}} & \frac{1}{K_{D2}} & \dots & \frac{1}{K_{D2}} \end{bmatrix},$$

(2.27)

where $g = (n-1)/2$ is the number of two-dimensional subspaces, and $\alpha = 2\pi/n$ is the angle between two adjacent phases.

As stated before, there are infinite possible decoupling matrices, depending on de values of constants K_{D1}, K_{D2}, and b. For example, if $K_{D1} = \sqrt{2/n}$ and $K_{D2} = \sqrt{2}$, then the transformation is power-invariant. The power-invariant matrix is orthonormal, and its inverse is equal to its transposition. Another possibility is to set $K_{D1} = 2/n$ and $K_{D2} = 2$; then, the resultant transformation is magnitude-invariant, that is, the amplitude of the vectors is equal in both reference systems. A third possibility is to set $K_{D1} = \sqrt{2}/n$ and $K_{D2} = \sqrt{2}$. With this combination, the Root-Mean-Square (RMS) value of the vectors is maintained invariant for both original and transformed reference systems [121].

As mentioned above, there are g two-dimensional subspaces. Each of these is represented by a system of rectangular coordinates ($\alpha_k - \beta_k$, $k \in \{1, 2, 3, ..., g\}$). The remaining mono-dimensional subspace represents the homopolar component. For example, when applying the decoupling transformation to the phase currents, the current vector in the new reference system is:

$$\begin{bmatrix} i_{\alpha_1} \\ i_{\beta_1} \\ i_{\alpha_2} \\ i_{\beta_2} \\ \vdots \\ i_0 \end{bmatrix} = \mathbf{D_1} \begin{bmatrix} i_1 \\ i_2 \\ i_3 \\ i_4 \\ \vdots \\ i_n \end{bmatrix},$$

(2.28)

On the other hand, b can take two values, $b = 0$ or $b = 1$, depending on the selected convention for the perpendicular axes α_k y β_k. Specifically, if the
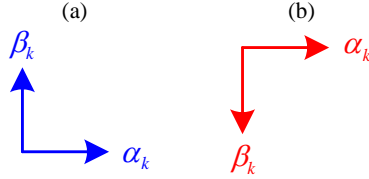
Fig. 2.4: Sign convention for α_k-β_k axes.

Table 2.1: Harmonics associated with each subspace for transformation $\mathbf{D_1}$.

Sub-space	3-ph machine	5-ph machine	7-ph machine
$\alpha_1 - \beta_1$	$h = 3l \pm 1$	$h = 5l \pm 1$	$h = 7l \pm 1$
	$h = 1, 5, 7, ...$	$h = 1, 9, 11, ...$	$h = 1, 13, 15, ...$
$\alpha_2 - \beta_2$	NA‡	$h = 5l \pm 2$	$h = 7l \pm 2$
	NA	$h = 3, 7, 13, ...$	$h = 5, 9, 19, ...$
$\alpha_3 - \beta_3$	NA	NA	$h = 7l \pm 3$
	NA	NA	$h = 3, 11, 17, ...$
homopolar	$h = 3l$	$h = 5l$	$h = 7l$
component	$h = 0, 3, 9, ...$	$h = 0, 5, 15, ...$	$h = 0, 7, 21, ...$

‡NA: Not applicable.

convention shown in Fig. 2.4.(a) is followed, then $b = 1$. On the contrary, if the convention of the axes is the one shown in Fig. 2.4.(b), then $b = 0$.

Another advantage of using this transformation is that it decomposes the vectors according to their harmonic components [92, 100–102]. Thus, the harmonic components $h = nl \pm k$ will be reflected in the k−subspace, where $l \in \{0, 1, 2, 3, \dots\}$. In the subspace corresponding to the zero sequences, the harmonic components of order $h = nl$ are projected. In this context, table 2.1 summarizes the odd harmonics associated with each subspace for three-, five- and seven-phase star-connected ac machines. For example, if the currents in a 5-phase machine have only first and third-order harmonics, the fundamental component will be projected into the subspace $\alpha_1 - \beta_1$, while the third-order one will be projected into the subspace $\alpha_2 - \beta_2$.

However, if it is considered that the per-phase voltages, currents, and fluxes contain only odd harmonics [47, 101], then it is preferable that the decoupling matrix decomposes the vectors according to the odd harmonic components.

Therefore, it is convenient to use the following decoupling matrix [37,93,94,122]:

$$
\mathbf{D_2} = K_{D2}
\begin{bmatrix}
1 & cos(\alpha) & cos(2\alpha) & \dots & cos((n-1)\alpha) \\
0 & (-1)^b sin(\alpha) & (-1)^b sin(2\alpha) & \dots & (-1)^b sin((n-1)\alpha) \\
1 & cos(3\alpha) & cos(6\alpha) & \dots & cos(3(n-1)\alpha) \\
0 & (-1)^b sin(3\alpha) & (-1)^b sin(6\alpha) & \dots & (-1)^b sin(3(n-1)\alpha) \\
1 & cos(5\alpha) & cos(10\alpha) & \dots & cos(5(n-1)\alpha) \\
0 & (-1)^b sin(5\alpha) & (-1)^b sin(5\alpha) & \dots & (-1)^b sin(5(n-1)\alpha) \\
\vdots & \vdots & \vdots & \ddots & \vdots \\
1 & cos(v\alpha) & cos(v2\alpha) & \dots & cos(v(n-1)\alpha) \\
0 & (-1)^b sin(v\alpha) & (-1)^b sin(v2\alpha) & \dots & (-1)^b sin(v(n-1)\alpha) \\
\frac{1}{K_{D2}} & \frac{1}{K_{D2}} & \frac{1}{K_{D2}} & \dots & \frac{1}{K_{D2}}
\end{bmatrix},
\tag{2.29}
$$

where $v = n - 2$. If the inductance matrix is diagonalized, the following is obtained ($\mathbf{L}_{diag} = \mathbf{D_2 L D_2}^{-1}$):

$$
\mathbf{L}_{diag} =
\begin{bmatrix}
\lambda_1 & 0 & 0 & 0 & \dots & 0 & 0 & 0 \\
0 & \lambda_1 & 0 & 0 & \dots & 0 & 0 & 0 \\
0 & 0 & \lambda_3 & 0 & \dots & 0 & 0 & 0 \\
0 & 0 & 0 & \lambda_3 & \dots & 0 & 0 & 0 \\
\vdots & \vdots & \vdots & \vdots & \ddots & \vdots & \vdots & \vdots \\
0 & 0 & 0 & 0 & \dots & \lambda_v & 0 & 0 \\
0 & 0 & 0 & 0 & \dots & 0 & \lambda_v & 0 \\
0 & 0 & 0 & 0 & \dots & 0 & 0 & \lambda_0
\end{bmatrix},
\tag{2.30}
$$

where λ_k ($k \in \{1, 3, 5, ..., v\}$) is the harmonic inductance of the multiphase machine with respect to the harmonics of k-th order [89, 90, 103, 105, 108]. Again, the transformation decomposes the n-dimensional vectors according to their harmonic components. Thus, the harmonic components $h = n(l-1) \pm k$ are reflected in the k-subspace, where $l \in \{1, 3, 5, ...\}$. In the subspace that corresponds to the zero sequences, harmonic components of order $h = nl$ are projected. The odd harmonics associated with each subspace are presented in table 2.2 for three-, five- and seven-phase ac machines.

In general, the subspace $\alpha_1 - \beta_1$ contains the fundamental components of the variables (currents, voltages, and fluxes). The currents and fluxes in this subspace are in charge of producing the effective machine torque. However, if the design and manufacturing of the machine allow it, the control system can

Table 2.2: Harmonics associated with each subspace (transformation $\mathbf{D_2}$).

Sub-space	3-ph machine	5-ph machine	7-ph machine
$\alpha_1 - \beta_1$	$h = 1, 5, 7, ...$	$h = 1, 9, 11, ...$	$h = 1, 13, 15, ...$
$\alpha_3 - \beta_3$	NA‡	$h = 3, 7, 13, ...$	$h = 3, 11, 17, ...$
$\alpha_5 - \beta_5$	NA	NA	$h = 5, 9, 19, ...$
homopolar	$h = 0, 3, 9, ...$	$h = 0, 5, 15, ...$	$h = 0, 7, 21, ...$

‡NA: Not applicable.

be adjusted to generate torque with harmonics other than the fundamental. For example, in [93], besides the fundamental component, the third harmonic component is used to generate torque in a 5-phase machine, demonstrating the benefits of using machines with trapezoidal back-electromotive force (BLDC type), increasing the torque density of the machine by approximately 15 %.

2.2.2 Rotation transformation

The fictitious $\alpha_k - \beta_k$ axes are static. Therefore, a vector that rotates with an angular speed ω will have variable components on these axes. However, if this vector is observed from the point of view of a pair of perpendicular axes rotating at the same speed ω, constant magnitudes are obtained in the new reference frame. In a 2D plane, there are two possible rotation directions. Thus, it is possible to define two rotation transformations. In this work, the one that rotates counter-clockwise is used:

$$\begin{bmatrix} f_{d_k} \\ f_{q_k} \end{bmatrix} = \begin{bmatrix} cos(\omega_k t) & sin(\omega_k t) \\ -sin(\omega_k t) & cos(\omega_k t) \end{bmatrix} \begin{bmatrix} f_{\alpha_k} \\ f_{\beta_k} \end{bmatrix}. \tag{2.31}$$

For PMSMs, this transformation is convenient since the fundamental components of current, voltage, and flux rotate at synchronous speed $\omega_e = d\theta_e/dt$. Consequently, and in order to simplify the electric machine model, components $\alpha_k - \beta_k$ are transformed into multiple $d_k - q_k$ planes which rotate at the speed of the respective harmonic according to the transformation $\mathbf{P}$ in (2.32). This transformation is very useful from the control perspective since proportional-integral (PI) controllers are capable of regulating such non-alternating variables with zero error in a steady state. This way, the fundamental components and harmonics are regulated independently [93].

$$\mathbf{P} = \begin{bmatrix} cos(\theta_e) & sin(\theta_e) & 0 & 0 & \dots & 0 & 0 & 0 \\ -sin(\theta_e) & cos(\theta_e) & 0 & 0 & \dots & 0 & 0 & 0 \\ 0 & 0 & cos(3\theta_e) & sin(3\theta_e) & \dots & 0 & 0 & 0 \\ 0 & 0 & -sin(3\theta_e) & cos(3\theta_e) & \dots & 0 & 0 & 0 \\ \vdots & \vdots & \vdots & \vdots & \ddots & \vdots & \vdots & \vdots \\ 0 & 0 & 0 & 0 & \dots & cos(v\theta_e) & sin(v\theta_e) & 0 \\ 0 & 0 & 0 & 0 & \dots & -sin(v\theta_e) & cos(v\theta_e) & 0 \\ 0 & 0 & 0 & 0 & \dots & 0 & 0 & 1 \end{bmatrix}.$$

$$(2.32)$$

2.2.3   Application of vector transformations

The final step to obtain the decoupled PMSM model consists of applying the transformation $\mathbf{T} = \mathbf{PD_2}$ to the mathematical expressions of the machine in natural variables of (2.12). The following is obtained:

$$\mathbf{V}_{dq} = \mathbf{R}\mathbf{I}_{dq} + \mathbf{L}_{dq}\frac{d\mathbf{I}_{dq}}{dt} - \omega_e\mathbf{J}\mathbf{L}_{dq}\mathbf{I}_{dq} + \mathbf{e}_{dq}, \qquad (2.33)$$

where $\mathbf{V}_{dq} = \mathbf{T}\mathbf{V}$, $\mathbf{I}_{dq} = \mathbf{T}\mathbf{I}$, and $\mathbf{e}_{dq} = \omega_e\mathbf{T}(d\mathbf{\Psi}_{PM}/d\theta_e)$ is the back electromotive force of the machine. On the other hand, $\mathbf{J}$ is an $n \times n$ matrix that equals to $(d\mathbf{T}/d\theta_e)\mathbf{T}^{-1}$. If this last matrix is developed, the J matrix is obtained:

$$\mathbf{J} = \begin{bmatrix} 0 & 1 & 0 & 0 & \dots & 0 & 0 & 0 \\ -1 & 0 & 0 & 0 & \dots & 0 & 0 & 0 \\ 0 & 0 & 0 & 3 & \dots & 0 & 0 & 0 \\ 0 & 0 & -3 & 0 & \dots & 0 & 0 & 0 \\ \vdots & \vdots & \vdots & \vdots & \ddots & \vdots & \vdots & \vdots \\ 0 & 0 & 0 & 0 & \dots & 0 & v & 0 \\ 0 & 0 & 0 & 0 & \dots & -v & 0 & 0 \\ 0 & 0 & 0 & 0 & \dots & 0 & 0 & 0 \end{bmatrix}. \qquad (2.34)$$

On the other hand, the following expression is obtained for the inductance

matrix $\mathbf{L}_{dq} = \mathbf{T}\mathbf{L}\mathbf{T}^{-1}$:

$$
\mathbf{L_{dq}} =
\left[
\begin{array}{cccccccc}
L_{d1} & 0 & 0 & 0 & \ldots & 0 & 0 & 0 \\
0 & L_{q1} & 0 & 0 & \ldots & 0 & 0 & 0 \\
0 & 0 & L_{d3} & 0 & \ldots & 0 & 0 & 0 \\
0 & 0 & 0 & L_{q3} & \ldots & 0 & 0 & 0 \\
\vdots & \vdots & \vdots & \vdots & \ddots & \vdots & \vdots & \vdots \\
0 & 0 & 0 & 0 & \ldots & L_{dv} & 0 & 0 \\
0 & 0 & 0 & 0 & \ldots & 0 & L_{qv} & 0 \\
0 & 0 & 0 & 0 & \ldots & 0 & 0 & L_0
\end{array}
\right] . \tag{2.35}
$$

At this point, it should be taken into account whether the machine has saliency or not. For a machine without saliency (magnets mounted on the rotor surface), $\mathbf{L}_{dq}$ is equal to the $\mathbf{L}_{diag}$ matrix in (2.30) and, therefore, $L_{dk} = L_{qk}$ for $k \in \{1, 3, 5, ..., v\}$. When dealing with a machine with saliency (buried magnets), it must be taken into account that the inductances vary with respect to their position and also which harmonics are considered and which are neglected. For example, if only the harmonics of order two are taken into account in the inductances, then only $L_{d1} \neq L_{q1}$ and, for the rest of subspaces, $L_{dk} = L_{qk}$ for $k \in \{3, 5, 7, ..., v\}$. However, if the rest of the harmonics are considered, then $L_{dk} \neq L_{qk}$ for $k \in \{1, 3, 5, ..., v\}$.

The next step is to find the expression for the electromagnetic torque in terms of the variables in dq [94]:

$$
\begin{aligned}
T_{em} &= K_{PC}(-N_p \mathbf{J}\mathbf{L}_{dq}\mathbf{I}_{dq} \cdot \mathbf{I}_{dq} + \frac{N_p}{\omega_e}\mathbf{e}_{dq} \cdot \mathbf{I}_{dq}) = \\
&= K_{PC} N_p \left(\sum_{k=1}^{v} k(L_{dk} - L_{qk})I_{dk}I_{qk} + \sum_{k=1}^{v} k\psi_k I_{qk} \right),
\end{aligned} \tag{2.36}
$$

for $k = 1, 3, 5, ..., v$. If the power-invariant constant is used, then $K_{PC} = 1$. On the contrary, if the magnitude-invariant constant is used, then $K_{PC} = n/2$. In (2.36), two differentiated components are observed for the electromagnetic torque. The terms $\psi_k I_{qk}$ correspond to the magnetic torque, while terms $k(L_{dk} - L_{qk})I_{dk}I_{qk}$ are related to the reluctant torque, and only exist when $L_{dk} \neq L_{qk}$.
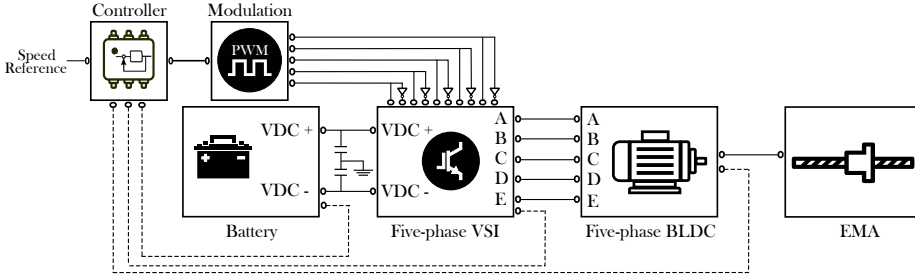
Fig. 2.5: Simplified block diagram of the simulation model of a five-phase BLDC driving an EMA.

2.3 Modeling and simulation procedures applied to a five-phase machine

In order to illustrate the application of the modeling approaches presented above, a simulation platform has been implemented in MATLAB/Simulink$^{\circledR}$. In particular, the per-phase modeling (natural variable modeling) approach is followed in this section, as the vector approach is extensively used in subsequent chapters of this thesis. This platform incorporates a five-phase machine, which is the second most extended used configuration among multiphase machines [29, 36, 94], while the most widely used is the dual three-phase configuration [1, 39, 69] that will be studied in chapters 3 and 4. In particular, a surface-mounted BLDC (SM-BLDC) is considered. For exemplary purposes, this machine drives an Electromechanical Actuator (EMA) to evaluate the model in the context of a variable-speed ac drive. In particular, the EMA is a ball-screw linear actuator that translates rotational machine motion to linear motion. Fig. 2.5 shows a simplified block diagram of the implemented simulation model.

2.3.1 Mathematical model of a five-phase BLDC

As stated before, the relationship between the phase currents and voltages in a star-connected multiphase machine is given by (2.12), where, for a five-phase system, $\mathbf{V} = [v_1, v_2, v_3, v_4, v_5]$ and $\mathbf{I} = [i_1, i_2, i_3, i_4, i_5]$ are the phase voltage and current vectors, $\mathbf{R} = R_s I$ is a 5×5 diagonal matrix that represents the phase resistance (I is the identity matrix), and $\mathbf{L}$ is a 5×5 circulant matrix
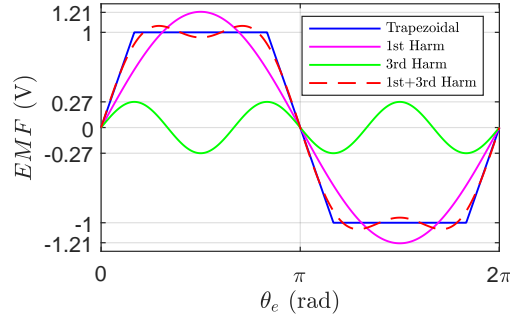
Fig. 2.6: BLDC quasi-trapezoidal flux linkage waveform and its components.

which represents the self and mutual inductances [eq. (2.37)]. As an SM-BLDC is modeled, the elements of $\mathbf{L}$ are assumed constant. Therefore, the term $(d\mathbf{L}/dt)\mathbf{I}$ from (2.12) is zero (note that salient pole machine configurations will be comprehensively studied in chapter 3).

$$\mathbf{L} = \begin{bmatrix} L_{11} & L_{12} & L_{13} & L_{14} & L_{15} \\ L_{15} & L_{11} & L_{12} & L_{13} & L_{14} \\ L_{14} & L_{15} & L_{11} & L_{12} & L_{13} \\ L_{13} & L_{14} & L_{15} & L_{11} & L_{12} \\ L_{12} & L_{13} & L_{14} & L_{15} & L_{11} \end{bmatrix}. \tag{2.37}$$

The vector $\mathbf{\Psi}_{PM} = [\Psi_1, \Psi_2, \Psi_3, \Psi_4, \Psi_5]$ represents the per-phase magnetic flux linkages generated by the permanent magnets. In a BLDC machine with a quasi-trapezoidal back-EMF distribution, the main harmonic components of the flux linkages are the first and third harmonics. As it can be observed from Fig. 2.6, the amplitude of the fundamental component is 1.21 times the total back-EMF, while the third harmonic amplitude is 0.27 times the total back-EMF. In this simulation model, only the fundamental (ψ_1) and third harmonic (ψ_3) components of the flux linkages are considered, and, for the sake of simplicity, the rest of the components are neglected.

Fig. 2.7 particularizes the per-phase electrical-circuit representation for a 5-phase BLDC machine. The voltage-controlled sources represent the back-EMF and coupling effects, as (2.38) shows. This way, the model implementation in an electric circuit simulation software becomes straightforward, as was described
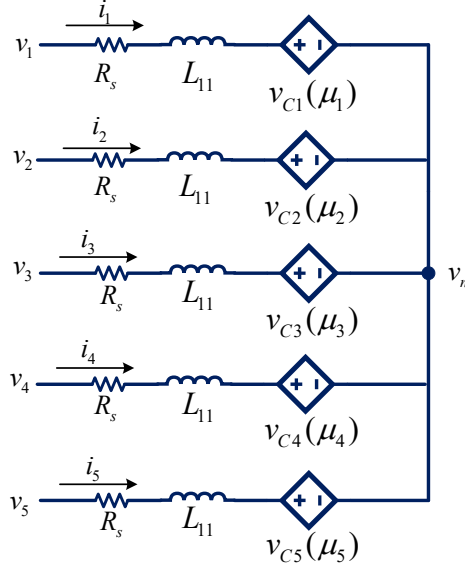
Fig. 2.7: Five phase BLDC machine model representation in the natural reference frame.

previously.

$$v_{ck} = \frac{d\Psi_k}{dt} + \sum_{j \neq k}^{5} \frac{dL_{kj}}{dt} i_j + \sum_{j \neq k}^{5} L_{jk} \frac{di_j}{dt}, \tag{2.38}$$

where $k \in [1, 2, 3, 4, 5]$.

As a surface-mounted machine is considered, the saliency/reluctant torque component is neglected. Therefore, the total torque is produced by the interaction between phase currents and magnet flux linkages. From (2.19), the torque equation is derived for this particular case:

$$T_{em} = \mathbf{I}^T \frac{d\mathbf{\Psi}_{PM}}{d\theta_m}. \tag{2.39}$$

2.3.2 Vector control of a five-phase BLDC

In order to successfully simulate the five-phase SM-BLDC in various operating points, a control system is required. However, as the control system is not
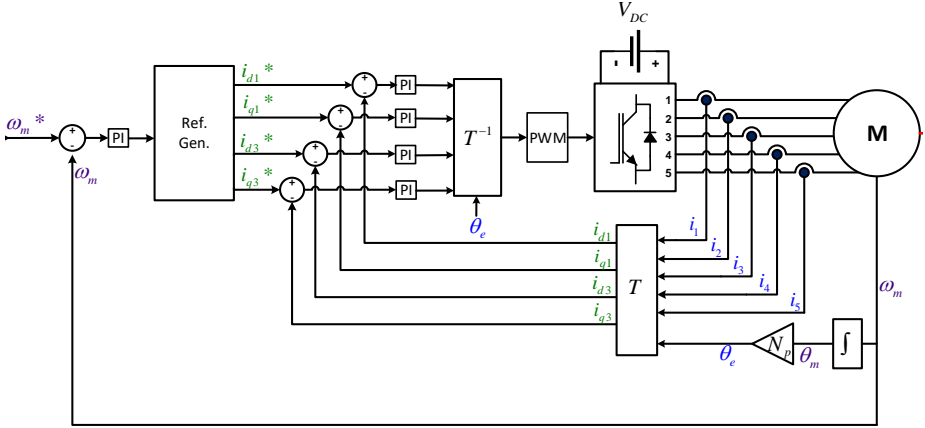
Fig. 2.8: General diagram of the vector control for a five-phase SM-BLDC.

the subject of this chapter, only a rough overview is provided. In chapter 3, a detailed description of a vector controller for six-phase machines is presented, and most of the techniques described there are adaptable to the control of five-phase machines.

Fig. 2.8 shows the general diagram of a vector controller for the five-phase machine. The control system consists of an outer speed loop, which receives the speed set-point and, using a discrete PI, determines the required electromagnetic torque at each operation instant. The inner torque loop, which is based on the well-known FOC approach, is adapted to the multiphase scenario, using PI regulators to control the four degrees of freedom of the five-phase BLDC [93,123]. This is possible thanks to the appropriate vector transformation $\mathbf{T}$ in (2.40), which is obtained by multiplying the magnitude-invariant five-phase version of matrices (2.29) and (2.32). As discussed before, $\mathbf{T}$ decomposes the vector of phase currents according to their harmonic components, making it possible to control the fundamental (i_{d1}, i_{q1}) and third harmonic (i_{d3}, i_{q3}) currents.

$$\mathbf{T} = \frac{2}{5} \begin{bmatrix} cos(\theta_e) & cos(\theta_e - 2\pi/5) & cos(\theta_e - 4\pi/5) \\ -sin(\theta_e) & -sin(\theta_e - 2\pi/5) & -sin(\theta_e - 4\pi/5) \\ cos(3\theta_e) & cos3(\theta_e - 2\pi/5) & cos3(\theta_e - 4\pi/5) \\ -sin(3\theta_e) & -sin3(\theta_e - 2\pi/5) & -sin3(\theta_e - 4\pi/5) \\ \frac{1}{2} & \frac{1}{2} & \frac{1}{2} \end{bmatrix} \cdots$$

$$\cdots \begin{bmatrix} cos(\theta_e - 6\pi/5) & cos(\theta_e - 8\pi/5) \\ -sin(\theta_e - 6\pi/5) & -sin(\theta_e - 8\pi/5) \\ cos3(\theta_e - 6\pi/5) & cos3(\theta_e - 8\pi/5) \\ -sin3(\theta_e - 6\pi/5) & -sin3(\theta_e - 8\pi/5) \\ \frac{1}{2} & \frac{1}{2} \end{bmatrix}.$$

$$(2.40)$$

Table 2.3: Optimum injection-ratio depending on the selected constraint [2, 3].

Case	Constraint	Injection ratio r_c
Case 1	$i_{q3} = 0$	$0/i_{q1}^{\dagger}$
Case 2	Same RMS value	$\dfrac{3\psi_3}{\psi_1}$
Case 3	Same amplitude	$\dfrac{\psi_1}{6\psi_1 - 9\psi_3}$

Such degrees of freedom can be exploited to increase the torque density of the machine by selecting the proper injection-ratio $r_c = i_{q3}/i_{q1}$ [2, 3, 43, 53, 54]. As shown in table 2.3, three possible current reference scenarios were considered in this section to carry out the simulations. The first case does not consider injection of third harmonic current; therefore, $i_{q1} = i_{q1}^{\dagger}$ and $i_{q3} = 0$. In the second case, the injection ratio that maximizes the generated torque while keeping the current RMS value less than or equal to the one of case 1 is considered. In the third case, the generated torque is maximized with the constraint that sets the current amplitude less than or equal to the one in case 1. In all these scenarios, the d-axis fundamental and third harmonic currents are regulated to zero, as

Table 2.4: Most relevant parameters of the simulated five-phase BLDC.

Parameter	Symbol	value
Stator Inductance	L_s	9.6 mH
Stator Resistance	R_s	1.56 Ohm
First harmonic PM flux	ψ_1	0.1314 Wb
Third harmonic PM flux	ψ_3	0.0098 Wb
Rated power	P_N	1.51 kW
Rated torque	T_N	12.1 Nm
Rated speed	ω_N	1200 RPM
Pole-pair number	N_p	9

they do not contribute to the electromagnetic torque generation, and no field weakening operation is required for the studied EMA.

2.3.3 Simulation results

In this section, software simulations have been carried out for a five-phase BLDC EMA. Table 2.4 summarizes the most significant parameters of the BLDC EMA system.

The following figures show the most significant results obtained during the extension of the EMA when current set-points are generated following the injection ratio of case 2 (table 2.3). Fig. 2.9 shows how the controller regulates the EMA extension satisfactorily (note that the speed and position results are very similar for all the three set-point generation cases considered). Fig. 2.10 shows the electromagnetic torque generated by the BLDC machine during extension. The multiphase machine degrees of freedom $(i_{d1}, i_{q1}, i_{d3}, i_{q3})$ have been commanded to achieve MTPA operation while keeping the same RMS value in the phase currents (Fig. 2.11), operating as expected.

Finally, Fig. 2.12 shows, in detail, the phase 1 current during maximum load condition for all the three current set-point generation scenarios considered in table 2.3. The amplitude of the currents for cases 2 and 3 are very similar and lower than for case 1. However, the copper losses are different for each case. For case 2, the ohmic losses are 5% lower than for case 1 while, for case 3,
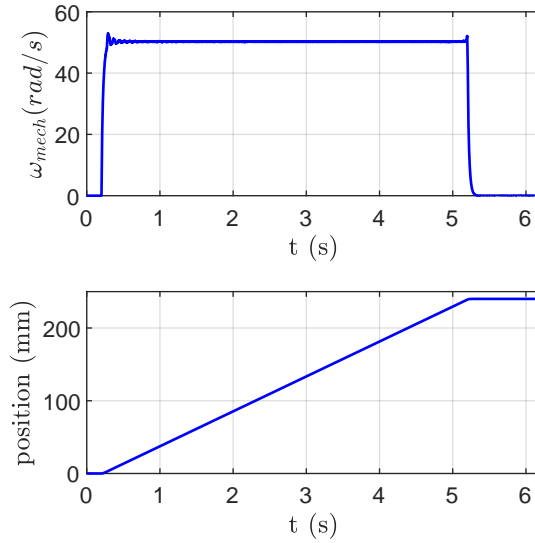
Fig. 2.9: Speed and position control during the EMA extension.
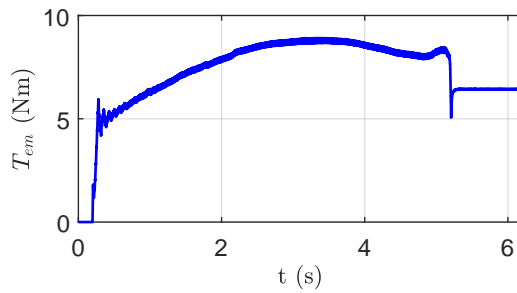

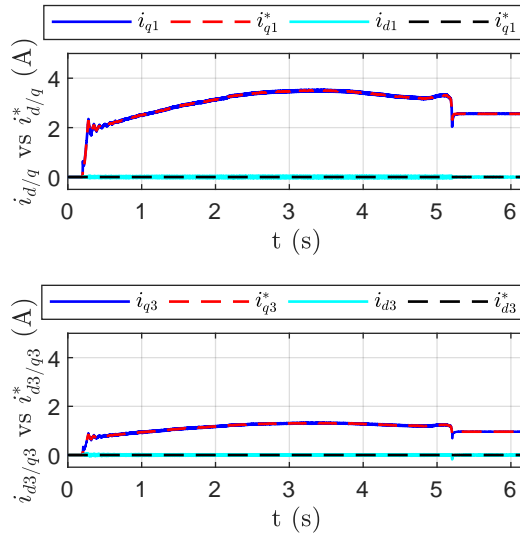Fig. 2.10: Electromagnetic torque produced by the fundamental and third harmonic components.

Fig. 2.11: Fundamental and third harmonic d- and q-axis current control.
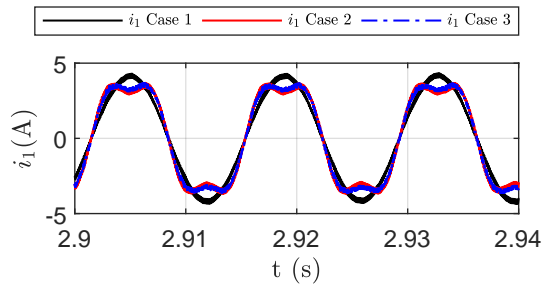
Fig. 2.12: Phase 1 current during maximum load conditions.

such losses are 4% lower than for case 1. As expected, the current set-point generation procedure of case 2 provides the lowest copper losses, since such set-points are determined taking into account the RMS value of the current.

2.4 Conclusions

Two methodologies for the development of accurate models of multiphase machines have been presented. Both methodologies have been mathematically detailed for the general case of n-phase machines.

The first methodology described the machine in its natural per-phase variables (voltage, currents, fluxes, etc.). This type of model proved to be complex and highly coupled. However, they facilitate the emulation of the behavior of the machine during electric fault conditions.

The second methodology describes the machine using fictitious variables (voltage, currents, fluxes, etc.). These variables are obtained thanks to the application of vector transformations to the natural per-phase variables. The resulting models are less complex than the previous ones. Therefore, they facilitate the design of the control system for multiphase machines.

In order to illustrate a case of use of the general modeling approach based on a per-phase or natural variable representation, a simulation platform incorporating a five-phase SM-BLDC has been presented. The results show the suitability of using this type of modeling approach for star-connected symmetrical multiphase PMSMs. However, as the main objective of this thesis is to develop novel control algorithms for multiphase machines operating under healthy conditions, in the subsequent chapters of this thesis, the vector modeling approach will be adopted.

Chapter 3

Modeling and control of dual three-phase IPMSMs

Among multiphase solutions, dual three-phase PMSMs are being especially considered for transport electrification applications. These machines have six phases arranged in two three-phase star-connected winding sets. Therefore, they pose the advantages of multiphase drives, while the transition from manufacturing and controlling three-phase drives to dual three-phase ones is relatively simple [9, 69].

In dual three-phase machine architectures, phases are symmetrically or asymmetrically distributed. Fig. 3.1 shows the asymmetrical (a) and symmetrical (b) arrangements of dual three-phase machines. In both cases, the phases inside a set are separated $2\pi/3$ radians, but the winding sets are shifted α radians [124]. For symmetrical configurations, $\alpha = \pi/3$, while, for asymmetrical arrangements, $\alpha = \pi/6$ most frequently. For the sake of simplicity, the symmetrical configuration is considered in this chapter; furthermore, the electric machine prototype used in this thesis has this particular configuration. However, all techniques described in this chapter can be easily extended to the asymmetrical configuration.

This chapter describes the modeling and torque control approaches that can be used for dual three-phase machines. First, the general methodology described in chapter 2 for modeling n-phase PMSMs is particularized. That is, the mathematical equations modeling the dynamics in the natural per-phase variables are developed. Then, two vector model approaches, *multiphase* and *double three-*
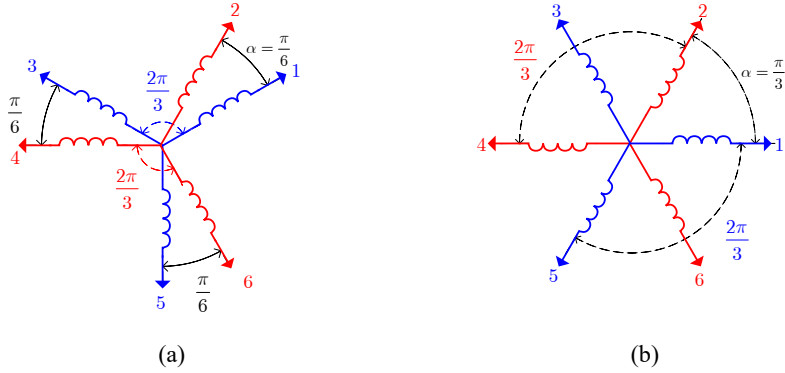
Fig. 3.1: Common winding arrangements of dual three-phase machines: (a) asymmetrical configuration, (b) symmetrical configuration.

phase, are described. These models are derived from the application of the vector transformations $\mathbf{T_1}$ and $\mathbf{T_2}$, which are, in turn, the result of multiplying a decoupling matrix by a rotation matrix, as discussed in chapter 2. The main features of each of these models are highlighted and contrasted against each other. Additionally, the high magnetic saturation phenomena characteristics of automotive IPMSMs are considered for each model.

In the next section, the diagram of a generic controller is used to introduce the required components for torque vector control. The first component is the current set point generator, the second one includes the current regulation loops, and the third one is the modulation algorithm. Each of these components is described by means of their mathematical formulations and detailed block diagrams. Furthermore, general tuning procedures for the control parameters are presented.

Finally, three particular alternatives for the vector torque control of dual three-phase IPMSMs are described. The first controller is called *double three-phase* torque controller, as it is based on the modeling approach of the same name. This control approach aims to take advantage of well-known control techniques for three-phase machines, independently controlling each winding set of the drive. The second solution, called *multiphase* torque control, is based on the model derived from the transformation $\mathbf{T_1}$. This approach utilizes techniques of multiphase machine control, like harmonic decomposition and decoupling. The third solution is novel and is named *hybrid* torque control. This solution has

been proposed by the author of this thesis and is one of the main contributions of this work. It combines the previous solutions in a convenient way to keep their advantages and mitigate their drawbacks.

3.1 Mathematical model of a symmetrical dual three-phase IPMSM

In this section, the methodology presented in chapter 2 for the general n-phase scenario is used to develop a mathematical model of a dual three-phase IPMSM. First, the mathematical model represented in natural variables is developed. Then, through vector transformation, two models in synchronous frames are described.

3.1.1 Model represented in natural machine variables

For a 6-phase machine, the stator voltage equation in the natural variable reference frame is:

$$\mathbf{V} = \mathbf{R}\mathbf{I} + \frac{d\mathbf{L}}{dt}\mathbf{I} + \mathbf{L}\frac{d\mathbf{I}}{dt} + \frac{d\mathbf{\Psi}_{PM}}{dt}, \tag{3.1}$$

where $\mathbf{V} = [v_1, v_2, v_3, v_4, v_5, v_6]^T$ and $\mathbf{I} = [i_1, i_2, i_3, i_4, i_5, i_6]^T$ are the per-phase voltages and currents, respectively. $\mathbf{R}$ is a 6×6 diagonal matrix (3.2), where each diagonal element represents the phase resistance. If all phases are assumed to be identical (same materials, an equal number of turns, and same distribution), all diagonal elements of the such matrix have the same value.

$$\mathbf{R} = \begin{bmatrix} R_s & 0 & 0 & 0 & 0 & 0 \\ 0 & R_s & 0 & 0 & 0 & 0 \\ 0 & 0 & R_s & 0 & 0 & 0 \\ 0 & 0 & 0 & R_s & 0 & 0 \\ 0 & 0 & 0 & 0 & R_s & 0 \\ 0 & 0 & 0 & 0 & 0 & R_s \end{bmatrix}. \tag{3.2}$$

On the other hand, $\mathbf{L}$ is the 6×6 stator inductance matrix (3.3). Each element L_{ij} $(i, j \in \{1, 2, \ldots, 6\})$ represents the self- $(i = j)$ and mutual-inductances $(i \neq j)$ between phases i and j. Considering the spatial distribution of the windings (Fig. 3.1), $\mathbf{L}$ is a symmetric matrix. In particular and for IPMSMs, the elements of $\mathbf{L}$ vary according to the rotor electrical angle (θ_e), as shown in Fig. 3.2(a) for L_{11} and in Fig. 3.2(b) for L_{12}. This is produced as a
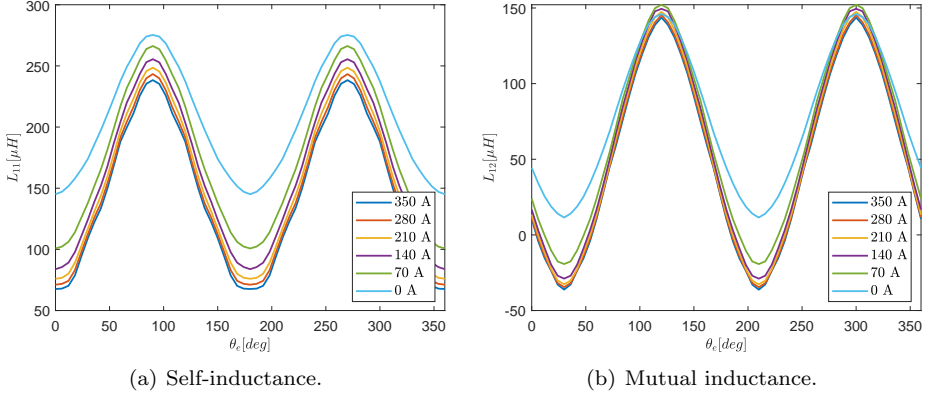
(a) Self-inductance.

(b) Mutual inductance.

Fig. 3.2: Self-inductance of phase 1 and mutual inductance between phases 1 and 2 for various peak phase currents, obtained for the prototype used in this thesis.

consequence of the variable magnetic reluctance of such rotor configuration [95]. Moreover, $\mathbf{L}$ varies with the stator currents due to magnetic saturation.

$$
\mathbf{L} = \begin{bmatrix}
L_{11} & L_{12} & L_{13} & L_{14} & L_{15} & L_{16} \\
L_{21} & L_{22} & L_{23} & L_{24} & L_{25} & L_{26} \\
L_{31} & L_{32} & L_{33} & L_{34} & L_{35} & L_{36} \\
L_{41} & L_{42} & L_{43} & L_{44} & L_{45} & L_{46} \\
L_{51} & L_{52} & L_{53} & L_{54} & L_{55} & L_{56} \\
L_{61} & L_{62} & L_{63} & L_{64} & L_{65} & L_{66}
\end{bmatrix}.
\tag{3.3}
$$

The term $\mathbf{\Psi}_{PM}$ in (3.1) is the 6-dimensional flux linkage vector ($\mathbf{\Psi}_{PM} = [\psi_1, \psi_2, \ldots, \psi_6]$) generated due to the permanent magnets. Its elements vary with θ_e and the currents (due to magnetic saturation), as can be observed in Fig. 3.3(a) and 3.3(b).

Generally, the inductances and fluxes are modeled using the data acquired from a finite element model (FEM) of the electric machine. This approach allows the straightforward modeling of the non-linear phenomena of magnetic saturation. This phenomenon implies a variation of the inductances and fluxes with the phase currents. For instance, Fig. 3.2 shows the self-inductance of phase 1 (L_{11}) and the mutual inductance between phases 1 and 2 (L_{12}) for

(a) Phase 1 flux linkage.
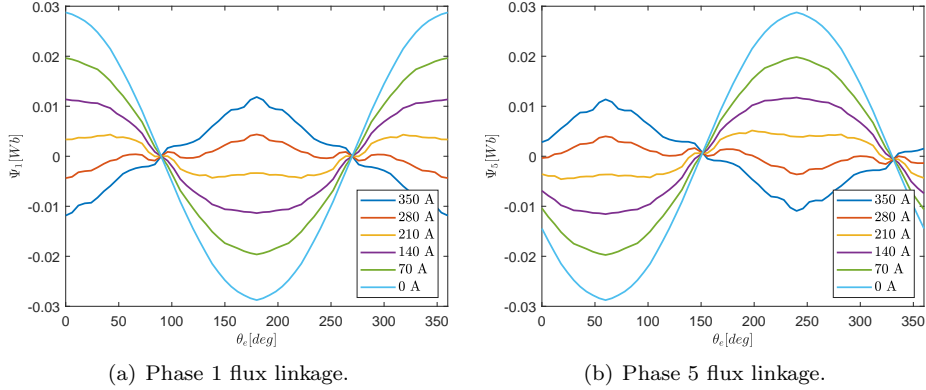
(b) Phase 5 flux linkage.

Fig. 3.3: Airgap flux linkage variations for various peak phase currents obtained for the dual three-phase IPMSM prototype used in this thesis.

various peak phase currents. Likewise, Fig. 3.3 shows the phase airgap flux linkage variation for various peak currents.

Equation (3.1), along with the flux and inductance FEM data, allows the dynamic modeling of the voltages and currents of the machine. The next step is to model the electromagnetic torque produced by the machine. This model can be derived from the conventional electrical input power equation ($P = \mathbf{I}^T \mathbf{V}$). First, the non-torque producing terms are removed (copper and magnetic losses) [94]. Finally, the expression that relates output power and torque is used ($P = \omega_{mec} T_{em}$) to get the electromagnetic torque equation:

$$T_{em} = \frac{1}{2} \mathbf{I}^T \frac{d\mathbf{L}}{d\theta_m} \mathbf{I} + \mathbf{I}^T \frac{\mathbf{\Psi}_{PM}}{d\theta_m}. \tag{3.4}$$

Thus, (3.4) completes the mathematical representation of the electric machine. However, such a model is complex and highly coupled, not suitable for control system design. Therefore, vector transformations are applied to simplify the mathematical representation of the model by decoupling and eliminating dependence on rotor position. These transformations allow the design and implementation of the well-known FOC technique [64, 98, 124, 125].

3.1.2 Model represented in synchronous reference frames

Two vector transformation approaches are commonly considered for dual three-phase IPMSM modeling. The first is a generalization of the magnitude invariant Clarke and Park transformation matrices for symmetrical multiphase machines. The second transformation matrix involves the application of the conventional three-phase Clarke and Park transformations to each three-phase set. Based on these matrix transformations, the multiphase and the double three-phase modeling approaches were developed [64, 124–126].

Multiphase modeling approach

If the multiphase modeling approach is followed, the matrix transformation $\mathbf{T_1}$ is considered. $\mathbf{T_1}$ is obtained by multiplying the decoupling matrix $\mathbf{C_1}$ in (3.5) and the rotating matrix $\mathbf{P_1}$ in (3.6), i.e., $\mathbf{T_1} = \mathbf{P_1}\mathbf{C_1}$. Following the ideas presented in chapter 2, transformation $\mathbf{C_1}$ decomposes the 6-dimensional per-phase space into two static orthogonal planes and two 1-dimension homopolar spaces. $\mathbf{P1}$ consists of two rotation transformations; the first sub-matrix rotates vectors at the synchronous electrical speed ω_e. The second sub-matrix rotates vectors at five times the electrical speed $(5\omega_e)$.

$$\mathbf{C_1} = \frac{1}{3} \begin{bmatrix} 1 & cos(\alpha) & cos(2\alpha) & cos(3\alpha) & cos(4\alpha) & cos(5\alpha) \\ 0 & sin(\alpha) & sin(2\alpha) & sin(3\alpha) & sin(4\alpha) & sin(5\alpha) \\ 1 & cos(2\alpha) & cos(4\alpha) & cos(6\alpha) & cos(8\alpha) & cos(10\alpha) \\ 0 & sin(2\alpha) & sin(4\alpha) & sin(6\alpha) & sin(8\alpha) & sin(10\alpha) \\ 1 & 0 & 1 & 0 & 1 & 0 \\ 0 & 1 & 0 & 1 & 0 & 1 \end{bmatrix}, \qquad (3.5)$$

$$\mathbf{P_1} = \begin{bmatrix} cos(\theta_e) & sin(\theta_e) & 0 & 0 & 0 & 0 \\ -sin(\theta_e) & cos(\theta_e) & 0 & 0 & 0 & 0 \\ 0 & 0 & cos(5\theta_e) & sin(5\theta_e) & 0 & 0 \\ 0 & 0 & -sin(5\theta_e) & cos(5\theta_e) & 0 & 0 \\ 0 & 0 & 0 & 0 & 1 & 0 \\ 0 & 0 & 0 & 0 & 0 & 1 \end{bmatrix}, \qquad (3.6)$$

where $\alpha = \pi/3$, as previously stated, is the spatial separation between adjacent phases in symmetrical arrangements. The transformation $\mathbf{T_1}$ allows to decouple and decompose the 6-dimension phase vectors (current, voltages, and fluxes) according to their harmonic components [102, 124]. If the homopolar components
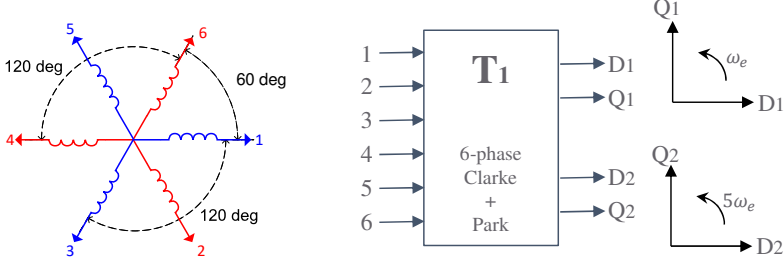
Fig. 3.4: Subspace decomposition by applying vector transformation $\mathbf{T_1}$.

are not considered, $\mathbf{T_1}$ decomposes the phase variables in two decoupled subspaces. The two-dimensional reference frame $D_1 - Q_1$ contains the fundamental components, while the subspace $D_2 - Q_2$ comprises the 5th and 7th harmonics (Fig. 3.4) [124, 125]. For instance, (3.7) shows the application of $\mathbf{T_1}$ to the phase currents.

$$
\begin{bmatrix} i_{D1} \\ i_{Q1} \\ i_{D2} \\ i_{Q2} \\ i_{H1} \\ i_{H2} \end{bmatrix} = \frac{1}{3} \begin{bmatrix} cos(\theta_e) & cos(\theta_e - \alpha) & cos(\theta_e - 2\alpha) \\ -sin(\theta_e) & -sin(\theta_e - \alpha) & -sin(\theta_e - 2\alpha) \\ cos(5\theta_e) & cos(5\theta_e - 2\alpha) & cos(5\theta_e - 4\alpha) \\ -sin(5\theta_e) & -sin(5\theta_e - 2\alpha) & -sin(5\theta_e - 4\alpha) \\ 1 & 0 & 1 \\ 0 & 1 & 0 \end{bmatrix} \cdots
$$
$$
\cdots \begin{bmatrix} cos(\theta_e - 3\alpha) & cos(\theta_e - 4\alpha) & cos(\theta_e - 5\alpha) \\ -sin(\theta_e - 3\alpha) & -sin(\theta_e - 4\alpha) & -sin(\theta_e - 5\alpha) \\ cos(5\theta_e - 6\alpha) & cos(5\theta_e - 8\alpha) & cos(5\theta_e - 10\alpha) \\ -sin(5\theta_e - 6\alpha) & -sin(5\theta_e - 8\alpha) & -sin(5\theta_e - 10\alpha) \\ 0 & 1 & 0 \\ 1 & 0 & 1 \end{bmatrix} \begin{bmatrix} i_1 \\ i_2 \\ i_3 \\ i_4 \\ i_5 \\ i_6 \end{bmatrix}.
$$
$$(3.7)$$

The next step is to apply the transformation $\mathbf{T_1}$ to (3.1) and (3.4). This way, the following vector model is obtained:

$$
v_{D1} = R_s i_{D1} + L_{D1}\frac{di_{D1}}{dt} - \omega_e L_{Q1} i_{Q1},
$$
$$
v_{Q1} = R_s i_{Q1} + L_{Q1}\frac{di_{Q1}}{dt} + \omega_e(L_{D1} i_{D1} + \psi_{PM1}),
$$
$$(3.8)$$

$$v_{D2} = R_s i_{D2} + L_{D2}\frac{di_{D2}}{dt} - 5\omega_e L_{Q2} i_{Q2},$$

$$v_{Q2} = R_s i_{Q2} + L_{Q2}\frac{di_{Q2}}{dt} + 5\omega_e(L_{D2} i_{D2} + \psi_{PM5}), \tag{3.9}$$

$$T_{em} = 3N_p\left[\psi_{PM1}i_{Q1} + (L_{D1} - L_{Q1})i_{D1}i_{Q1}\right], \tag{3.10}$$

where $\mathbf{V}_{DQ} = \mathbf{T_1}\mathbf{V} = [v_{D1}, v_{Q1}, v_{D2}, v_{Q2}, v_{H1}, v_{H2}]$ are the transformed per-phase stator voltages. $\mathbf{I}_{DQ} = \mathbf{T_1}\mathbf{I} = [i_{D1}, i_{Q1}, i_{D2}, i_{Q2}, i_{H1}, i_{H2}]$ and $\mathbf{\Psi}_{DQ} = \mathbf{T_2}\mathbf{\Psi}_{PM} = [0, \psi_{PM1}, 0, \psi_{PM5}, 0, 0]$ are the per-phase stator currents and permanent magnet fluxes represented in the $D_1 - Q_1$ and $D_2 - Q_2$ synchronous frames. Due to the star connection and assuming balanced three-phase sets, the homopolar components are neglected ($v_{H1}, v_{H2}, i_{H1}, i_{H2}$). The inductance matrix, once transformed, is as follows:

$$\mathbf{L}_{DQ} = \mathbf{T_1}\mathbf{L}\mathbf{T_1}^{-1} = \begin{bmatrix} L_{D1} & 0 & 0 & 0 & 0 & 0 \\ 0 & L_{Q1} & 0 & 0 & 0 & 0 \\ 0 & 0 & L_{D2} & 0 & 0 & 0 \\ 0 & 0 & 0 & L_{Q2} & 0 & 0 \\ 0 & 0 & 0 & 0 & L_{H1} & 0 \\ 0 & 0 & 0 & 0 & 0 & L_{H2} \end{bmatrix}. \tag{3.11}$$

This vector model shows that both planes $D_1 - Q_1$ and $D_2 - Q_2$ are decoupled. These equations are quite similar to those of a three-phase IPMSM. The main difference is that the $D_2 - Q_2$ plane rotates at five times the angular speed of the $D_1 - Q_1$ plane (see chapter 2). The parameters L_{D1}, L_{Q1}, ψ_{PM1}, L_{D2}, L_{Q2} and ψ_{PM5} can be obtained by computing the per-phase finite element model (FEM) flux data. For example, the application of $\mathbf{T_1}$ to FEM data can be observed in Fig. 3.5 for L_{D1}, L_{Q1} and ψ_{PM1}. As expected, these parameters vary according to i_{D1} and i_{Q1} (magnetic saturation). Additionally, from (3.10), it is deduced that torque can be controlled by only regulating the $D_1 - Q_1$ plane currents. Therefore, the optimal current references are easier to calculate, with the advantage that cross-coupling between the two three-phase sets is considered [127].

Double three-phase modeling approach

If the double three-phase modeling approach is followed, the matrix transformation $\mathbf{T_2}$ is considered. This matrix is obtained by multiplying matrices $\mathbf{C_2}$ and $\mathbf{P2}$. As shown in (3.12), Matrix $\mathbf{C_2}$ is composed of two three-phase Clarke

(a) L_{D1}.

(b) L_{Q1}.

(c) ψ_{PM1}.
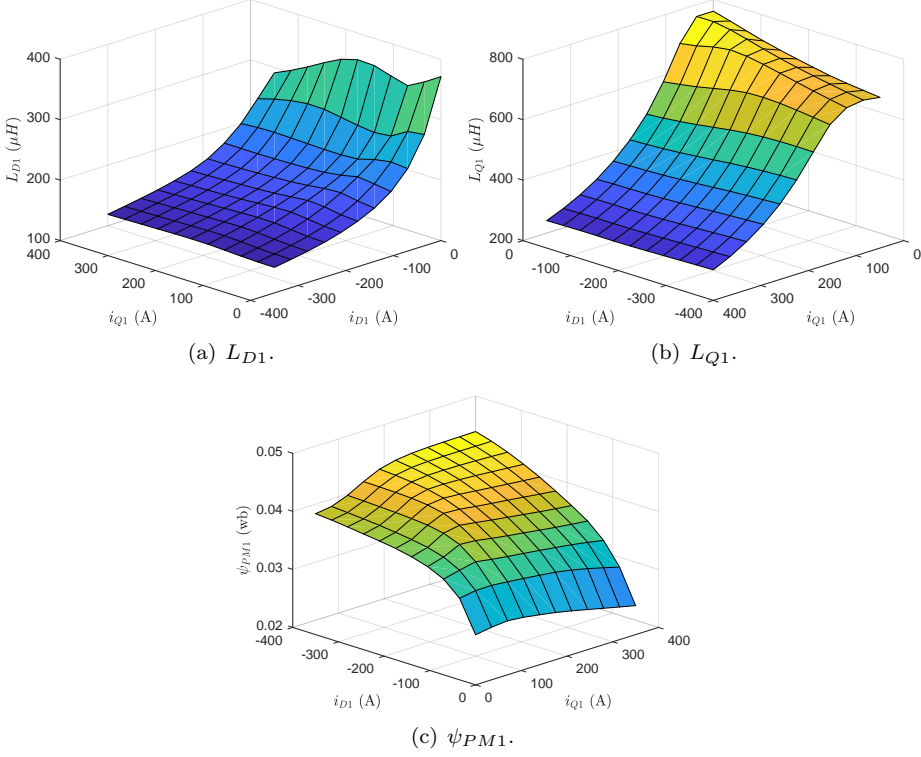
Fig. 3.5: L_{D1}, L_{Q1} and ψ_{PM1} after the application of $\mathbf{T_1}$ over the per-phase FEM data of the dual three-phase IPMSM prototype used in this thesis.

transformations. Following the ideas presented in chapter 2, this transformation decomposes the 6-dimensional per-phase space into two static planes, in which horizontal axes are aligned to phases 1 and 2, and has two 1-dimension homopolar spaces. **P2** consists of two three-phase rotation transformations, shifted α radians one from each other, as shown in (3.13). In this case, both transformed planes rotate at the synchronous electrical speed ω_e.
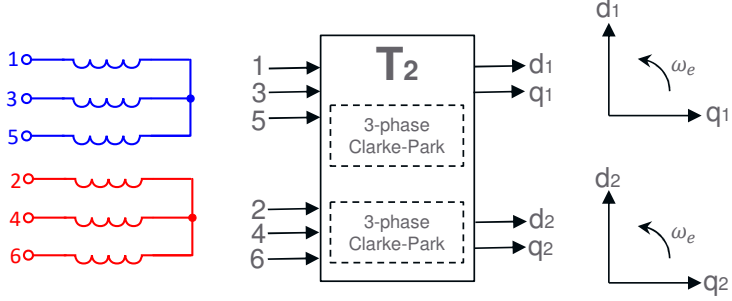
Fig. 3.6: Subspace decomposition by transformation $\mathbf{T_2}$.

$$\mathbf{C_2} = \frac{2}{3} \begin{bmatrix} 1 & cos(2\alpha) & cos(4\alpha) & 0 & 0 & 0 \\ 0 & sin(2\alpha) & sin(4\alpha) & 0 & 0 & 0 \\ 0.5 & 0.5 & 0.5 & 0 & 0 & 0 \\ 0 & 0 & 0 & 1 & cos(2\alpha) & cos(4\alpha) \\ 0 & 0 & 0 & 0 & sin(2\alpha) & sin(4\alpha) \\ 0 & 0 & 0 & 0.5 & 0.5 & 0.5 \end{bmatrix}, \tag{3.12}$$

$$\mathbf{P_2} = \begin{bmatrix} cos(\theta_e) & sin(\theta_e) & 0 & 0 & 0 & 0 \\ -sin(\theta_e) & cos(\theta_e) & 0 & 0 & 0 & 0 \\ 0 & 0 & 1 & 0 & 0 & 0 \\ 0 & 0 & 0 & cos(\theta_e - \alpha) & sin(\theta_e - \alpha) & 0 \\ 0 & 0 & 0 & -sin(\theta_e - \alpha) & cos(\theta_e - \alpha) & 0 \\ 0 & 0 & 0 & 0 & 0 & 1 \end{bmatrix}. \tag{3.13}$$

As Fig. 3.6 shows, $\mathbf{T_2}$ decomposes the 6-dimension phase vectors into two coupled subspaces. For instance, (3.14) shows the application of $\mathbf{T_2}$ to the phase currents. The $d_1 - q_1$ plane contains the information related to the first three-phase set, and the $d_2 - q_2$ plane is the one related to the second [64]. Therefore, this transformation allows a straightforward and independent control of each three-phase currents [126, 128].

82

$$
\begin{bmatrix} i_{d1} \\ i_{q1} \\ i_{h1} \\ i_{d2} \\ i_{q2} \\ i_{h2} \end{bmatrix} = \frac{2}{3} \begin{bmatrix} cos(\theta_e) & cos(\theta_e - 2\alpha) & cos(\theta_e - 4\alpha) \\ -sin(\theta_e) & -sin(\theta_e - 2\alpha) & -sin(\theta_e - 4\alpha) \\ 0.5 & 0.5 & 0.5 \\ 0 & 0 & 0 \\ 0 & 0 & 0 \\ 0 & 0 & 0 \end{bmatrix} \cdots
$$

$$
\cdots \begin{matrix} 0 & 0 & 0 \\ 0 & 0 & 0 \\ 0 & 0 & 0 \\ cos(\theta_e - \alpha) & cos(\theta_e - 3\alpha) & cos(\theta_e - 5\alpha) \\ -sin(\theta_e - \alpha) & -sin(\theta_e - 3\alpha) & -sin(\theta_e - 5\alpha) \\ 0.5 & 0.5 & 0.5 \end{matrix} \begin{bmatrix} i_1 \\ i_3 \\ i_5 \\ i_2 \\ i_4 \\ i_6 \end{bmatrix}. \tag{3.14}
$$

Similarly, the result of applying $\mathbf{T_2}$ (Fig. 3.6) over (3.1) and (3.4) is:

$$
\begin{aligned}
v_{d1} =& R_s i_{d1} + L_d \frac{di_{d1}}{dt} - \omega_e L_q i_{q1} + M_d \frac{di_{d2}}{dt} - \omega_e M_q i_{q2}, \\
v_{q1} =& R_s i_{q1} + L_q \frac{di_{q1}}{dt} + \omega_e L_d i_{d1} + M_q \frac{di_{q2}}{dt} + \omega_e M_d i_{d2} \\
& + \omega_e \psi_{PM},
\end{aligned} \tag{3.15}
$$

$$
\begin{aligned}
v_{d2} =& R_s i_{d2} + L_d \frac{di_{d2}}{dt} - \omega_e L_q i_{q2} + M_d \frac{di_{d1}}{dt} - \omega_e M_q i_{q1}, \\
v_{q2} =& R_s i_{q2} + L_q \frac{di_{q2}}{dt} + \omega_e L_d i_{d2} + M_q \frac{di_{q1}}{dt} + \omega_e M_d i_{d1} \\
& + \omega_e \psi_{PM},
\end{aligned} \tag{3.16}
$$

$$
\begin{aligned}
T_{em} =& \frac{3}{2} N_p [\psi_{PM}(i_{q1} + i_{q2}) + (L_d - L_q)(i_{d1}i_{q1} + i_{d2}i_{q2}) \\
& + (M_d - M_q)(i_{d1}i_{q2} + i_{d2}i_{q1})],
\end{aligned} \tag{3.17}
$$

where $\mathbf{V}_{dq} = \mathbf{T_2 V} = [v_{d1}, v_{q1}, v_{h1}, v_{d2}, v_{q2}, v_{h2}]$ are the per-phase stator voltages in the $d_1 - q_1$ and $d_2 - q_2$ reference frame. $\mathbf{I}_{dq} = \mathbf{T_2 I} = [i_{d1}, i_{q1}, i_{h1}, i_{d2}, i_{q2}, i_{h2}]$, and $\mathbf{\Psi}_{dq} = \mathbf{T_2 \Psi}_{PM} = [0, \psi_{PM}, 0, 0, \psi_{PM}, 0]$ are the stator per-phase currents and permanent magnet fluxes represented in the $d_1 - q_1$ and $d_2 - q_2$ frames. The transformation of the inductance matrix is as follows:

$$\mathbf{L}_{dq} = \mathbf{T_2 L T_2}^{-1} = \begin{bmatrix} L_d & 0 & 0 & M_d & 0 & 0 \\ 0 & L_q & 0 & 0 & M_q & 0 \\ 0 & 0 & L_h & 0 & 0 & 0 \\ M_d & 0 & 0 & L_d & 0 & 0 \\ 0 & M_q & 0 & 0 & L_q & 0 \\ 0 & 0 & 0 & 0 & 0 & L_h \end{bmatrix}. \tag{3.18}$$

In this model, the $d_1 - q_1$ and $d_2 - q_2$ planes are coupled by the terms M_d and M_q. Therefore, the equations of voltages, currents, and torque are more complex than those of a three-phase machine. Another feature of applying $\mathbf{T_2}$ is that both planes rotate at the same speed, but there is a $\pi/3$ offset between them. Both planes can produce torque, as shown by (3.17). The application of $\mathbf{T_2}$ to the FEM data of the IPMSM prototype used in this thesis can be observed in Fig. 3.7. In this case, the model parameters vary according to i_{d1}, i_{q1}, i_{d2} and i_{q2} (magnetic saturation).

Note that plane decoupling is not possible when the well-known Clarke-Park three-phase transformation, here called $\mathbf{T_2}$, is applied to each three-phase set [127, 128]. However, this vector transformation facilitates the independent regulation of the power consumed (or delivered during regenerative braking) by each three-phase set. This feature will be crucial for the novel control algorithm proposed in chapter 4.

3.2 Components of vector torque controllers for dual three-phase IPMSMs

Fig. 3.8 shows the block diagram of a generic vector torque control algorithm for dual three-phase machines fed by a six-leg two-level inverter. In this case, the required torque is provided through the regulation of vector transformed ($\mathbf{T_V}$) per-phase stator currents. First, the current set-point generator block provides the four reference currents, in the synchronous frame ($d - q$), to the current regulators. Next, the current control algorithm computes the four stator voltage references v_{dq}^* from the tracking error between current references and vector-transformed per-phase currents. After, these four voltages are transformed into six per-phase voltages and fed to the PWM block. Finally, the twelve inverter firing signals are computed and fed to the power converter. Below, a brief description of each of these blocks' functions is provided.

(a) L_d.
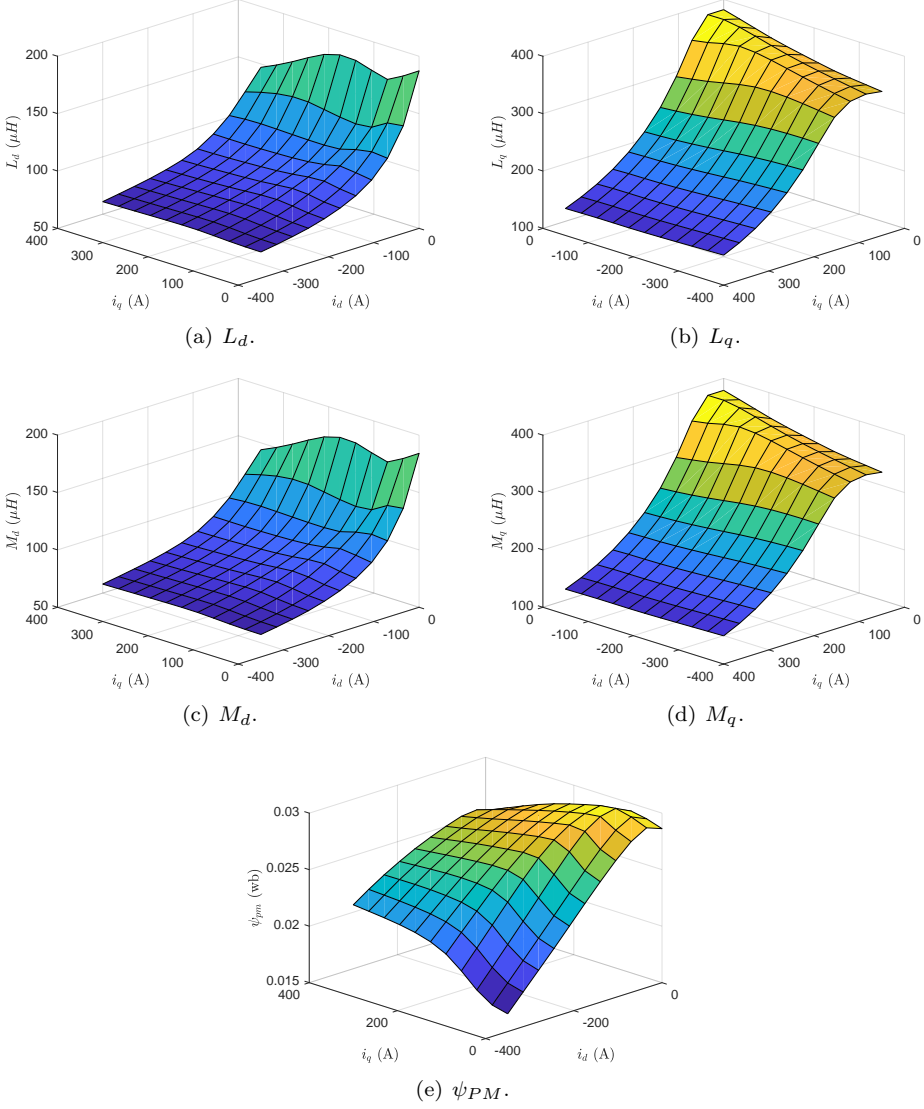

(b) L_q.

(c) M_d.

(d) M_q.

(e) ψ_{PM}.

Fig. 3.7: L_d, L_q, M_d, M_q and ψ_{PM} after the application of $\mathbf{T_2}$ over the per-phase FEM data of the dual three-phase IPMSM prototype used in this thesis.
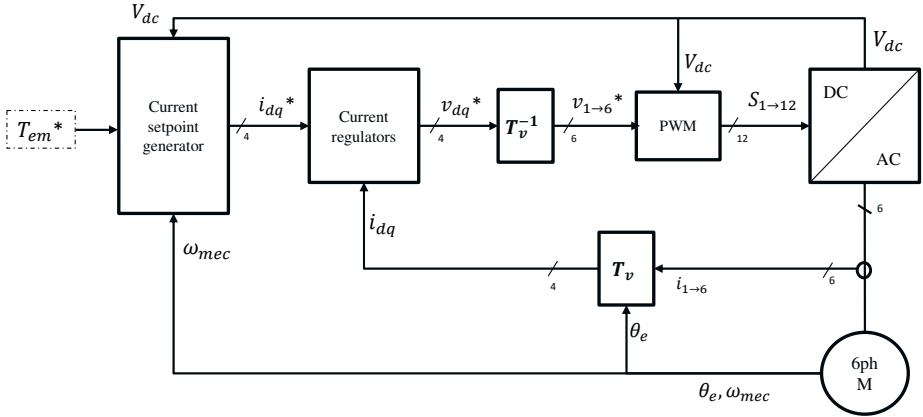
Fig. 3.8: Block diagram of a vector control algorithm for dual three-phase machines.

3.2.1 Current set-point generation

This block generates the optimum current set-points for the required torque and actual operating point. In highly saturated IPMSM drives, a simple solution with a relatively low computational burden relies on precalculating these references and storing them into Look-up tables (LUTs) [20, 129]. In general, up to 4D-LUTs would be required for automotive IPMSMs, as the optimal current set-points depend on the reference torque, dc-link voltage, rotor temperature, and mechanical speed. However, rotor temperature is not considered in industrial applications, as its precise estimation is complex [130]. In addition, the LUTs are calculated for a specific set of electrical parameters, and control can be eventually lost in Field Weakening (FW) if significant parameter variations due to machine aging or manufacturing tolerances occur [20, 129, 131].

LUT dimensions can be reduced to only two (speed and torque) through speed normalization, as there is a linear relationship between two torque-speed curves computed for different values of the dc-link voltage (Fig. 3.9). The utilization of 2D LUTs allows reducing the computational burden and the required memory storage. In addition, a Voltage Constraint Tracking (VCT) feedback controller can be incorporated to impose the robustness of the set-point generation block against significant electrical parameter deviations from the theoretical ones [20, 129, 131]. Fig. 3.10 shows the speed normalization and VCT

blocks. First, the speed is normalized by the ratio between the nominal voltage (V_{dc}^{norm}) and the actual voltage (V_{dc}). Then, the goal of the VCT is to maintain the stator voltage vector close to the voltage limit margin during field weakening operation. To achieve this, the VCT varies the virtual mechanical speed fed to the 2D-LUTs according to the error produced between the reference voltage v_s^* (from current regulators) and the voltage limit ($V_{dcmax} = V_{dc}/\sqrt{3}$) [20,129,131].

For the implementation of the VCT algorithm, constants k_v and k_{vct} need to be defined. k_v represents a security margin, and it is set with a value from $0.8 < k_v < 1$ to ensure that the voltage limit is never reached. The constant $k_{vct} > 0$ is experimentally tuned to adjust the dynamics of the VCT regulator. Therefore, this VCT loop does not require the knowledge of any machine parameter, providing additional robustness to the well-known LUT-based set-point generation technique under parameter variations or uncertainties.

The modified speed (ω_{VCT}) and torque set-point (T_{em}^*) are the inputs to the 2D-LUTs. The LUTs are the result of optimizing the current references for the operating zones of the machine. Fig. 3.11 shows the four optimum operating regions for a dual three-phase IPMSM:

- Maximum Torque Per Ampere (MTPA).

- Field Weakening (FW) at constant-torque.

- FW on max-current.

- Maximum Torque Per Voltage (MTPV).

Fig. 3.11(a) shows the operation regions in the torque vs. speed plane, i.e., this figure illustrates the expected torque trajectory when the speed is increased. Fig. 3.11(b) illustrates a $D-Q$-axis current vector trajectory through the entire speed range of the machine.

In the following, the mathematical conditions to be met at each operation region are summarized. Next, a programmatic algorithm to precalculate the 2-D LUTs for a dual three-phase IPMSM is described. Then, this algorithm is used to calculate the 2-D LUTs for the prototype used in this thesis.

Maximum torque per ampere (MTPA) region

As the name implies, each point in this region is the current vector that produces a given torque and whose magnitude is the smallest possible. Therefore, the MTPA curve can be computed by solving the optimization problem of (3.19) for each reference torque allowed for the electric machine.
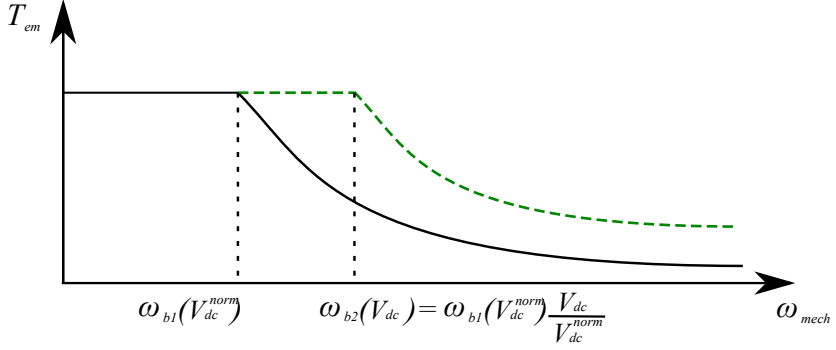
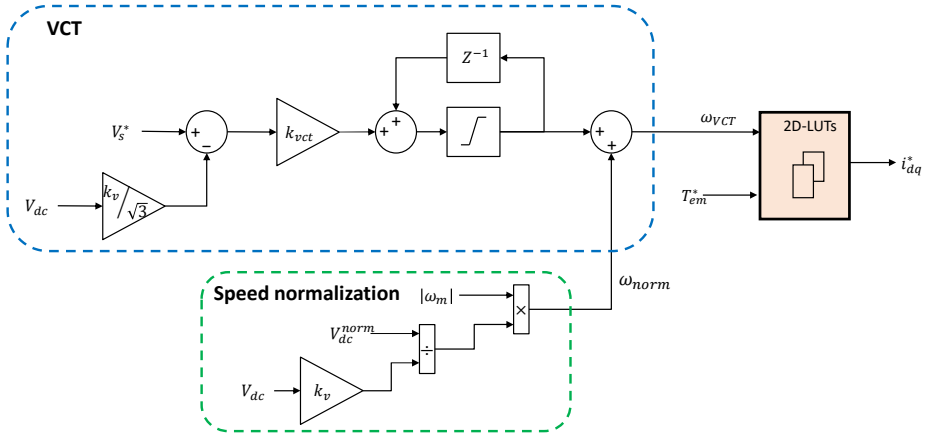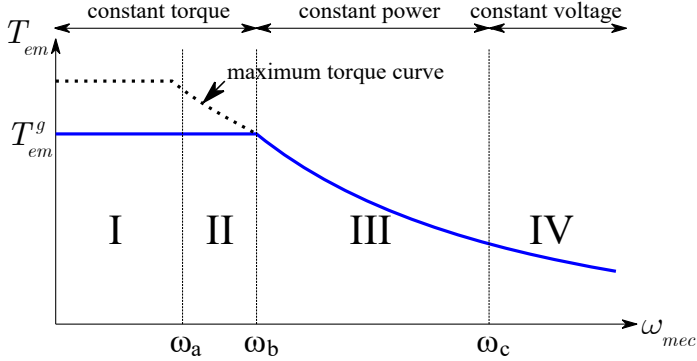Fig. 3.9: V_{dc} vs torque-speed curve.

Fig. 3.10: Block diagram of the VCT feedback loop, including speed normalization.

$$\begin{aligned} \min \quad & \|\mathbf{I}\|, \\ \text{s.t.} \quad & T_{em} = T_{em}^g, \\ & \|\mathbf{I}\| \leq i_{max}, \\ & \|\mathbf{V}\| \leq V_{dcmax}, \end{aligned} \tag{3.19}$$

88

(a) Operation regions.
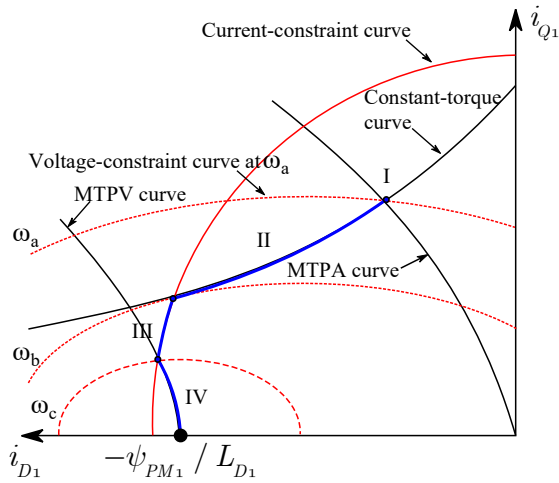
(b) $D-Q$-axis current vector trajectory for all the operation regions.

Fig. 3.11: Optimum operating zones for an IPMSM: MTPA (I), FW constant torque (II), FW max-current (III), and MTPV (IV).

where i_{max} is the maximum current that the drive (electric machine and/or power electronics) can withstand without suffering any damage. This optimization is easier to solve using the vector representation $\mathbf{T_1}$, as only i_{D1} and i_{Q1}

components are responsible for the production of torque. In this scenario, the optimization problem can be expressed as:

$$\min_{i_{D1}, i_{Q1}} \quad \sqrt{i_{D1}^2 + i_{Q1}^2},$$

$$\text{s.t.} \quad 3N_p \left[\psi_{PM1} i_{Q1} + (L_{D1} - L_{Q1}) i_{D1} i_{Q1}\right] = T_{em}^g,$$

$$\sqrt{i_{D1}^2 + i_{Q1}^2} \leq i_{max},$$

$$\sqrt{v_{D1}^2 + v_{Q1}^2} \leq V_{dcmax}. \tag{3.20}$$

When magnetic saturation is considered (Fig. 3.5), (3.20) cannot be analytically solved. However, mathematical software with optimization tools like MATLAB allows solving this problem in a straightforward manner. The computation of the MTPA curve is described and illustrated in the next section for the dual three-phase IPMSM prototype used in this thesis.

Fig. 3.11(b) shows an example of an MTPA curve. For a given torque, the current vector is placed in point I of the MTPA curve. There, the machine can operate while $\omega_{mec} \leq \omega_a$. The machine reaches the voltage constraint curve at ω_a, and if the speed increases, the drive must operate in the FW region.

FW at constant-torque region

This region consists of several curves, where each curve is a set of current vectors that produce a given torque. As Fig. 3.11(b) shows, these curves are constrained between the MTPA curve and the current constraint curve ($\sqrt{i_{D1}^2 + i_{Q1}^2} = i_{max}$). When using the $\mathbf{T_1}$ representation, the curves that comprise this region can be expressed as:

$$\forall \quad (i_{D1}, i_{Q1}),$$

$$\text{s.t.} \quad 3N_p \left[\psi_{PM1} i_{Q1} + (L_{D1} - L_{Q1}) i_{D1} i_{Q1}\right] = T_{em}^g,$$

$$i_{D1} < i_{D1}^{MTPA},$$

$$\sqrt{i_{D1}^2 + i_{Q1}^2} \leq i_{max},$$

$$\sqrt{v_{D1}^2 + v_{Q1}^2} \leq V_{dcmax}, \tag{3.21}$$

where, i_{D1}^{MTPA} is the $D1$-axis component of the MTPA point for a given torque (T_{em}^g). As shown in Fig.3.11(b), the optimum trajectories slide over a constant-torque curve when the speed goes from ω_a to ω_b. While operating in regions I

and II, the machine is able to produce constant torque when the speed increases [Fig. 3.11(a)].

FW on max-current region

Once the optimal FW trajectory reaches the maximum current circle, it cannot continue to slide over the constant torque curve without damaging the electric drive. Therefore, the optimum trajectory slides over the current constraint curve [Fig. 3.11(b), region III]. The FW on max-current curve can be expressed as:

$$
\begin{aligned}
\forall \quad & (i_{D1}, i_{Q1}) \\
\text{s.t.} \quad & \sqrt{i_{D1}^2 + i_{Q1}^2} = i_{max} \\
& i_{D1} < i_{D1}^{Tcte} \\
& i_{Q1} \geq i_{Q1}^{MTPV},
\end{aligned}
\tag{3.22}
$$

where i_{D1}^{Tcte} is the $D1$-axis component of the interception point between the constant-torque and the current-constraint curves for a given torque (T_{em}^g), and i_{Q1}^{MTPV} is the $Q1$-axis component of the interception point between the MTPV and current-constraint curves. As shown in Fig.3.11, the optimum trajectories slide over the current-constraint curve when the speed goes from ω_b to ω_c. While operating in region III, the machine is not able to produce a constant torque when the speed increases but keeps a constant power.

For some torque values, the current vector trajectory passes directly from region II to IV. This happens for low torques, whose torque-constant curves intersect first with the MTPV curve rather than with the maximum current circle.

Maximum torque per volt (MTPV) region

As the name implies, each point in this region is the current vector that produces the maximum torque when the voltage (or flux) magnitude is the maximum allowed. Therefore, the MTPV curve can be computed by solving the optimization problem of (3.23).

$$
\begin{aligned}
\max \quad & T_{em} \\
\text{s.t.} \quad & \|\mathbf{V}\| = V_{dcmax}, \\
& \|\mathbf{I}\| \leq i_{max}.
\end{aligned}
\tag{3.23}
$$

This optimization problem is easier to solve using the vector representation $\mathbf{T_1}$. Considering this reference frame, the optimization problem can be described

as follows:

$$\max_{i_{D1}, i_{Q1}} \quad 3N_p \left[\psi_{PM1} i_{Q1} + (L_{D1} - L_{Q1}) i_{D1} i_{Q1} \right],$$

$$\text{s.t.} \quad \sqrt{v_{D1}^2 + v_{Q1}^2} = V_{dcmax}, \tag{3.24}$$

$$\sqrt{i_{D1}^2 + i_{Q1}^2} \leq i_{max}.$$

To solve this problem, (3.8) is used to express v_{D1} and v_{Q1} in terms of i_{D1} and i_{Q1}. Furthermore, (3.8) shows that the MTPV curve approaches $i_{D1} = -\psi_{PM1}/L_{D1}$ as i_{Q1} approximates to zero, as shown in Fig.3.11(b). Depending on the specific parameters of a machine, it is possible that $\psi_{PM1}/L_{D1} \leq -i_{max}$. Then, the drive cannot operate in region IV, and region III is extended up to $i_{Q1} = 0$.

In this region, the optimum trajectory slides over the MTPV curve when the speed exceeds ω_c (Fig. 3.11). While operating in zone IV, the machine is not able to produce a constant torque when the speed increases but keeps a constant voltage magnitude.

Offline programmatic calculation of 2D-LUTs

Following the previous mathematical description of the IPMSM operation regions, a programmatic algorithm for the offline calculation of the 2D-LUTs was developed. The algorithm is quite flexible and allows the calculation of LUTs both for three-phase and multiphase machines, using the appropriate vector representation. For the sake of simplicity, the steps of the algorithm in the case of adopting the *multiphase* model are described below. However, the adaptation to other vector representations is straightforward. Thus, the model represented by (3.8), (3.9) and (3.10) is considered. In addition, the optimum current vectors calculation requires using the magnetic characteristics of the machine, either measured [132–134] or computed by FEM (Fig. 3.5). Since i_{D1} and i_{Q1} are the ones in charge of producing torque, only two LUTs are needed. The computational steps followed are:

1. Using the FEM/measured data and (3.10), the electromagnetic torque matrix is calculated for all available i_{D1} and i_{Q1} combinations. Fig. 3.12(a) presents the computed electromagnetic torque as a function of i_{D1} and i_{Q1} of the IPMSM prototype used in this thesis.

2. For each T_{em}^*, from $T_{min} = 0$ to T_{max}, the constant torque curve is computed. Then, within this curve, the MTPA point is found, i.e., the vector

(a) Torque map.

(b) Constant-torque curves.

(c) MTPA, i Max, and MTPV.

(d) Optimal trajectories.

(e) i_{D1} LUT.
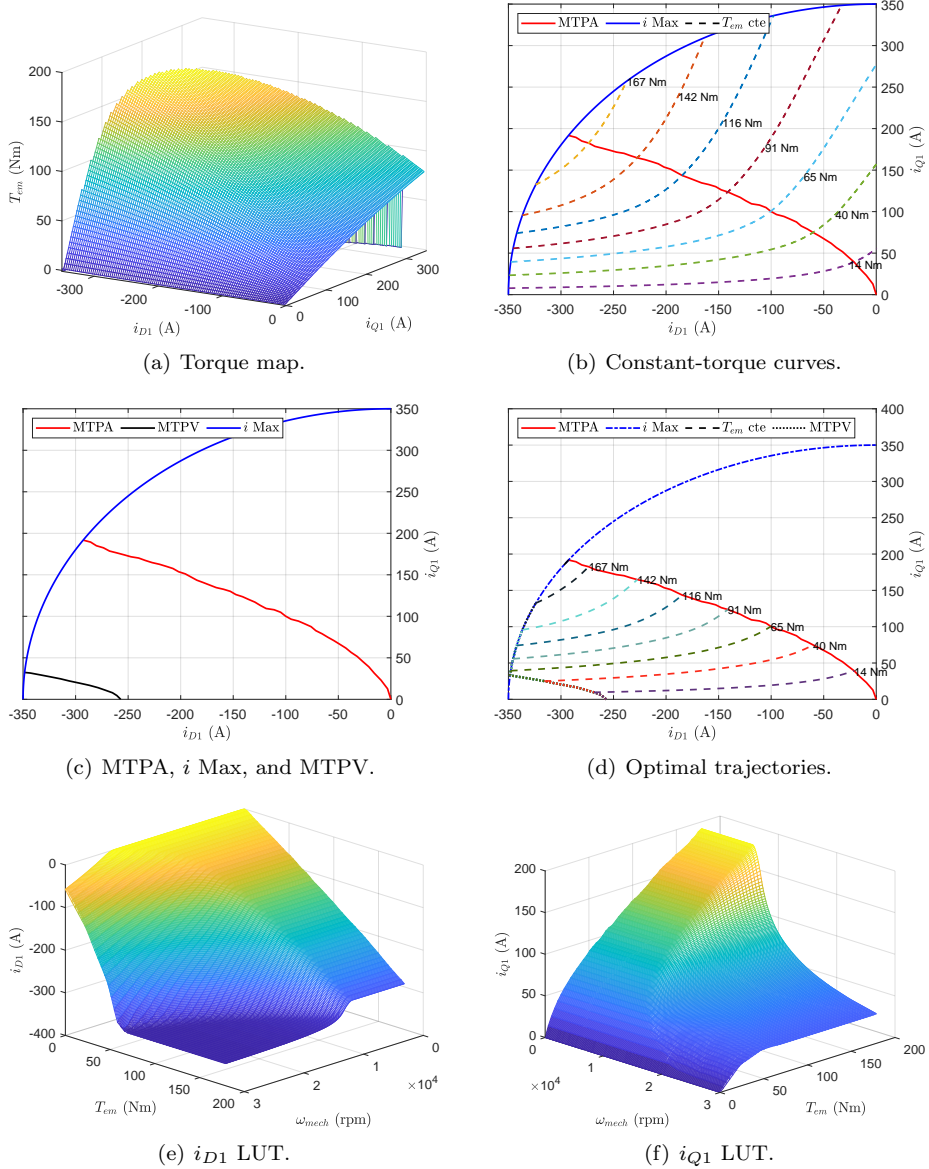

(f) i_{Q1} LUT.

Fig. 3.12: Illustration of the LUT generation process for the IPMSM prototype used in this thesis.

of current with minimum magnitude. Finally, the base speed for each MTPA point is calculated by solving $\sqrt{v_{D1}^2 + v_{Q1}^2} = V_{dcmax}$. Fig. 3.12(b) illustrates some examples of the constant torque, MTPA, and maximum current curves of the IPMSM prototype used in this thesis.

3. For each given electrical speed, the maximum voltage curve is calculated ($\sqrt{v_{D1}^2 + v_{Q1}^2} = V_{dcmax}$). Then, within this curve, the MTPV point is found, i.e., the current vector, which produces maximum torque. Fig. 3.12(c) shows the MTPV curve computed for the IPMSM prototype used in this thesis. Note that, in this case, and for the entire dc voltage range, the MTPV curve is never reached, considering the maximum mechanical speed of the machine.

4. The intersection points between the constant torque curves, the maximum current circle, and the MTPV curve are determined.

5. For each value of T_{em}^*, the curves are delimited to the desired ranges and concatenated to form the optimal current trajectories. Fig. 3.12(d) shows the limited and concatenated trajectories for the different operation regions (MTPA, constant torque, max-current, and MTPV).

6. For each calculated point (current vector) in the constant torque and max-current curves, its associated speed is computed and linked using the maximum voltage curve ($\sqrt{v_{D1}^2 + v_{Q1}^2} = V_{dcmax}$).

7. i_{D1} and i_{Q1} LUTs are sorted, sized, packed and saved. Fig. 3.12(e) and 3.12(f) provide the 3D illustration of the computed LUTs of the IPMSM prototype used in this thesis.

3.2.2 Current regulation

From the modeling approaches described above, two possibilities for current regulation can be derived. The first option ($\mathbf{T_1}$-regulation) is a set of four PI loops for the currents in the $D1 - Q1$ and $D2 - Q2$-axes (transformation $\mathbf{T_1}$). This control approach allows for the regulation of the fundamental components (i_{D1}, i_{Q1}) independent of the regulation of the harmonic components (i_{D2}, i_{Q2}) [124, 125]. Usually, the latter components' set-points are set to zero, as they do not generate mechanical power [124–126].
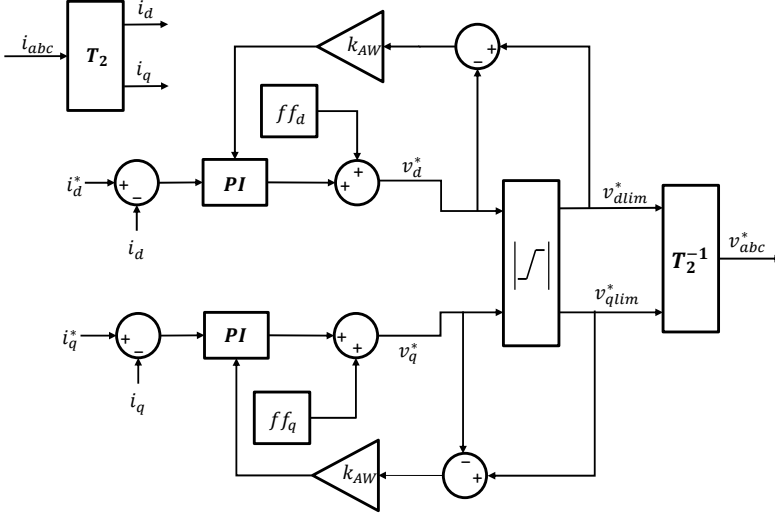
Fig. 3.13: Block diagram of the PI current loops.

The second option ($\mathbf{T_2}$-regulation) is comprised of four PI loops for the $d1 - q1$ and $d2 - q2$ synchronous frames (transformation $\mathbf{T_2}$). In this control approach, the stator currents of the first three-phase set (i_{d1}, i_{q1}) can be independently regulated from the currents of the second three-phase set (i_{d2}, i_{q2}) [64, 126]. As the structure is the same for both current regulation approaches, without loss of generality, Fig. 3.13 illustrates the diagram of the current loops when controlling the currents in the reference axes $d - q$.

In addition to the well-known PI controller, the regulation algorithm incorporates decoupling feed-forward terms. In the scenario of $\mathbf{T_1}$-regulation, the feed-forward terms (3.25) and (3.26) are computed from (3.8) and (3.9).

$$ff_{D1} = R_s i_{D1}^* - \omega_e L_{Q1} i_{Q1}^*, \tag{3.25}$$

$$ff_{Q1} = R_s i_{Q1}^* + \omega_e (L_{D1} i_{D1}^* + \psi_{PM1}). \tag{3.26}$$

For $\mathbf{T_2}$-regulation, the feed-forward terms (3.27) and (3.28) are computed from (3.15) and (3.16).

$$ff_d = R_s i_d^* - \omega_e L_q i_q^* - \omega_e M_q i_q^*, \tag{3.27}$$

$$ff_q = R_s i_q^* + \omega_e L_d i_d^* + \omega_e \psi_{PM} + \omega_e M_d i_d^*. \tag{3.28}$$

In both cases, the current-dependent inductances and fluxes (see Fig. 3.5 and 3.7) are estimated using LUTs to account for magnetic saturation in the feed-forward terms computing. Note that reference currents are used to compute feed-forward terms, as this way, noise from measured currents is not directly transmitted to the control actions v_{dq}.

As the voltage is saturated (see appendix A), an anti-windup loop is implemented to avoid undesired transient behavior such as large overshoot and/or an oscillatory response. Therefore, the proportional (k_p), integral (k_i), and anti-windup (k_{AW}) constants have to be tuned properly [135]. Thanks to the decoupling feed-forward terms, an extended practice is to approximate the stator currents' dynamics to a first-order system [104]:

$$i_{dq}(s) = \frac{1}{L_{dq}s + R_s} v_{dq}(s).$$

(3.29)

Thus, classical techniques (time or frequency domain, pole placement, etc.) for tuning PI regulators can be applied. For example, if time domain tuning is carried out, the PI constants can be computed considering a settling time in the range of $\tau_e \leq t_s \leq 5\tau_e$, and a damping factor of $\zeta < 1$, where $\tau_e = R_s/L$ [136, 137]. Furthermore, during simulations and experimental validation, fine-tuning of the controller's parameters is required.

Finally, the set-point voltages in the synchronous frame ($D - Q$ or $d - q$) are transformed into the natural per-phase variables. Then, during the modulation stage, these voltages are used to calculate the firing signals for the power semiconductors of the six-phase inverter.

3.2.3 Modulation algorithm

In the following, the most extended technique used for PWM modulation of dual three-phase machines is described [138–140]. Fig. 3.14 shows the block diagram of the *double zero-sequence injection* modulation technique [141]. This is an adaptation of the well-known three-phase carrier-based PWM modulation for dual three-phase drives. Herein, the injection of triplen harmonics or zero-sequence signal is incorporated.

For IPMSMs, the maximum speed in the MTPA region is limited by V_{dcmax} [142]. Therefore, the highest possible value of V_{dcmax} without over-modulating is desired for operating the machine in MTPA for a wide speed range. In principle, the maximum output voltage V_{dcmax} of a two-level inverter is $V_{dc}/2$ [31]. However, such voltage limit can be increased up to $V_{dcmax} = V_{dc}/\sqrt{3}$ by per-
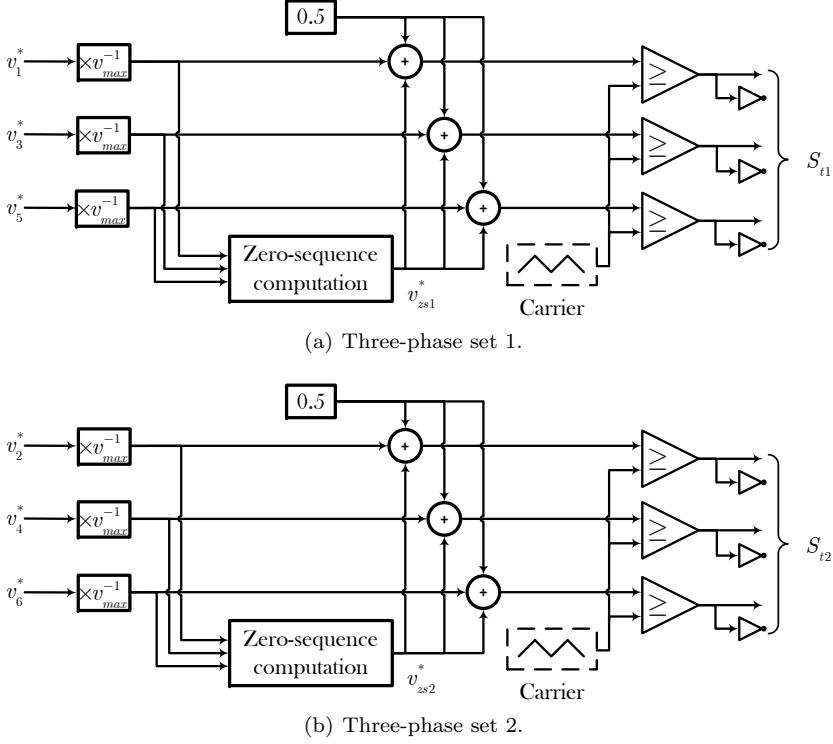
(a) Three-phase set 1.

(b) Three-phase set 2.

Fig. 3.14: Double zero-sequence injection modulation technique.

forming triplen harmonics voltage injection [138,143]. The most commonly used methods for the injection of zero-sequence signals are:

(a) Third harmonic injection [139, 144]. It consists of adding a third-order component in phase with the fundamental harmonic to the output voltage:

$$v_{zs}^* = v_{3pk}^* sin\left(3\omega t\right), \qquad (3.30)$$

where v_{3pk}^* is the amplitude of the third harmonic component. In order to achieve the maximum output voltage of $V_{dc}/\sqrt{3}$, the third harmonics have to be $v_{3pk}^* = v_{1pk}^*/6$, where v_{1pk}^* is the amplitude of the fundamental reference voltage.

The implementation of this method, as described so far, not only requires the amplitude of the reference voltage but also a precise knowledge of the angle. Consequently, this method is impractical for variable speed and closed-loop operation [138]. However, the third harmonic injection can be implemented by adding to the fundamental references the following signal [140]:

$$
\begin{aligned}
v_{zs1}^* &= -\frac{v_1^* v_3^* v_5^*}{v_1^{*2} + v_3^{*2} + v_5^{*2}}, \\
v_{zs2}^* &= -\frac{v_2^* v_4^* v_6^*}{v_2^{*2} + v_4^{*2} + v_6^{*2}},
\end{aligned}
\tag{3.31}
$$

where v_x^* represent the per-phase voltage references without harmonic injection $(x \in \{1, 2, 3, 4, 5, 6\})$. So, the new voltage reference with the third harmonic injection is $\hat{v}_x^* = v_x^* + v_{zs}^*$. This equation is equivalent to (3.30) with a maximum output voltage $(v_{3pk}^* = v_{1pk}^*/6)$, but implementing the third harmonic injection with (3.31) only requires the instantaneous values of the fundamental voltage references.

(b) The second method is the one named min-max, which only requires the knowledge of the actual fundamental reference voltages to increase the voltage limit up to $V_{dc}/\sqrt{3}$. This zero sequence is calculated as follows [138, 140]:

$$
\begin{aligned}
v_{zs1}^* &= \frac{min\,\{v_1^*, v_3^*, v_5^*\} + max\,\{v_1^*, v_3^*, v_5^*\}}{2}, \\
v_{zs2}^* &= \frac{min\,\{v_2^*, v_4^*, v_6^*\} + max\,\{v_2^*, v_4^*, v_6^*\}}{2}.
\end{aligned}
\tag{3.32}
$$

The min-max signal is composed of odd triple harmonics. Furthermore, the min-max sequence injection produces precisely the same pulse pattern as the one achieved by a center-weighted Space Vector Modulation (SVM) [138]. Therefore, the carrier-based PWM with min-max signal injection has the advantages offered by SVM but with a much simpler implementation. This is why it has been chosen for its implementation in the controller of the dual three-phase IPMSM.

As is described in this section, the implementation of harmonics injection is relatively straightforward for a FOC type controller. However, this is not true for non-linear regulation approaches such as first-order Sliding Mode Control
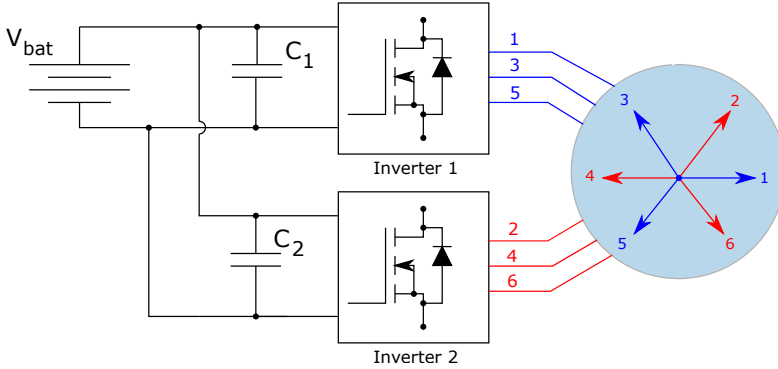
Fig. 3.15: Standard configuration of dual three-phase drive with parallel dc-links connected.

(SMC). In appendix B it is proposed how to incorporate harmonics injection capabilities in such type of controller.

3.3 Vector torque control alternatives for dual three-phase IPMSMs

This section describes three torque control strategies for standard dual-three phase drives (Fig. 3.15), i.e., configurations with parallel connected dc-links, considering the vector model approaches previously presented. The first strategy, called *double three-phase torque control*, consists of the implementation of two independent torque control loops, one for each three-phase set. This strategy is based on the $\mathbf{T_2}$ transformation. The second strategy, called *multiphase torque control*, leverages the $\mathbf{T_1}$ transformation to control the torque through the regulation of currents in the $D1 - Q1$ plane while regulating the current components in the $D2 - Q2$ plane to zero. The third strategy, the *Hybrid torque control*, is a novel proposal of this thesis. To the best author's knowledge, no other work deals with this particular dual three-phase control approximation. It is based on both $\mathbf{T_1}$ and $\mathbf{T_2}$ transformations, aiming to combine their advantages. In the next chapter, the application of these control algorithms to a particular dual three-phase drive configuration is analyzed.

3.3.1 *Double three-phase* torque control

A straightforward solution for torque control of dual three-phase machines is to implement an independent control loop for each three-phase set. Therefore, the well-known and widely validated control strategies for three-phase IPMSMs can be immediately applied [64, 126, 128]. Fig. 3.16 shows the block diagram of the *double three-phase* torque controller, where each three-phase set is required to generate half of the desired torque.

In this solution, each three-phase set is treated as an independent machine. For each set, the torque controller has the three components described in the previous section. First, the current set-point generation is responsible for providing the optimal current set-points considering the required torque, mechanical speed, dc-link, and stator voltage of each three-phase set. Therefore, the VCT loop is implemented to regulate the stator voltages $v_{sj} = \sqrt{v_{dj}^{*\,2} + v_{qj}^{*\,2}}$ for each three-phase set. In the same way, the 2D-LUTs for each $d-q$ plane (transformation $\mathbf{T_2}$) are computed offline.

The second and third components of the *double three-phase* controller are the $\mathbf{T_2}$-regulation loops and the modulation algorithm [126]. These current control loops include PI controllers, decoupling feed-forward terms, and an anti-windup scheme, as described in the previous section. Then, the voltage references are transformed from the $d-q$ synchronous frames into the respective per-phase values. Finally, PWM blocks synthesize the firing pulses for the inverter. To do so, the *double zero-sequence injection* technique, as described previously, is implemented.

The *double three-phase* torque control has two main advantages. The first one is the straightforward application of well-known control techniques used for decades for the control of three-phase machines. The second one is the independent control of each three-phase set. However, as demonstrated in [127, 128], this approach does not consider the cross-coupling effects between winding sets, which has a direct influence on the electromagnetic torque production of the machine. As a consequence, significant deviations from the commanded torque can be produced.
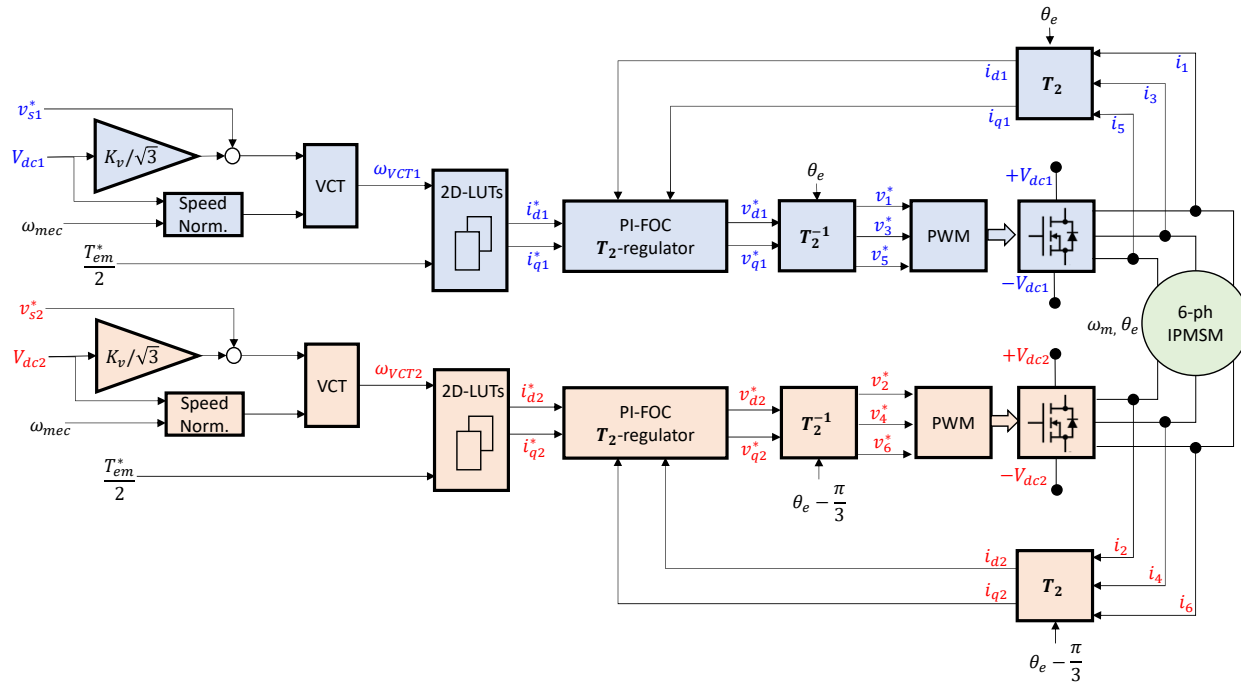
Fig. 3.16: Block diagram of the *double three-phase* torque control approach, including independent set-point generators.

3.3.2 *Multiphase* torque control

In contrast to the previous control scheme, this solution applies techniques from the more recent field of multiphase electric machines [29,30,145] to the control of dual-three phase drives. Fig. 3.17 illustrates the block diagram of the *multiphase* torque controller. This solution takes advantage of transformation $\mathbf{T_1}$. Thus, the dual-three phase is considered as a single unit responsible for producing the full required torque [124–126].

The *multiphase* torque controller follows the general vector torque control approach described in the previous section: (1) current set point generation, (2) current regulation, and (3) modulation. The structure of the current set-point generation algorithm is quite similar to the previous one. However, in this case, the current generation is done in the $D1 - Q1$ synchronous frame. Therefore, the machine is considered as a unit, where, as stated before, both sets interact to produce the required torque. For the calculation of the required 2-D LUTs, the model represented by (3.8), (3.9), and (3.10) has to be considered. Then, the optimum current LUTs are calculated from the flux data computed through the IPMSM FEM model. As the currents $i_{D1} - i_{Q1}$ are responsible for producing torque, only two LUTs are required instead of four.

As in the previous approach, the VCT scheme of Fig. 3.10 is implemented to provide additional robustness against parameter uncertainties. However, in this case, the reference stator voltage ($v_S = \sqrt{v_{D1}^*{}^2 + v_{Q1}^*{}^2}$) and the mean dc-link input voltages (V_{dc1}, V_{dc2}) are considered to feed the VCT loop. Another difference between the *multiphase* over the *double three-phase* torque control is that the LUTs are fed with the total required torque instead of half the torque.

Then, the stator currents are controlled using the $\mathbf{T_1}$-regulation loops described in section 3.2.2. The $i_{D1} - i_{Q1}$ currents are regulated to the set-points provided by the LUTs, while $i_{D2} - i_{Q2}$ are regulated to zero. The latter allows reducing the power consumed for non-torque producing harmonics [124–126].

Finally, the voltage set-points are transformed from the $D - Q$ synchronous frames into the per-phase values. Then, the *double zero-sequence injection* PWM technique synthesizes the firing pulses for the power converter.

Summarizing, the main advantage of the *multiphase* approach is the addressing of the coupling effects between sets while taking advantage of a simpler model than in the double three-phase approach [125, 126]. Therefore, precise torque set-point tracking is expected.
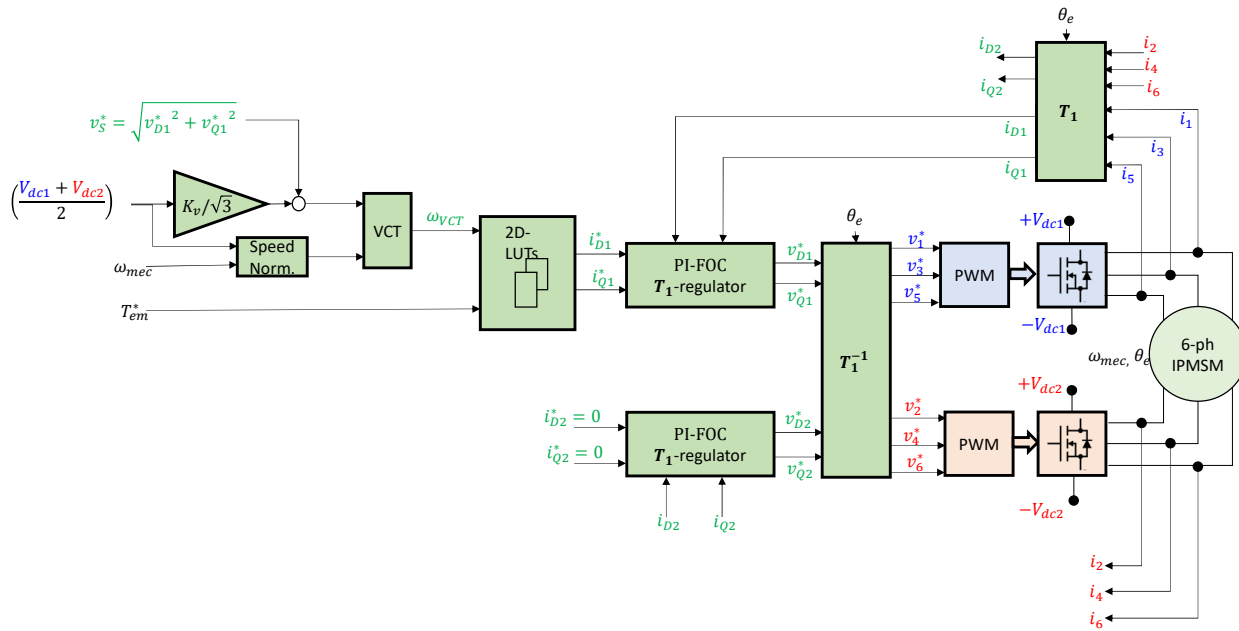
Fig. 3.17: Block diagram of the *multiphase* torque control approach.

Furthermore, the *multiphase* approach allows the independent regulation of the fundamental components (i_{D1}, i_{Q1}) with respect to the harmonic components (i_{D2}, i_{Q2}) [124–126]. However, the independent control of each three-phase set is not straightforward, complicating the utilization of some additional control degrees of freedom.

3.3.3 Proposed *Hybrid* torque control

Fig. 3.18 shows the block diagram of the proposed *hybrid* torque control strategy. This approach aims to keep the advantages of the *double three-phase* and *multiphase* torque control while avoiding their drawbacks. This novel vector torque controller for dual three-phase drives combines the *multiphase* current set-point generation with the *double three-phase* current regulators. Therefore, this solution allows the independent current control of each three-phase set, while the generation of optimal current set-points considers coupling between three-phase sets and reduces the number of LUTs required.

As in the *multiphase* approach, the current generation is done in the $D1-Q1$ synchronous frame (VCT and LUTs). However, in this case, the average of the reference stator voltages (v_{s1}, v_{s2}) and dc-link input voltages (V_{dc1}, V_{dc2}) are considered to feed the VCT loop.

Once the optimal fundamental components set-points $i_{D1}^* - i_{Q1}^*$ are calculated, and the harmonic components' references are set to zero $(i_{D2}^* = i_{Q2}^* = 0)$, they are transformed into the $d_1 - q_1$ and $d_2 - q_2$ planes. This is done thanks to the transformation $\mathbf{T_{1 \to 2}}$:

$$
\begin{bmatrix} d_1 \\ q_1 \\ h_1 \\ d_2 \\ q_2 \\ h_2 \end{bmatrix} = \begin{bmatrix} 1 & 0 & cos(6\theta_e) & -sin(4\theta_e) & 0 & 0 \\ 0 & 1 & -sin(6\theta_e) & cos(4\theta_e) & 0 & 0 \\ 0 & 0 & 0 & 0 & 1 & 0 \\ 1 & 0 & -cos(6\theta_e) & sin(6\theta_e) & 0 & 0 \\ 0 & 1 & sin(6\theta_e) & cos(6\theta_e) & 0 & 0 \\ 0 & 0 & 0 & 0 & 0 & 1 \end{bmatrix} \begin{bmatrix} D_1 \\ Q_1 \\ D_2 \\ Q_2 \\ H_1 \\ H_2 \end{bmatrix}. \tag{3.33}
$$

As can be seen from (3.33), if D_2 and Q_2 are null, then the components $d_1 = d_2 = D_1$ and $q_1 = q_2 = Q_1$.

Matrix $\mathbf{T_{1 \to 2}}$ can be derived by applying the inverse transformation $\mathbf{T_1^{-1}}$ to the $D - Q$ components $(\mathbf{I} = \mathbf{T_1^{-1} I_{DQ}})$. Then, the $\mathbf{T_2}$ transformation can be applied as $\mathbf{I_{dq}} = \mathbf{T_2 I}$. I.e., $\mathbf{T_{1 \to 2}} = \mathbf{T_2 T_1^{-1}} = \mathbf{P_2 C_2 C_1^{-1} P_1^{-1}}$.
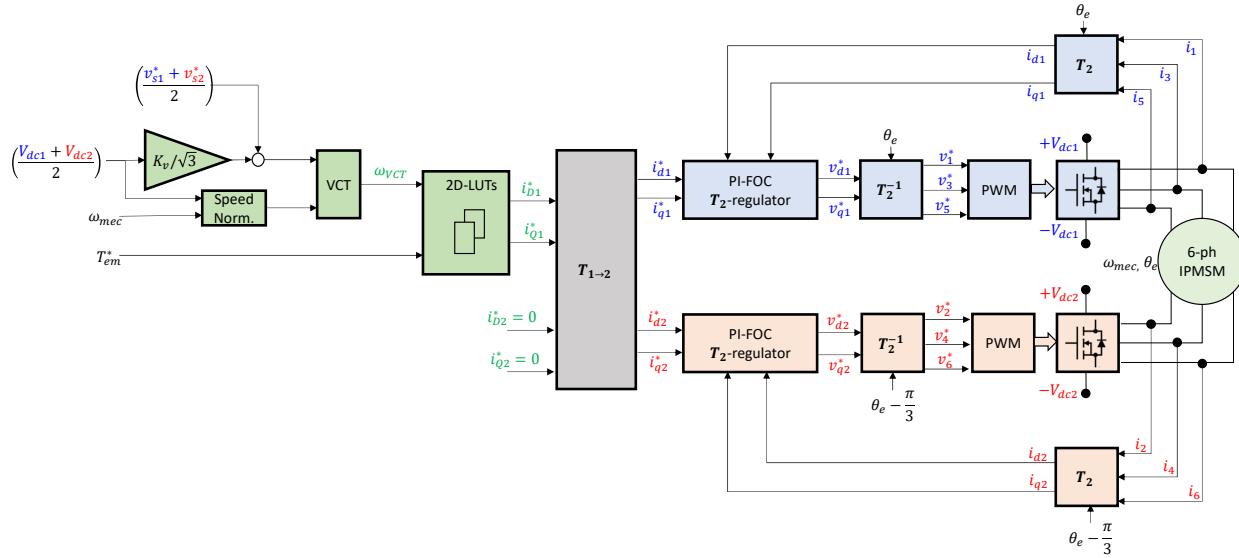
Fig. 3.18: Block diagram of the *hybrid* torque control approach.

Note that $\mathbf{C_2}$ in (3.12) considers a different order for phase components than $\mathbf{C_1}$:

$$\begin{bmatrix} \alpha_1 \\ \beta_1 \\ h_1 \\ \alpha_2 \\ \beta_2 \\ h_2 \end{bmatrix} = \mathbf{C_2} \begin{bmatrix} 1 \\ 3 \\ 5 \\ 2 \\ 4 \\ 6 \end{bmatrix}. \tag{3.34}$$

For that reason, matrix $\mathbf{C_2}$ is reorganized as follows:

$$\begin{bmatrix} \alpha_1 \\ \beta_1 \\ h_1 \\ \alpha_2 \\ \beta_2 \\ h_2 \end{bmatrix} = \hat{\mathbf{C}}_2 \begin{bmatrix} 1 \\ 2 \\ 3 \\ 4 \\ 5 \\ 6 \end{bmatrix}, \tag{3.35}$$

$$\hat{\mathbf{C}}_2 = \frac{2}{3} \begin{bmatrix} 1 & 0 & cos(2\alpha) & 0 & cos(4\alpha) & 0 \\ 0 & 0 & sin(2\alpha) & 0 & sin(4\alpha) & 0 \\ 0.5 & 0 & 0.5 & 0 & 0.5 & 0 \\ 0 & 1 & 0 & cos(2\alpha) & 0 & cos(4\alpha) \\ 0 & 0 & 0 & sin(2\alpha) & 0 & sin(4\alpha) \\ 0 & 0.5 & 0 & 0.5 & 0 & 0.5 \end{bmatrix}. \tag{3.36}$$

Considering that $\mathbf{C_1^{-1}} = 3\mathbf{C_1^T}$ [see (3.5)], the product $\hat{\mathbf{C}}_2 \mathbf{C_1^{-1}}$ is:

$$\hat{\mathbf{C}}_2 \mathbf{C_1^{-1}} = \begin{bmatrix} 1 & 0 & 1 & 0 & 0 & 0 \\ 0 & 1 & 0 & -1 & 0 & 0 \\ 0 & 0 & 0 & 0 & 1 & 0 \\ \frac{1}{2} & \frac{\sqrt{3}}{2} & -\frac{1}{2} & \frac{\sqrt{3}}{2} & 0 & 0 \\ -\frac{\sqrt{3}}{2} & \frac{1}{2} & \frac{\sqrt{3}}{2} & \frac{1}{2} & 0 & 0 \\ 0 & 0 & 0 & 0 & 0 & 1 \end{bmatrix}. \tag{3.37}$$

Next, the product $\hat{\mathbf{C}}_2 \mathbf{C_1^{-1}} \mathbf{P_1^{-1}}$ is computed, [see (3.6)]:

106

$$\hat{\mathbf{C}}_2\mathbf{C}_1^{-1}\mathbf{P}_1^{-1} =$$

$$\begin{bmatrix} cos(\theta_e) & -sin(\theta_e) & cos(5\theta_e) & -sin(5\theta_e) & 0 & 0 \\ sin(\theta_e) & cos(\theta_e) & -sin(5\theta_e) & cos(5\theta_e) & 0 & 0 \\ 0 & 0 & 0 & 0 & 1 & 0 \\ cos(\theta_e - \frac{\pi}{3}) & -sin(\theta_e - \frac{\pi}{3}) & -cos(5\theta_e + \frac{\pi}{3}) & sin(5\theta_e + \frac{\pi}{3}) & 0 & 0 \\ sin(\theta_e - \frac{\pi}{3}) & cos(\theta_e - \frac{\pi}{3}) & sin(5\theta_e + \frac{\pi}{3}) & cos(5\theta_e + \frac{\pi}{3}) & 0 & 0 \\ 0 & 0 & 0 & 0 & 0 & 1 \end{bmatrix}. \quad (3.38)$$

The last step consist on multiplying $\mathbf{P_2}$ from (3.6) by (3.38), then:

$$\mathbf{T_{1\to 2}} = \mathbf{T_2}\mathbf{T_1^{-1}} \;=\; \mathbf{P_2}\mathbf{C_2}\mathbf{C_1^{-1}}\mathbf{P_1^{-1}} \;=\; \begin{bmatrix} 1 & 0 & A_{11} & A_{12} & 0 & 0 \\ 0 & 1 & A_{21} & A_{22} & 0 & 0 \\ 0 & 0 & 0 & 0 & 1 & 0 \\ 1 & 0 & B_{11} & B_{12} & 0 & 0 \\ 0 & 1 & B_{21} & B_{22} & 0 & 0 \\ 0 & 0 & 0 & 0 & 0 & 1 \end{bmatrix}. \quad (3.39)$$

Applying some trigonometric simplifications, the final result (3.33) is obtained:

$$\begin{aligned} A_{11} &= cos(\theta_e)cos(5\theta_e) - sin(\theta_e)sin(5\theta_e) = cos(6\theta_e), \\ A_{12} &= -cos(\theta_e)sin(5\theta_e) + sin(\theta_e)cos(5\theta_e) = -sin(4\theta_e), \\ A_{21} &= -sin(\theta_e)cos(5\theta_e) - cos(\theta_e)sin(5\theta_e) = -sin(6\theta_e), \\ A_{22} &= sin(\theta_e)sin(5\theta_e) + cos(\theta_e)cos(5\theta_e) = cos(4\theta_e), \end{aligned} \quad (3.40)$$

$$\begin{aligned} B_{11} &= -cos(\theta_e - \frac{\pi}{3})cos(5\theta_e + \frac{\pi}{3}) + sin(\theta_e - \frac{\pi}{3})sin(5\theta_e + \frac{\pi}{3}) = -cos(6\theta_e), \\ B_{12} &= cos(\theta_e - \frac{\pi}{3})sin(5\theta_e + \frac{\pi}{3}) + sin(\theta_e - \frac{\pi}{3})cos(5\theta_e + \frac{\pi}{3}) = sin(6\theta_e), \\ B_{21} &= sin(\theta_e - \frac{\pi}{3})\,cos(5\theta_e + \frac{\pi}{3}) + cos(\theta_e - \frac{\pi}{3})\,sin(5\theta_e + \frac{\pi}{3}) = sin(6\theta_e), \\ B_{22} &= -sin(\theta_e - \frac{\pi}{3})\,sin(5\theta_e + \frac{\pi}{3}) + cos(\theta_e - \frac{\pi}{3})\,cos(5\theta_e + \frac{\pi}{3}) = cos(6\theta_e). \end{aligned}$$
$$(3.41)$$

Finally, as in the *double three-phase* control approach, $\mathbf{T_2}$-regulation loops track the current set-points, and the *double zero-sequence injection* PWM algorithm synthesizes the firing pulses for the power converter.

3.4 Conclusions

Three mathematical modeling approaches for representing dual three-phase machines were presented. First, the model in natural per-phase variables was described. This model proved to be complex and highly coupled, therefore not suitable for the design of control systems. Then, two models in synchronous reference frames were reported. The *multiphase* vector model decoupled and decomposed the per-phase variables according to their harmonics components. Thus, the optimal current references are easier to calculate, while the cross-coupling between the three-phase sets is considered. Finally, the *double three-phase* vector model facilitates the independent regulation of the power consumed (or delivered during regenerative braking) by each three-phase set. However, the two planes related to each three-phase set remain coupled.

In order to facilitate the understanding of the components required for a vector torque control for dual three-phase IPMSMs, a generic block diagram of a controller was presented. This diagram introduces the components, their interactions, and their functionalities. Three main components were described: the current set-point generator, the current regulator, and the modulator. For the current set-point generator, a combination of precalculated LUTs, VCT feedback, and speed normalization was selected. This approach reduces the required dimensions of the LUTs to two, while the VCT provides additional robustness under parameter variations or uncertainties.

A programmatic algorithm for the offline calculation of the 2D-LUTs was presented. The algorithm is quite flexible and allows the calculation of LUTs both for three-phase and multiphase machines. Then, this algorithm was used to calculate the 2D-LUTs for the dual three-phase IPMSM prototype used in this thesis. In the next chapter, such 2D-LUTs are validated by simulations, laboratory, and in-vehicle tests.

For the current regulation, two possible PI-FOC solutions were analyzed, each based on one of the two vector models. A detailed block diagram was presented, including PI controllers, decoupling feed-forward terms, and an anti-windup scheme. Furthermore, a general tuning procedure was briefly described.

For modulation, the *double zero-sequence injection* PWM technique was selected. The selected algorithm includes the min-max zero sequence. This carrier-based PWM with min-max signal injection has the advantages offered by SVM but with a much simpler implementation. The incorporation of this feature is of capital importance in automotive drives, where the MTPA region should be extended by maximizing the utilization of the available dc-link voltage.

Finally, three particular strategies for torque vector control of dual three-phase IPMSMs were analyzed. The *double three-phase* torque controller allows the straightforward application of well-known control techniques of three-phase machines and the independent control of each three-phase set. However, this approach does not consider the cross-coupling effects between winding sets. Thus, significant deviations from the commanded torque can be produced.

The *multiphase* torque controller considers the inherent cross-coupling between the two three-phase sets. Therefore, precise torque tracking is expected. Furthermore, the *multiphase* approach allows for the regulation of the fundamental components independent of the regulation of the harmonic components. However, the independent control of each three-phase set is not straightforward.

The proposed *hybrid* torque controller combines the *multiphase* current setpoint generation with the *double three-phase* current regulators in order to keep the advantages of both controllers while avoiding their drawbacks. For the combination of *multiphase* and *double three-phase* was required the transformation $\mathbf{T_{1 \rightarrow 2}}$, which mathematical derivation was detailed. In the next chapter, the application of this proposal for the torque control of a dual-three phase with a particular cascaded dc-link configuration is assessed. In that chapter, simulations, laboratory, and in-vehicle validations of the proposed hybrid torque regulation approach are presented.

The proposed vector control technique is convenient for operating the drive during normal conditions. However, if fault-tolerant approaches need to be implemented in the presence of a fault, current regulators with high dynamics, such as first-order SMC controllers, should substitute the PI regulation blocks. In this context and considering future lines of investigation, an SMC regulation scheme to regulate each three-phase set is presented in appendix B. This approach incorporates harmonic injection capabilities, which represent a novelty over previously reported SMC approaches for PMSM drives.

Chapter 4

Torque control of automotive dual three-phase IPMSM with a cascaded dc-link

As contextualized in chapter 1, the control solutions proposed in this thesis have been investigated within the European Union-funded FITGEN project. This project aimed to develop a functionally integrated e-axle ready to be implemented in third-generation EVs [146]. In particular, the following performance indicators were defined: to increase the power density of the electric machine and the inverter by 40 % and 50 %, respectively, to provide an affordable super-fast charging capability, and to increase 40 % the EV driving range. To achieve these targets, the e-axle incorporates a symmetrical six-phase IPMSM driven by a full-SiC inverter with a switching frequency of up to 24 kHz. This e-axle also includes a dc/dc converter mounted between the battery pack and power inverter (Fig. 4.1). This converter boosts the dc-link to the 800 V range, providing embedded super-fast charging capabilities. However, a cascaded dc-link configuration has been adopted to avoid the utilization of power semiconductors with high voltage ratings, which exhibit higher conduction losses and cost. This configuration consists of two three-phase inverter units connected in series, where each unit drives one of the machine winding sets (Fig. 4.1).
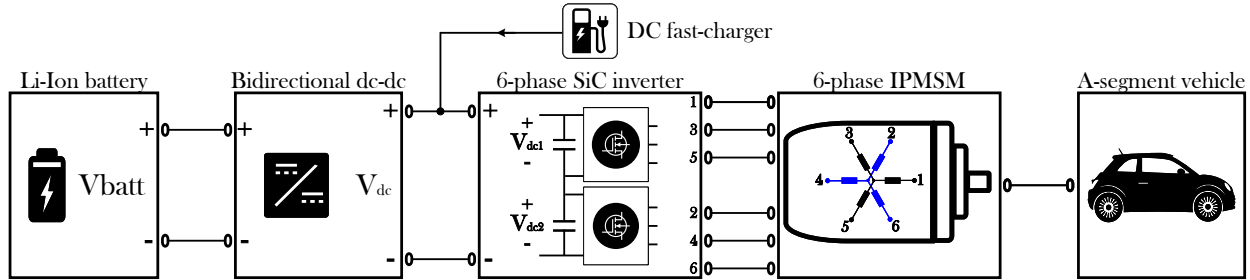
Fig. 4.1: General diagram of the FITGEN e-axle including a dc/dc converter, a six-phase SiC-based inverter with a cascaded dc-link capacitor, and a dual three-phase IPMSM.

Considering all the previous, the electric machine control system must deal with the following aspects:

1. *Optimum operation*: The controller must determine the current references of a minimum magnitude according to the commanded torque and the machine's rotational speed, i.e., both MTPA and FW operation must be considered.

2. *Current regulation*: A control algorithm is needed to regulate the stator currents and generate the voltage set-points for the PWM modulator.

3. *Active dc-link voltage balancing*: Due to the incorporation of the cascaded dc-link configuration, an algorithm must be included to keep the input voltage of each three-phase converter unit balanced.

4. *Modulation*: The particular configuration of the stator winding makes necessary the incorporation of an interleaved PWM modulation pattern.

The first two aspects have already been addressed in chapter 3. Regarding the active dc-link voltage balancing, this kind of cascaded configuration and their corresponding voltage balancing controllers have been previously proposed in the literature for various applications, such as for wind turbines based on asymmetrical six-phase induction machines [78], twelve-phase induction machines [79], twelve-phase surface mounted permanent magnet synchronous generators [76], and nine three-phase decoupled-segment generators [74]. However, these applications only consider the generative operation mode, where the dc-voltage of each inverter unit is asymptotically stable, even in open-loop.

On the other hand, in [81] and [83], a cascaded configuration is theoretically proposed for EV powertrains. Therefore, motoring operation is considered. In this scenario, a closed-loop balancing algorithm is required due to the unstable behavior of the dc-link voltages during traction operation. In [81] and [83], the design and validation of the balancing algorithm are done for passive three-phase loads or down-scaled laboratory induction machines/converters at TRL-3/4.

In light of the foregoing, the objective of this chapter is to propose and validate, at TRL7, a torque control system for a full-scale symmetrical dual three-phase IPMSM with a cascaded dc-link configuration. For this purpose, a novel dc-link balancing algorithm for cascaded inverter configurations is designed, but first, a mathematical model of the cascaded dc-link is introduced. Such a model aims to support the design of the voltage balancing control strategy. Then, based on the controllers presented in chapter 3, torque regulation

alternatives are compared for the dual three-phase drive with cascaded configuration. These alternatives incorporate the proposed dc-link voltage algorithm. Their performance is evaluated using software simulation.

According to simulation results, the most promising alternative is selected for experimental validation, and particular requirements of the drive regarding modulation are discussed. Experimental verification is initially carried out at TRL-6 using a full-scale prototype of the dual three-phase drive. Besides allowing the fine-tuning of the control parameters, such initial tests facilitate the design and implementation of an interleaved PWM scheme to cancel the high current ripple caused by the machine winding distribution. Furthermore, during this laboratory experimentation, the electric drive is validated extensively under four driving cycles. Finally, the novel control proposal is validated at TRL-7, as the dual three-phase prototype is incorporated in an A-segment vehicle. All these experimental results demonstrate the proposal's applicability in an industrial environment.

4.1 Dual three-phase IPMSM drive with cascaded dc-link configuration

4.1.1 General description of the cascaded configuration

In general, the two three-phase sets of a dual three-phase PMSM are fed by two independent voltage source inverters (VSI), which dc-link capacitors are connected in parallel to a battery pack [Fig. 4.2(a)]. Alternatively, various works propose the incorporation of an intermediate high voltage dc/dc converter [Fig. 4.2(b)] between the power electronics and the battery pack [143, 147–150]. In principle, incorporating the dc/dc converter can increase conduction and switching losses and also cost. However, the following advantages can be obtained:

- The dc-link can be boosted to provide embedded super-fast charging capabilities. For example, and as stated in the introduction of this chapter, within the FITGEN project, this voltage is boosted from 320 V up to 800 V [149, 150].

- The battery and inverter input voltages are decoupled. From a design point of view, this allows reducing the size of the electric machine and optimizing the battery system [147, 151, 152].

114

(a) Conventional configuration.

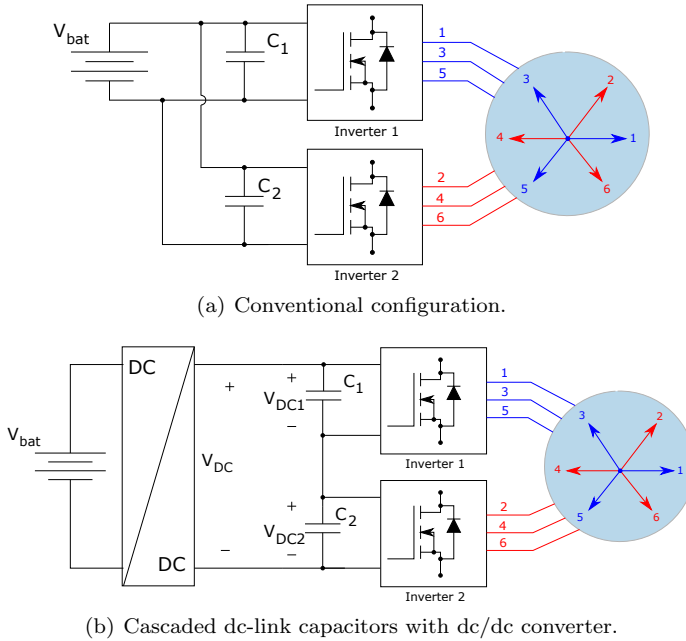(b) Cascaded dc-link capacitors with dc/dc converter.

Fig. 4.2: General diagram of a dual three-phase IPMSM drive architecture.

- The dc-link capacitor's power and energy ratings can be reduced [151].

- The dc-link voltage can be adapted in real-time through a dedicated control strategy, and overall system power losses (in converters and electric machine) can be minimized [147–153].

- A lower current ripple and a higher power factor can be obtained [147, 148, 153].

- Inverter input dc-link voltage can be maintained regardless of the state-of-charge (SoC) of the battery pack [150].

Considering the aforementioned advantages, within project FITGEN, a dc/dc converter, including a cascaded dc-link configuration, was selected to achieve the project's key performance indicators.
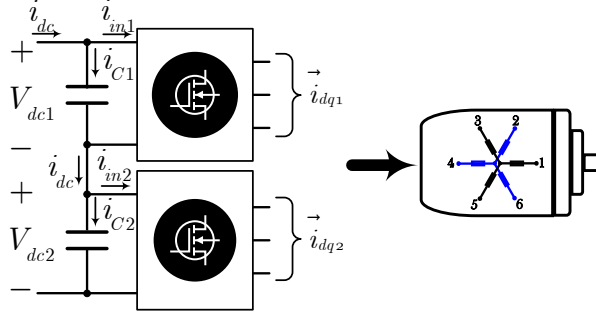
Fig. 4.3: Simplified diagram of the cascaded dc-link configuration.

4.1.2 Mathematical representation of the cascaded dc-link

In chapter 3, three mathematical modeling approaches for dual three-phase IPMSMs were provided. However, the incorporation of the cascaded dc-link configuration was not considered. To fill this gap, this section presents a mathematical representation of the cascaded dc-link to support the design of the proposed voltage balancing control strategy.

As will be explained in section 4.2, the balancing algorithm utilizes the q-axis currents to balance the dc-link voltages. Therefore, the mathematical description of how the voltages behave when the q-axis currents change is provided below. Fig. 4.3 shows a simplified circuit diagram of the cascaded configuration, where i_{dc} is the current circulating from/to the dc/dc converter, V_{dcj} is the voltage of capacitor C_j, $i_{in,j}$ is the current circulating through inverter unit j, and i_{Cj} is the current flowing through capacitor C_j ($j \in \{1,2\}$). Using Kirchhoff's circuit laws, it can be derived that the voltage on each dc-link capacitor is:

$$V_{dcj} = \frac{1}{C_j} \int (i_{dc} - i_{inj})dt. \tag{4.1}$$

In order to analytically determine the relationship between the dc-link voltages and the electric machine input currents, as a first step, the expression of the average input currents of both inverters can be considered [154, 155]:

$$avg(i_{inj}) = \frac{3}{4}|\vec{i}_{dqj}|m_j cos\phi_j, \tag{4.2}$$

where $|\vec{i}_{dqj}|$ is the current vector magnitude of the j-th three-phase set, represented in the $d - q$ reference frame, m_j is the modulation index and $cos\phi_j$ is

the power factor. Therefore, by combining (4.1) and (4.2), it is possible to determine the voltage variation in V_{dcj} due to a change in the current magnitude $|\vec{i}_{dqj}|$:

$$\Delta V_{dcj} = -\int B_j \Delta |\vec{i}_{dqj}| dt, \tag{4.3}$$

where $B_j = 3m_j cos\phi_j/4C_j$.

If the variations in the current vector magnitude $(\Delta|\vec{i}_{dqj}|)$ are produced due to changes in the current component i_{qj}, then:

$$\Delta|\vec{i}_{dqj}| = \sqrt{i_{dj}^2 + (i_{qj} + \Delta i_{qj})^2} - \sqrt{i_{dj}^2 + i_{qj}^2}. \tag{4.4}$$

Multiplying and dividing (4.4) by the term χ:

$$\chi = \sqrt{i_{dj}^2 + (i_{qj} + \Delta i_{qj})^2} + \sqrt{i_{dj}^2 + i_{qj}^2}, \tag{4.5}$$

the following approximation holds true as long as $|\Delta i_{qj}| \ll |\vec{i}_{dqj}|$:

$$\Delta|\vec{i}_{dqj}| \approx \frac{i_{qj}}{|\vec{i}_{dqj}|}\Delta i_{qj}. \tag{4.6}$$

Substituting (4.6) into (4.3), the resulting expression shows that a change in the q-axis current (Δi_{qj}) will generate the following variation in V_{dcj}:

$$\Delta V_{dcj} \approx -\int B_j \frac{i_{qj}}{|\vec{i}_{dqj}|}\Delta i_{qj} dt. \tag{4.7}$$

From (4.1) to (4.7), the following considerations about the dynamic behavior of the cascaded capacitors can be drawn (identical three-phase windings and inverter units are considered):

- During steady state operation and considering that the system is initially balanced, $i_{in1} = i_{in2}$, $B_1 = B_2$, and $V_{dc1} = V_{dc2} = V_{dc}/2$ at $t = 0$ s. However, as pointed out in [78, 81], unless a voltage balancing strategy is included, even a slight unbalance in the system will cause dc-link voltages to diverge.

- V_{dc} is imposed by the dc/dc converter. As $V_{dc1} + V_{dc2} = V_{dc}$, then $\Delta V_{dc1} = -\Delta V_{dc2}$.

(a) $B_j i_{qj}/|\vec{i}_{dqj}|$ vs T_{em}.

(b) $B_j i_{qj}/|\vec{i}_{dqj}|$ vs ω_{mec}.
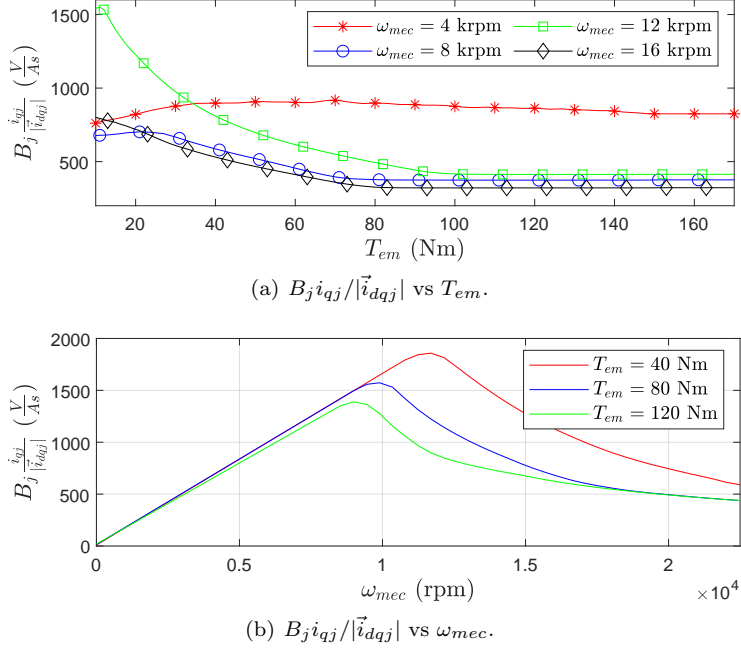
Fig. 4.4: $B_j i_{qj}/|\vec{i}_{dqj}|$ as function of the operating point.

- In motoring mode, an increase in the q-axis current's magnitude will cause a decrease in the associated dc-link voltage ($|i_{qj} + \Delta i_{qj}| > |i_{qj}|$, then $\Delta V_{dcj} < 0$).

- In contrast, in regenerative mode, if $|i_{qj} + \Delta i_{qj}| > |i_{qj}|$, then $\Delta V_{dcj} > 0$.

- Fig. 4.4 shows the variation of $B_j i_{qj}/|\vec{i}_{dqj}|$ with respect to the machine operating point. The data in this figure is retrieved through FEM data of the prototype used during the experimental verification of the proposal. From Fig. 4.4 and (4.7), the non-linear relationship between the q-axis current and dc-link voltage becomes clear.

- After an initial balancing, a dc-voltage unbalance is solely generated by an unbalanced current consumption of the three-phase inverter/machine

units. To demonstrate this, the following mathematical analysis is carried out.

First, the expression of the capacitor's voltage is considered for each set:

$$V_{dc1} = \int \frac{i_{C1}}{C_1} dt \ + \ V_{dc1}(0), \tag{4.8}$$

$$V_{dc2} = \int \frac{i_{C2}}{C_2} dt \ + \ V_{dc2}(0), \tag{4.9}$$

$$V_{dc} = V_{dc1} + V_{dc2} = \int \left(\frac{i_{C1}}{C_1} + \frac{i_{C2}}{C_2} \right) dt + \ V_{dc1}(0) + \ V_{dc2}(0), \tag{4.10}$$

where $V_{dc1}(0)$ and $V_{dc2}(0)$ are the initial conditions. Assuming that the voltage balancing algorithm successfully balanced the dc-links voltages when initializing the power system, then $V_{dc1}(0) = V_{dc2}(0) = \ V_{dc}/2$ (V_{dc} is imposed by the dc/dc converter). Thus, the integrand of the right side of (4.10) is equal to zero. Therefore:

$$\frac{i_{C1}}{C_1} = -\frac{i_{C2}}{C_2}. \tag{4.11}$$

From Fig. 4.3 and applying Kirchhoff's circuit laws, $i_{C2} = i_{C1} + i_{in1} - i_{in2}$. Replacing the previous expression into (4.11), the following is obtained:

$$\frac{i_{C1}}{C_1} = -\frac{i_{C1} + i_{in1} - i_{in2}}{C_2}. \tag{4.12}$$

By isolating i_{C1} in (4.12), the following is obtained:

$$\frac{i_{C1}}{C_1} = \frac{i_{in2} - i_{in1}}{C_1 + C_2}. \tag{4.13}$$

Therefore, once the dc-link voltages are initially balanced:

$$V_{dc1} = \int \frac{i_{in2} - i_{in1}}{C_1 + C_2} dt + \frac{V_{dc}}{2}. \tag{4.14}$$

Following a similar procedure for the second three-phase set, it can be demonstrated that:

$$V_{dc2} = \int \frac{i_{in1} - i_{in2}}{C_1 + C_2} dt + \frac{V_{dc}}{2}. \tag{4.15}$$

Therefore, if $i_{in1} \neq i_{in2}$, even if only temporarily, then the dc-link voltages become unbalanced. Only a controller compensation on these currents would balance the voltages again.

4.2 Novel active dc-link voltage balancing algorithm

As previously demonstrated, dc-voltages need to be actively balanced to control a dual three-phase IPMSM drive with a cascaded dc-link configuration. This voltage balancing must be carried out by regulating the power circulating through each three-phase set of the drive [78]. From the torque control solutions presented in chapter 3, three options are possible:

1. *Double three-phase* torque control approach: This solution incorporates an independent three-phase FOC block for each three-phase set, which allows, in a simple and intuitive manner, the inclusion of power-sharing capabilities. However, this approach does not consider the cross-coupling effects between winding sets. As a consequence, significant deviations from the commanded torque can be produced [64, 126, 128].

2. *Multiphase* torque control approach: This solution makes use of convenient vector transformations and considers cross-coupling effects between three-phase sets; therefore, accurate torque regulation is expected. However, this approach complicates the power-sharing capabilities of the controller, as per three-phase sets quantities are not explicit within this vector representation [77, 78]. Power-sharing capabilities can be provided by regulating the $D2-Q2$ synchronous frame, but this procedure is not straightforward and requires modified vector transformations [77–79, 125].

3. *Hybrid* torque control approach: This solution is proposed in this thesis. It incorporates a current set-point generation block that accounts for the cross-coupling effects while allowing independent regulation of the three-phase stator currents in a straightforward fashion.

Considering all the previous, this work adopts the proposed *Hybrid* torque control approach for the incorporation of voltage balancing capabilities. As this scheme regulates the currents in the $d-q$ synchronous frame, the power-sharing capabilities are enabled by properly acting over the current set-points. Three options are considered for the voltage balancing algorithm:

(a) To use both $d-q$ current components for the regulation of dc-link voltages [81, 82].

(b) To modify only d-axis current components for the dc-voltages balancing [76].
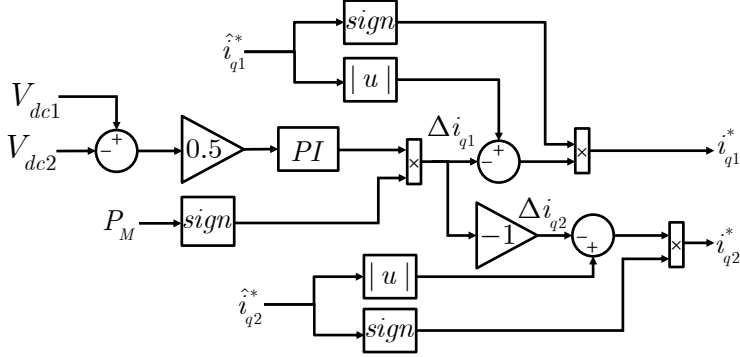
Fig. 4.5: Block diagram of the proposed active voltage balancing algorithm.

(c) To use only q-axis current components to modify the power delivery [71, 74, 77–79].

Option (c) is selected in this thesis, as the other two, (a) and (b), modify the flux-related d-axis currents. The modification of d-axis currents is to be avoided, as these current components are critical to keeping the stator voltages within the safe margin during FW operation.

Fig. 4.5 shows the block diagram of the proposed dc-link voltage balancing algorithm, which modifies the q-axis current references according to the deviation between the measured dc-link voltages of the two three-phase sets. Herein, the tracking error is calculated as follows:

$$V_{dc1} - \frac{V_{dc}}{2} = V_{dc1} - \frac{V_{dc1} + V_{dc2}}{2} = \frac{V_{dc1} - V_{dc2}}{2}. \tag{4.16}$$

As it is sufficient to act over one reference current per three-phase set, as stated before, it has been chosen to change $\hat{i}_{q1}^*$ and $\hat{i}_{q2}^*$, avoiding to vary the flux-related current set-points ($\hat{i}_{d1}^*$, $\hat{i}_{d2}^*$). A proportional-integral (PI) regulator computes the variations Δi_{q1} and Δi_{q2} required to balance the voltages (Fig. 4.5). Besides, $\Delta i_{q1} = -\Delta i_{q2}$, as the dc voltage variations fulfill $\Delta V_{dc1} = -\Delta V_{dc2}$. Then, q-axis references are modified as follows:

$$i_{qj}^* = (|\hat{i}_{qj}^*| - \Delta i_{qj})sign(\hat{i}_{qj}^*). \tag{4.17}$$

The PI gains have been set through simulations and empirically fine-tuned in the experimental test bench. Furthermore, the dynamics of the voltage bal-

ancing algorithm must be set following the heuristic rule of having, at least, a ten times faster inner-loop controller [137]. I.e., the dynamics of the balancing controller must be set at least ten times faster than the expected slew rate of the $\hat{i}_{q1}^*$ and $\hat{i}_{q2}^*$ currents. These set-points change at the same rate as the torque reference and the mechanical speed. Additionally, the dynamics of the balancing algorithm must be at least ten times slower than the dynamics of the current regulation loops.

Although theoretically, only a proportional control action is needed to achieve zero steady-state error in (4.7), an integral action has been incorporated. This control action can compensate for real machine phenomena such as manufacturing asymmetry, unbalance between three-phase assemblies, partial saturation, magnetic unbalances, or parasitic impedances. In the electric drive utilized in this thesis, automotive-grade components are implemented. Thus, parametric dispersion of the components and their parasitic resistance is expected to be minor but still unavoidable. Therefore, the voltage balancing algorithm is necessary, and even at steady-state, one three-phase set can drive more current than the other one. However, the current discrepancy is expected to be minor and not significantly affect the drive's power losses or lifetime.

Finally and as stated previously, increasing or decreasing the magnitude of the reference currents must be set according to the direction of the machine's power (P_M). Note that the machine is in motoring mode when $P_M > 0$ and regenerative operation when $P_M < 0$. Consequently, the balancing action is multiplied by 1 or -1 depending on the sign of P_M (Fig. 4.5). Note that the machine's power is estimated using the actual mechanical speed and electromagnetic torque.

4.3 Simulation assessment of torque control algorithm alternatives using $d - q$ FOC regulators

Initially and prior to experimental verification, both the *hybrid* and *double three-phase* torque control approaches, incorporating the proposed voltage balancing algorithm, have been evaluated to determine which of them performs best. To do so, an accurate model of the electric drive prototype developed within the FITGEN project has been implemented in Matlab/Simulink. The model of the electric machine has been developed using the *multiphase* modeling approach (see chapter 3) and includes the cross-coupling and magnetic saturation effects

Table 4.1: Main nominal parameters of the dual three-phase drive prototype.

Parameter	Value	Units
Electric machine		
Pole-pair number (N_P)	3	-
d-axis nominal inductance (L_{dnom})	55.6	μH
q-axis nominal inductance (L_{qnom})	291.3	μH
Stator resistance (R_s)	8.8	$m\Omega$
PM nominal flux (ψ_{PM})	0.029	Wb
Nominal power (P_{nom})	70	kW
Nominal torque $(T_{em,nom})$	80	Nm
Nominal mechanical speed $(w_{mech,nom})$	8000	r/min
Maximum power (P_{max})	135	kW
Maximum torque $(T_{em,max})$	170	Nm
Maximum mechanical speed $(w_{mech,max})$	22000	r/min
Maximum current per phase (I_{max})	235	Arms
Power electronics		
dc-link capacitance	320	μF
Switching frequency (f_{sw})	24	kHz
Total dc-link voltage	480 to 800	V

of the dual three-phase IPMSM. The Simpower/Simscape$^{\text{TM}}$ system library has been used to implement the models of the power electronics and the battery pack. The most relevant parameters of the FITGEN drive prototype are summarized in table 4.1.

Fig. 4.6 shows the block diagram of the *hybrid* toque controller incorporating the balancing algorithm presented in the previous section. The controller consists of: (1) the current set-point generator based on a VCT loop feedback, a speed normalization block, and offline-calculated 2D LUTs; (2) the current $\mathbf{T_2}$-regulation loops and (3) the *double zero-sequence injection* modulator. Thus, most of the components are the same as the ones described in chapter 3, with the exception of the voltage balancing block, which is included between the current set-point generator and the current regulation loops. Similarly, Fig. 4.7 shows the block diagram of the *double three-phase* toque controller, also incorporating the voltage balancing algorithm.
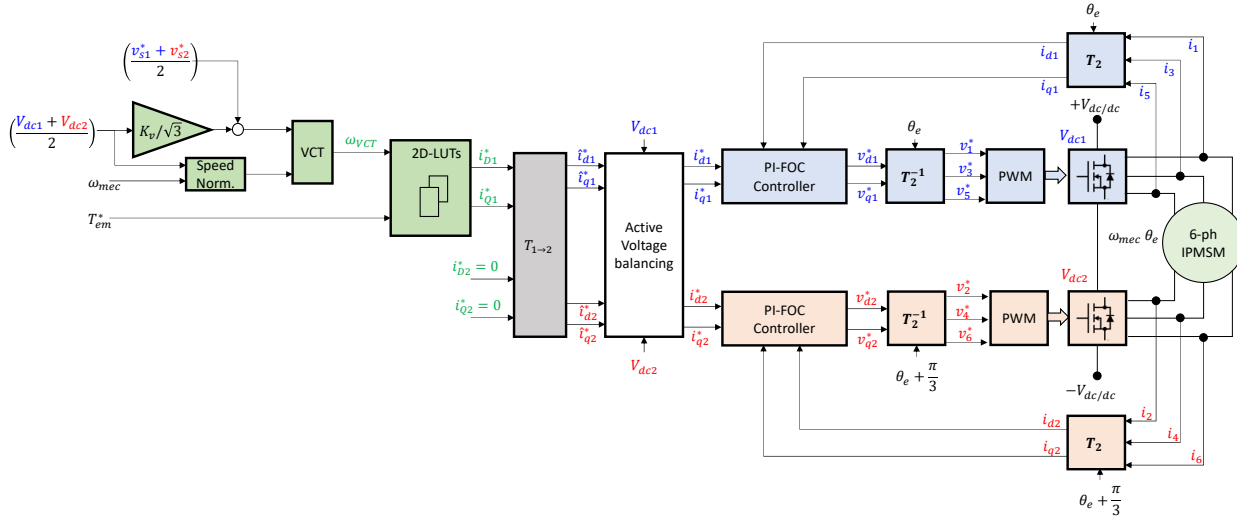
Fig. 4.6: Block diagram of the *hybrid* torque control approach with dc-link voltage balancing capabilities.
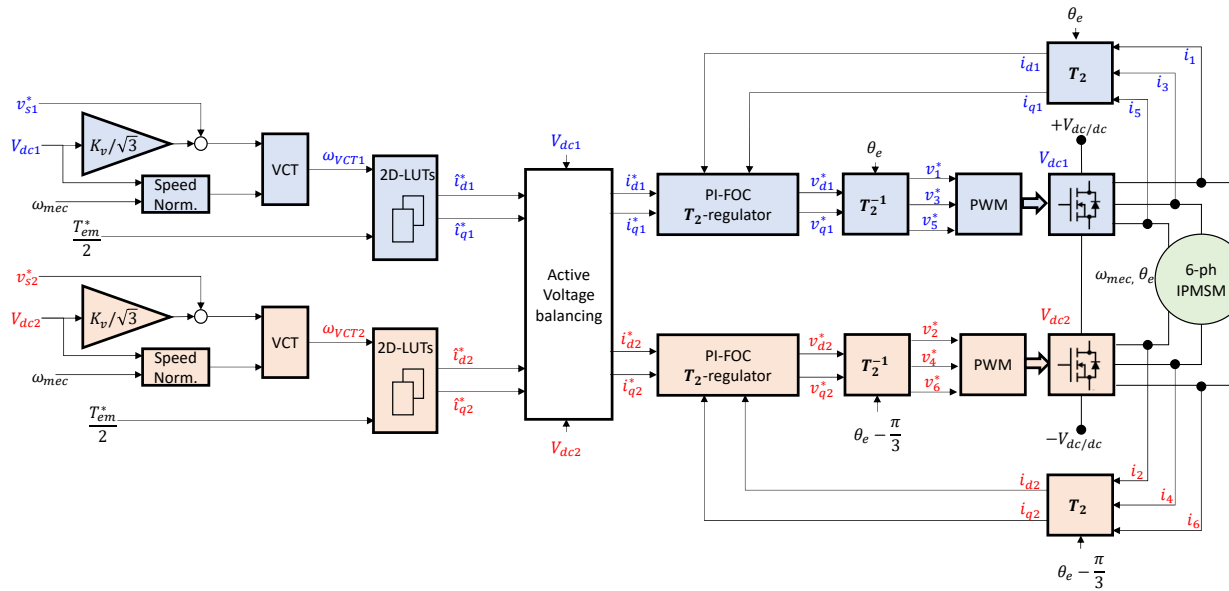
Fig. 4.7: Block diagram of the *double three-phase* torque control approach with dc-link voltage balancing capabilities.

Fig. 4.8 shows the performance of the drive when the *hybrid* control approach of Fig. 4.6 is used for torque regulation. In this particular simulation, the machine is operated through the whole speed range, commanding a constant torque reference of 80 Nm (rated value). A maximum power limit of 135 kW is set. As the proposed controller considers the coupling effects, no deviations between the commanded and the obtained torque are observed in general, during MTPA, FW at constant-torque, and FW on max-current operation [Fig. 4.8(a)]. A slight deviation in the torque set-point tracking is observed, at $t = 3.5$ s, as a result of the quantization of the LUT data, which highlights the importance of having a minimum resolution within the LUTs. In such a case, the VCT algorithm keeps the voltage constraint limit during the transition between FW and MTPV regions. As stated before, this transition can be smoothed by increasing the amount of data stored in the LUTs.

Fig. 4.8(b) shows the performance of the current regulation loop for the first three-phase set. As expected, the stator currents track their set-points for the entire speed range. Until $t = 1.5$ s, the drive is operated in the MTPA region. Next, it is operated in FW, at constant torque, between $t = 1.5$ s and $t = 2.7$ s. Then, the commanded torque is limited due to the maximum power constraint. As Fig. 4.8(c) shows, the field weakening operation is correctly performed for the whole speed range for $k_v = 0.9$. What is more, the voltage balancing is satisfactorily performed for all the operation regions [Fig. 4.8(d)]. In this simulation, the total dc-link voltage is set to 640 V by the dc/dc converter. The dc-link voltage ripple is lower than 1 % of the total dc-link voltage. Due to the non-linear nature of the dc-link voltage dynamics, the response of the voltage balancing controller is not uniform over the entire speed range.

In order to further analyze the performance of the *hybrid* controller in simulation, Fig. 4.9 shows the results obtained when a stretch of the World Harmonized Light-duty Vehicle Test Procedure (WLTP) driving cycle is commanded. Fig. 4.9(a) illustrates the machine's mechanical speed and the electromagnetic torque. The regulation of the stator currents is shown in Fig. 4.9(b), while Fig. 4.9(c) shows the performance of the voltage balancing algorithm and the FW algorithm. All these results demonstrate that the *hybrid* torque controller, including the proposed balancing algorithm, properly operates under dynamically changing driving conditions.

In Fig. 4.10, a constant torque set-point is commanded, while the mechanical speed remains constant (80 Nm and 5000 rpm). At $t = 1$ s, the voltage balancing algorithm is deactivated, leading to a complete loss of control. Thus, it is demonstrated by simulation that the previous mathematical analysis holds true, as slight current variations lead to a significant dc-link voltage unbalance.
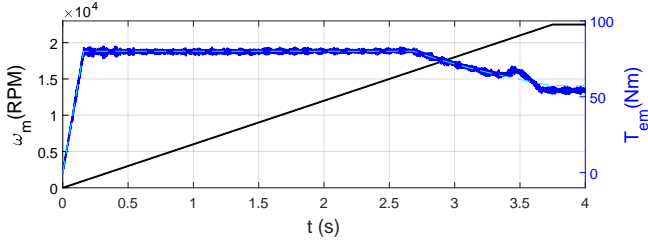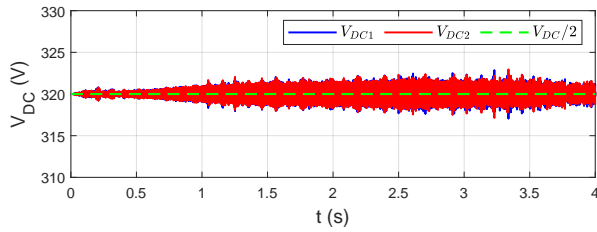
(a) Torque and speed.
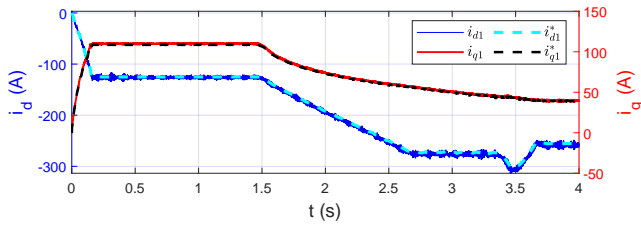
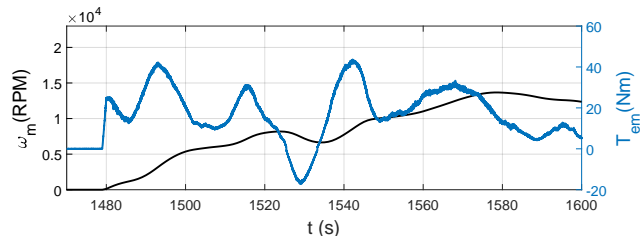(b) Synchronous reference frame currents.
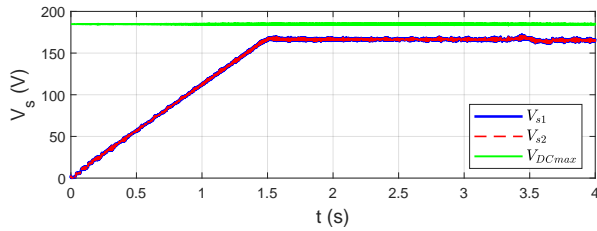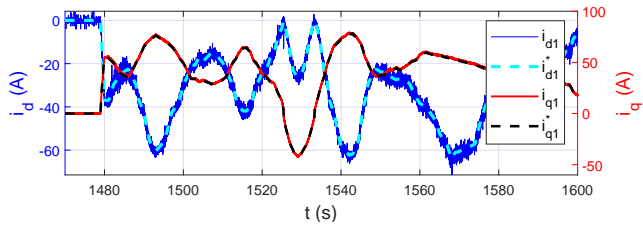

(c) Field weakening control results.

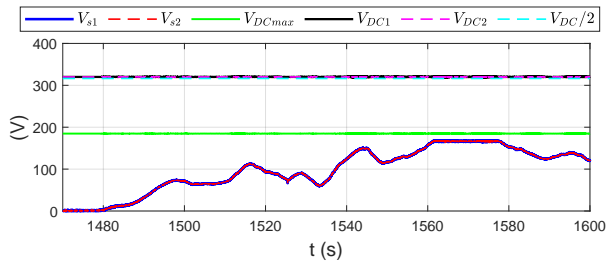(d) Voltage balancing control results.

Fig. 4.8: Dual three-phase IPMSM regulation using the *hybrid* control approach (I): nominal torque operation over the whole speed range.
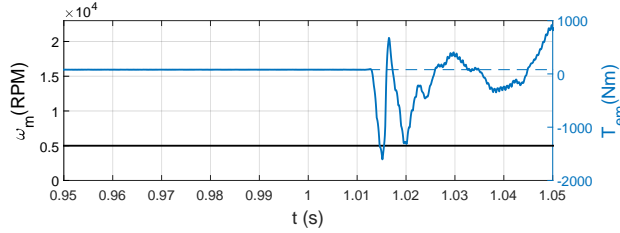
127

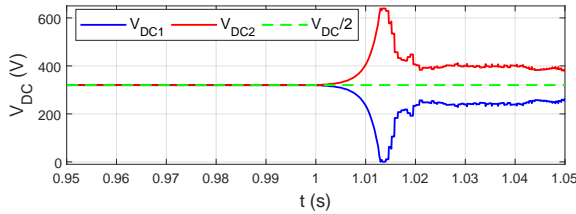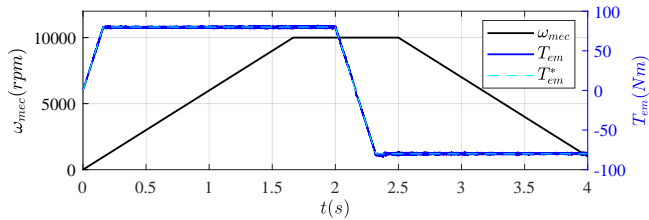(a) Torque and speed.

(b) Synchronous reference frame currents.

(c) dc-link and stator voltage control results.

Fig. 4.9: Dual three-phase IPMSM regulation using the *hybrid* control approach (II): WLTP driving cycle test results.

(a) Torque and speed.

(b) Voltage balancing control results.

Fig. 4.10: Dual three-phase IPMSM regulation using the *hybrid* control approach (III): disconnection of the voltage balancing control at $t = 1$ s.

Therefore, it is confirmed that the utilization of a dc-link voltage balancing controller is mandatory for such a cascaded configuration.

Fig. 4.11 shows the operation of the drive when the dc-link voltage regulation strategy, proposed in [150], is integrated into the control system with the *hybrid* controller and the balancing algorithm. This strategy regulates the input side dc/dc converter and varies the total dc-link voltage depending on the speed and torque operating points to minimize overall power losses. The obtained results demonstrate the correct operation of the proposals under stringent transient conditions such as torque reversal, speed ramps, and varying dc-link voltage.

Finally, the simulation results of Fig. 4.12 show the performance of the drive when the *double three-phase* control approach is utilized. As it has been previously done for the *hybrid* controller (see Fig. 4.8), the machine is operated over the whole speed range, applying a torque reference of 80 Nm with a maximum power limit of 135 kW. As for the *hybrid* torque control approach, the dc-link voltage balance is ensured thanks to the proposed balancing algorithm. However and as theoretically expected, a slight deviation in torque is observed
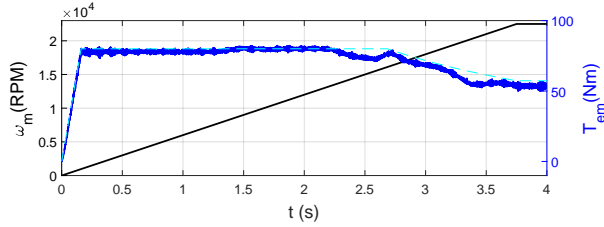
(a) Torque and speed.
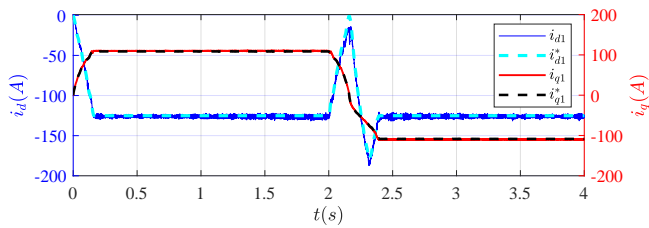
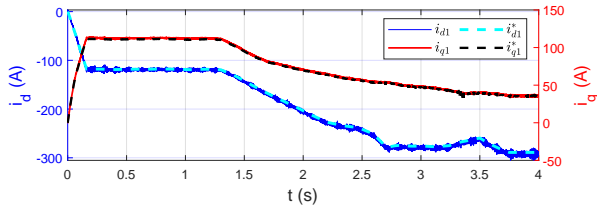(b) Synchronous reference frame currents.
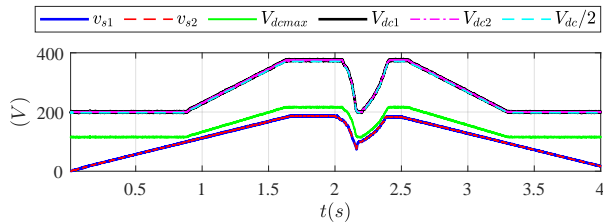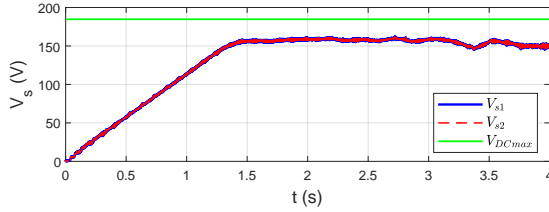

(c) Voltage balancing control results.

Fig. 4.11: Dual three-phase IPMSM regulation using the *hybrid* control approach (IV): optimal dc-voltage adaptation.
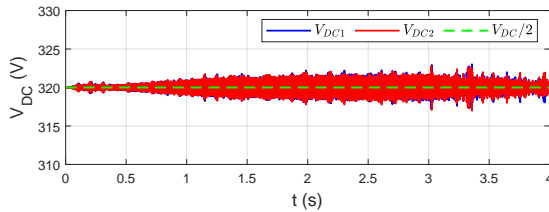
(a) Torque and speed.

(b) Synchronous reference frame currents.

(c) Field weakening control results.

(d) Voltage balancing control results.

Fig. 4.12: Dual three-phase IPMSM regulation using the *double three-phase* control approach.

during MTPA operation. During FW, the deviations between the commanded and actual torque increase with speed. Furthermore, a non-smooth stator voltage tracking is observed. All these phenomena are produced as the *double three-phase* controller neglects the coupling effects between the two three-phase sets. Thus, these simulation results show that it is more convenient to use the *hybrid* torque regulation scheme proposed in this thesis over the conventional *double three-phase* approach. Consequently, the *double three-phase* approach is discarded, and the following sections focus on the *hybrid* torque control approach.

4.4 Adapted PWM scheme for symmetrical IPMSM with overlapping windings

Following the *hybrid* control approach, the voltage references provided by the regulators are transformed from the $d - q$ reference frames into the respective three-phase values. Finally, the PWM module synthesizes the firing pulses, where a min-max type zero sequence injection block is included for the duty-cycle calculation to maximize the linear range of the output voltage [156].

In the symmetrical IPMSM prototype developed within the FITGEN project, the windings of both three-phase sets are overlapped. As a consequence, some parts of the windings share the same stator slots. Therefore, the two sets present a mutual leakage inductance, highly coupling the two windings at PWM frequency. Adopting a standard PWM technique causes an extremely high current ripple, resulting in additional power losses, acoustic noise, and poor control performance [78,85]. All these effects are strongly mitigated by using phase-shifted or interleaved PWM algorithms [83, 157, 158]. In [159, 160], the mathematical expressions that allow calculating the optimal phase-shift between the carrier of each three-phase set of a six-phase machine are detailed. Following such mathematical analysis, in this thesis, a phase-shift of π radians is applied (Fig. 4.13).

Fig. 4.14 shows the general block diagram of the proposed *hybrid* torque control strategy, which includes the novel voltage balancing algorithm and incorporates the interleaving modulation approach described above.

4.5 Experimental results

In this section, the experimental results carried out to validate the proposed *hybrid* torque control with dc-voltage balancing capabilities (Fig. 4.14) are
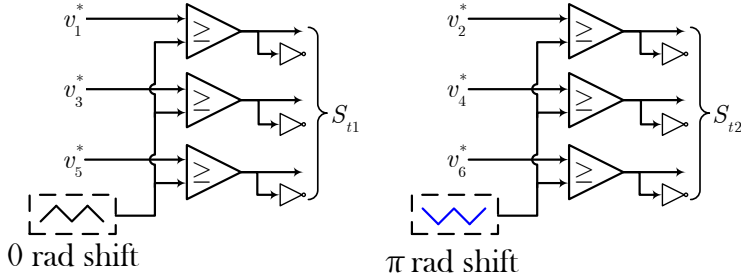
Fig. 4.13: Implemented interleaved PWM strategy with a π radians phase-shift for the second winding set.

presented. First of all, the experimental results carried out in a laboratory test bench are provided. During these experimental tests, the electric drive was operated under various speed and torque profiles to validate the performance of the components of the controller. Next, the controller's performance is evaluated using four driving cycles. Each cycle emulates quite different driving conditions; in this manner, the electric drive is validated in a wide variety of scenarios. Finally, the verification of the control proposal at TRL-7 is achieved in a real EV, including dynamometer and on-road tests.

4.5.1 Experimental results obtained in a laboratory test bench

Experimental platform description

Fig. 4.15 shows the experimental platform initially used to validate the proposed control approach at TRL-6. It includes a full-scale symmetrical dual three-phase IPMSM prototype, which development was led by BRUSA Elektronik AG within the FITGEN project. This IPMSM prototype is coupled to a load machine through a torque transducer. As is usual in this type of application, the load machine is speed regulated, while the machine under test is torque regulated. A six-phase SiC inverter with cascaded dc-link capacitors is incorporated at the rear side of the machine housing. Table 4.1 summarizes the most relevant nominal parameters of the electric drive prototype.
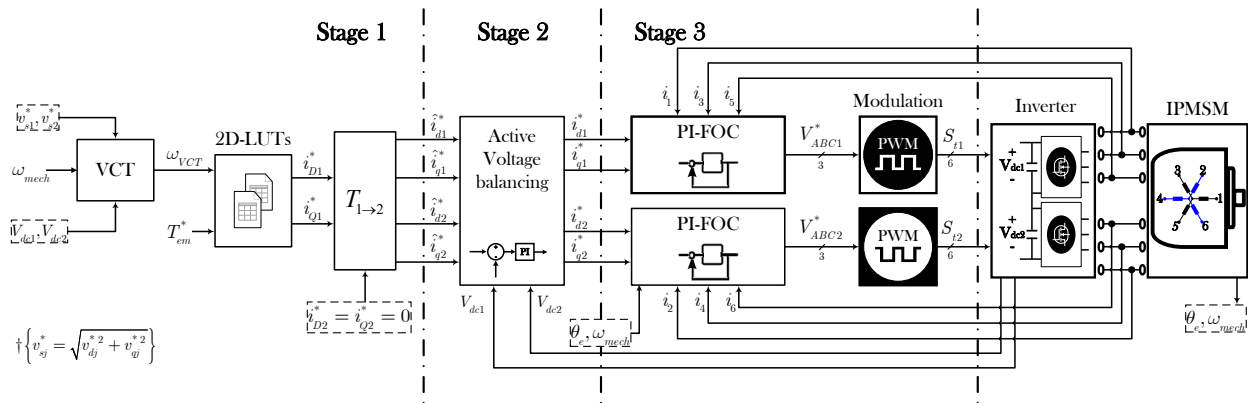
Fig. 4.14: Block diagram of the proposed *hybrid* torque control incorporating the voltage balancing algorithm and interleaved PWM.

Table 4.2: Main nominal parameters of the dc/dc converter.

Parameter	Value	Units
High side voltage range	150 to 750	V
Low side voltage range	50 to 600	V
Nominal current (low side)	$+/-$ 300	A
Maximum current (low side)	$+/-$ 400	A
Nominal power	180	kW
Efficiency	98.9	%
Switching frequency	41	kHz
Power density	6.4	kW/kg

A dSPACE MicroAutoBox II Rapid Control Prototyping (RCP) platform, including an IBM PPC 750GL at 900 MHz and 16 parallel 16-bit ADC channels with a conversion rate of 1 MS/s, has been used to implement the proposed control algorithm. In order to guarantee real-time execution and to make the best use of available computational resources, the control software has been divided into three stages (Fig. 4.14). Each stage runs at a different frequency depending on the required dynamic response of the tasks it incorporates. Stage 1 runs at 200 S/s (set-point generator), stage 2 runs at 2 kS/s (voltage balancing), and stage 3 runs at a sampling frequency of up to 24 kS/s (current regulation and duty-cycle determination). The PWM frequency is set to 24 kHz. Finally, to mitigate the harmful effect of EMIs in the low-voltage and high-frequency firing signals, the controller provides these signals through fiber optics to the six-phase inverter.

Additionally, a BDC546 bidirectional dc/dc converter from BRUSA Elektronik AG[1] has been utilized to feed the SiC six-phase inverter. The main nominal parameters of this device are summarized in table 4.2.
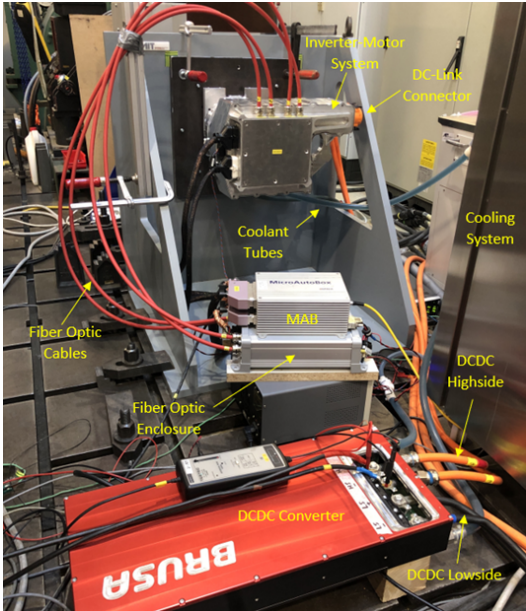
Current regulation, field weakening, and voltage balancing results

Several experimental tests are carried out to validate the controller's main components, i.e., the current (torque) regulation loops, the voltage balancing algorithm, and the current set-point generation block (MTPA and FW). These tests

---

[1]https://www.brusa.biz/portfolio/bdc546/
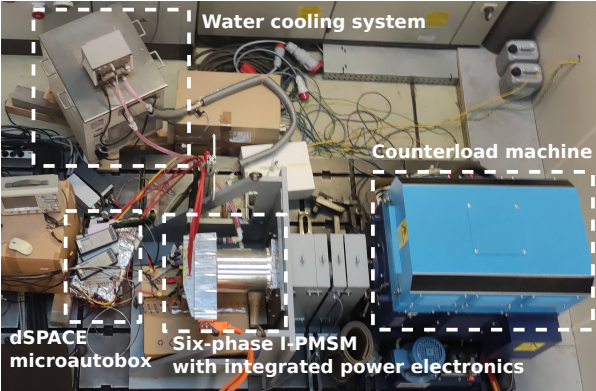
(a) Top view.

(b) Front view.

Fig. 4.15: Experimental platform including the dual three-phase IPMSM drive, mounted at AIT's Vienna facility.

serve to assess the controller's performance during both in steady-state operation and during transients. Thus, torque steps, torque reversals, and speed ramps are commanded.
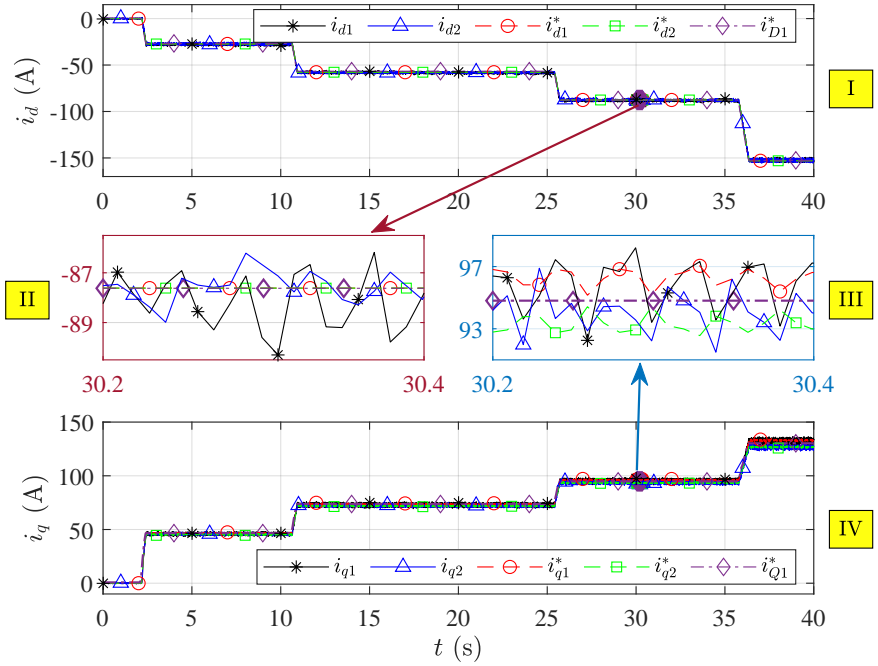
Fig. 4.16 shows the experimental results obtained when the machine rotates at 2500 rpm and various torque steps are commanded up to 100 Nm. The dq currents of both three-phase winding sets are regulated to the MTPA reference values [Fig. 4.16(a)-I and 4.16(a)-IV]. These figures show that the control successfully tracks the current set-points in the d- and q-axes. The current control performs properly, showing zero steady-state error, with an average current ripple lower than 5 %. The high-frequency variations within the $d - q$ currents result from the current ripple inherent to the low inductance value of the stator and also, in part, due to measurement noise. This current ripple is unavoidable but very minor when compared to the machine's rated current.

Thanks to the correct regulation of the stator currents, the electromagnetic torque properly tracks the reference torque [Fig. 4.16(b)]. Minor inaccuracies in the drive FEM parameters cause slight differences between the commanded and the measured torque. Note that the slew rate of the reference torque is limited to 100 Nm/s (1250 Nm/s in wheel due to the gearbox) to ensure driver's and passenger's comfort. This limitation of the rate of change of the torque set-point also limits the slew rate of the dc-link current and stator current set-points ($\hat{i}_{d1}^*$, $\hat{i}_{q1}^*$, $\hat{i}_{d2}^*$, $\hat{i}_{q2}^*$), which allows tuning fast enough dynamics for the dc-link voltage balancing controller.

The control action of the balancing algorithm is illustrated in detail in Fig. 4.16(a). As it can be seen from Fig. 4.16(a)-III, the balancing algorithm modifies the q-axis current references since the mean values of the references i_{q1}^* and i_{q2}^* are ± 1 A away from the LUT reference i_{Q1}^*. In addition, i_{q1}^* and i_{q2}^* fluctuate in steady state conditions with an amplitude of ± 1 A (only 0.5 % of the maximum inverter current). In contrast, the d-axis current references are unaltered during steady-state conditions [Fig. 4.16(a)-II].

Fig. 4.17 shows the response of the voltage balancing controller. In this test, the dc/dc converter is commanded to set a constant voltage of 480 V. As this figure shows, the input voltage of each inverter unit is balanced to 240 V, exhibiting a small voltage ripple of $\pm$ 0.5 V. The dynamics of the voltage balancing loop are fast enough to keep V_{dc1} and V_{dc2} around $V_{dc}/2$ during steady-state and transients (Fig. 4.17).

In the following test, the response of the electric drive prototype is assessed under sharp transient torque commands at a constant speed (2300 rpm). First, various torque steps are applied up to 120 Nm. Then, a torque reversal from

(a) $d - q$-axis currents.
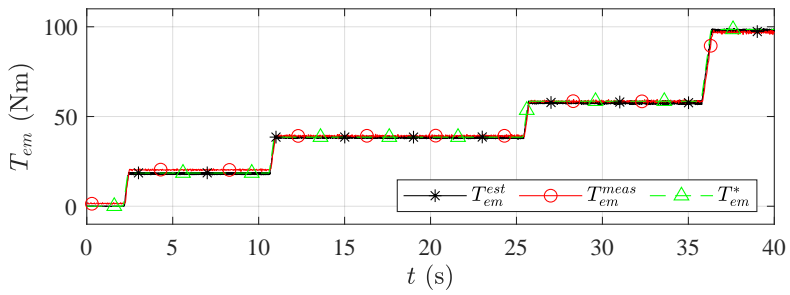
(b) Electromagnetic torque.

Fig. 4.16: Experimental results obtained when various torque steps are commanded (I).
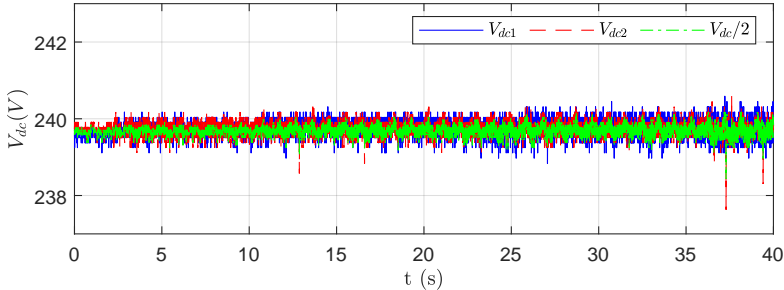
Fig. 4.17: Response of the voltage balancing when various torque steps are commanded (II).

120 Nm to -120 Nm is commanded [4.18(c)]. Thus, the drive's response in motoring and regenerative mode is successfully verified. As Fig. 4.18(a) and 4.18(b) show, the current loops successfully track the current set-points in both three-phase sets. Fig. 4.18(a)-I and 4.18(a)-II show a zoomed view of the steady-state currents during a torque command of 100 Nm. Again, the action of the balancing algorithm over q-axis currents is illustrated.

To validate the FW algorithm, including the VCT loop, the speed normalization block, and 2D LUTs, the electric machine is accelerated from a standstill up to 19000 rpm [Fig. 4.19(a)], while a constant torque set-point of 30 Nm is commanded. Thanks to the proposed field weakening approach, the modulus of the two three-phase set stator voltages v_{s1} and v_{s2} are kept below the maximum voltage limit of $V_{dcmax} = k_v V_{dc}/\sqrt{3}$ during the entire test [Fig. 4.19(b)]. Note that the machine is not driven to its maximum speed (22.500 rpm) due to limitations in the load machine of the test bench. The dc-link voltage of each inverter unit is kept balanced thanks to the proposed voltage balancing algorithm [Fig. 4.19(c)]. In this test, the total dc-link voltage is fixed to 520 V. It must be remembered that these voltages would become unbalanced and jeopardize the integrity of the power system if the balancing algorithm is not active. Note that the deactivation of the balancing algorithm has been only carried out during simulations, as its deactivation in the experimental test bench can lead to a potentially destructive event for the power electronics that constitute the electric drive. Finally, a maximum voltage ripple of ± 3 V is observed in the dc-link voltages. As expected, the voltage ripple varies with the operation point
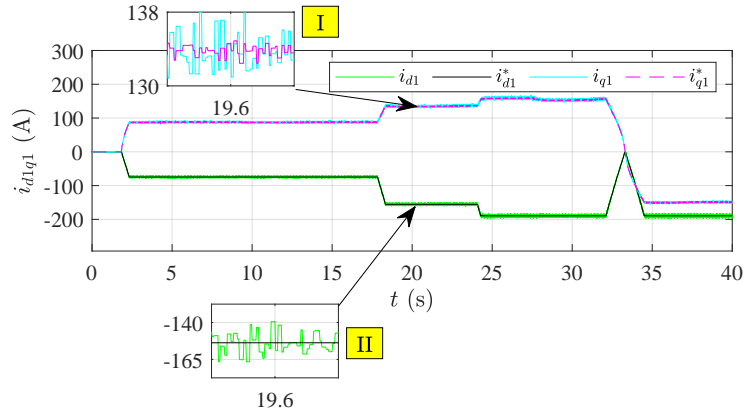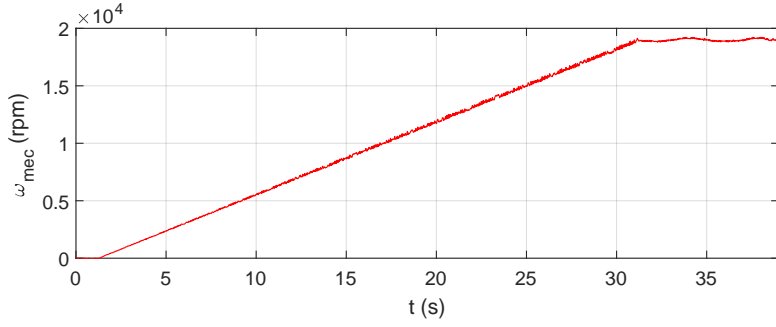
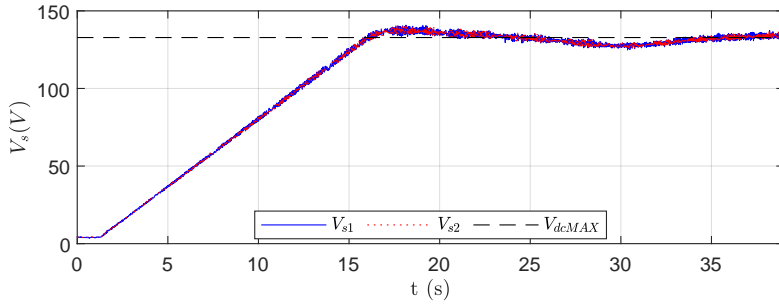(a) $d1q2$-axis currents.
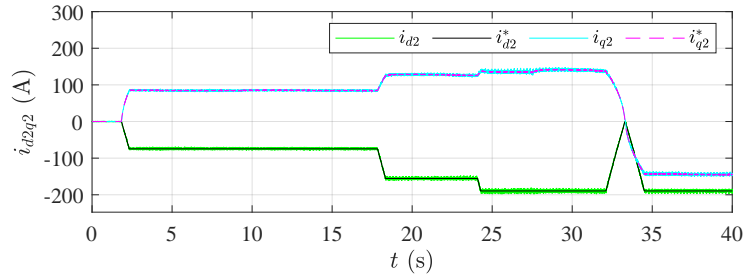
(b) $d2q2$-axis currents.
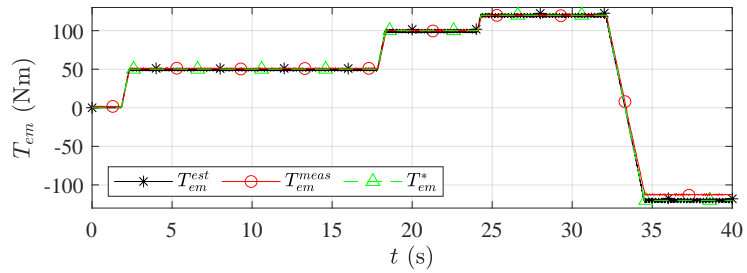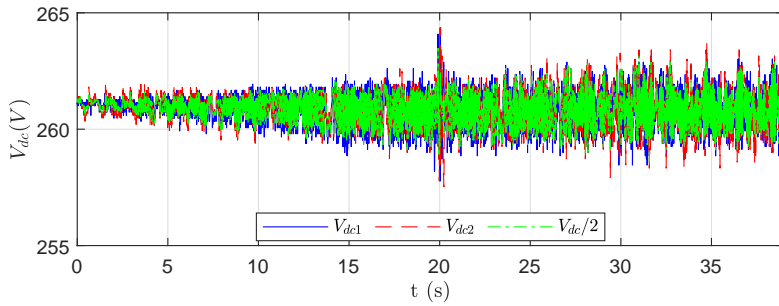

(c) Electromagnetic torque.

Fig. 4.18: Experimental results obtained for various torque steps and torque reversal.

(a) Mechanical speed.

(b) Stator voltages.

(c) dc-link voltage balancing.

Fig. 4.19: Experimental results obtained when accelerating the dual three-phase IPMSM up to 19000 rpm.

as predicted by the dc-link mathematical model presented at the beginning of this chapter.

Interleaved PWM

The performance of the electric drive is initially tested under the application of a conventional carrier-based PWM scheme (see chapter 3) and later with the interleaved PWM pattern previously described in this chapter. Fig. 4.20 shows the phase currents obtained during such early tests, where the *Double zero-sequence injection modulation technique* [141] is used with no phase shift, and a 50 Nm torque is commanded at 7800 rpm. Fig. 4.20(a) shows the oscilloscope capture of the phase currents[2]. In order to make clear the information in this capture, the oscilloscope traces are processed and plotted with MAT-LAB, correctly showing the time and current magnitudes in the x- and y-axes [Fig. 4.20(a)]. Then, these traces are transformed to the frequency domain using a Fast Fourier Transform (FFT). Fig. 4.20(c) shows the high undesired phase current harmonic components generated at the fundamental and third harmonic of the switching frequency (f_{sw}), where f_e is the actual electric frequency of the machine.

In contrast, Fig. 4.21 shows how the utilization of the interleaved PWM effectively eliminates the ripple in the phase currents. In this test, a 40 Nm torque is commanded at 7800 rpm. Fig. 4.21(a) shows the oscilloscope capture of the phase currents[3]. Apparent high-frequency electromagnetic noise is caused as a result of using current probes with low disturbance rejection. Such fictitious high-frequency noise is not present in the real machine per-phase currents. The oscilloscope traces are processed again and transformed (FFT), as shown in Figs. 4.21(b) and 4.21(c), respectively. Fig. 4.21(b) shows sinusoidal currents, while Fig. 4.21(c) corroborates the elimination of the undesired phase current components generated at the fundamental and third harmonic of the switching frequency (f_{sw}).

Note that Figs. 4.20 and 4.21 illustrate the behavior of the phase currents for two different commanded torque set-point values (50 Nm and 40 Nm, respectively). However, this does not make any difference to the more revealing

---

[2]Oscilloscope configuration: the vertical-scale is 2 V/div, the input impedance is 1 MΩ, the bandwidth is 500 MHz, the horizontal-scale is 1 ms/div, the sample-rate is 25 MS/s, and the record length is 250 kpts.

[3]Oscilloscope configuration: the vertical-scale is 2 V/div, the input impedance is 1 MΩ, the bandwidth is 500 MHz, the horizontal-scale is 1ms/div, the sample-rate is 250 MS/s, and the record length is 2.5 Mpts.
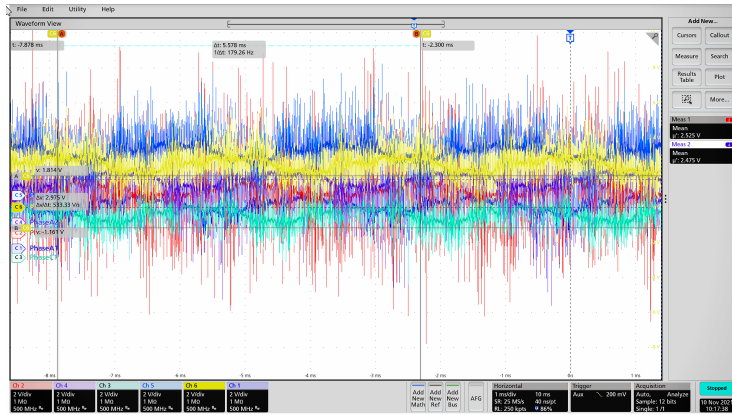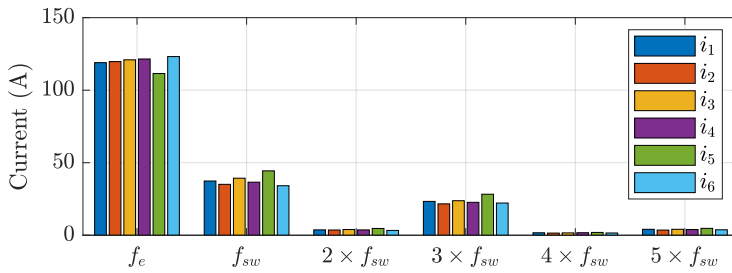
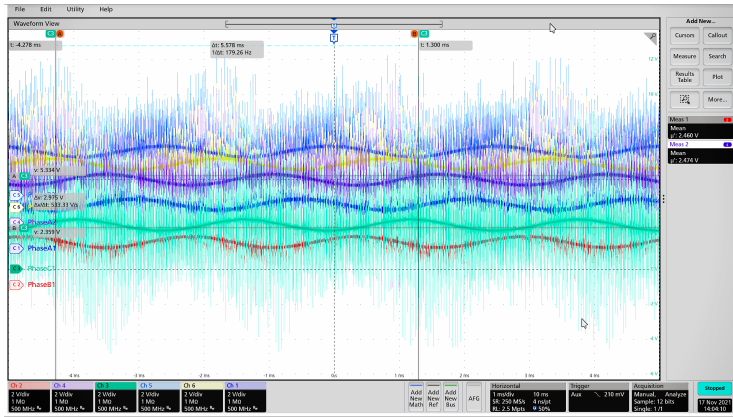(a) Oscilloscope capture
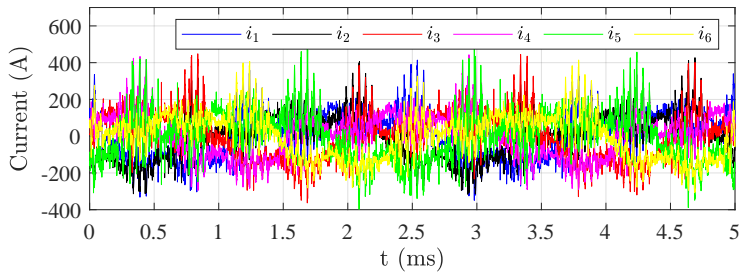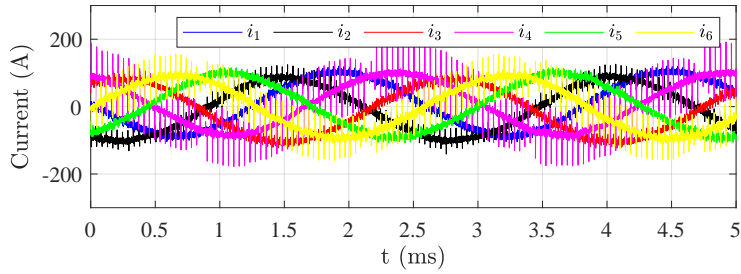

(b) Lowpass-filter
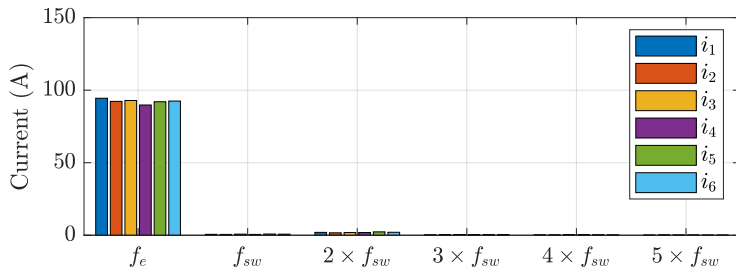

(c) Frequency spectrum

Fig. 4.20: Phase currents with high ripple obtained without interleaving during early tests, when a 50 Nm torque is requested at 7800 rpm.

143

(a) Oscilloscope capture

(b) Lowpass-filter

(c) Frequency spectrum

Fig. 4.21: Phase currents with low ripple thanks to the interleaved PWM, when a 40 Nm torque is requested at 7800 rpm.

Table 4.3: Summary of the main features of the WLTP driving cycle.

Average speed	Low	Medium	High	Extra-high	Total
Duration (s)	589	433	455	323	1800
Standstill duration (s)	150	49	31	8	235
Distance (km)	3.10	4.76	7.16	8.25	23.27
% of time at standstill	26 %	11 %	7 %	2 %	13 %
Max speed (km/h)	56.5	76.6	97.4	131.3	131.3
Avg speed - stops (km/h)	25.3	44.5	60.7	94.0	53.5
Avg speed + stops (km/h)	18.9	39.4	56.5	91.7	46.5
Min acceleration (m/s^2)	-1.5	-1.5	-1.5	-1.44	-1.5
Max acceleration (m/s^2)	1.16	1.61	1.66	1.05	1.66

aspects all these figures show, i.e., the elimination of the high-frequency harmonic components generated as a consequence of the particular machine winding arrangement, thanks to the application of the interleaved PWM algorithm.
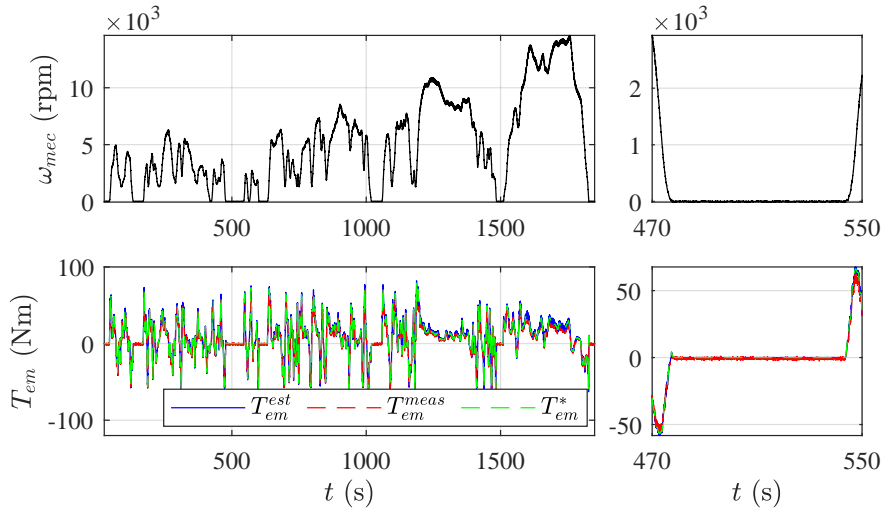
Driving cycle results

To conclude with the laboratory test bench experimentation, the proposed control solutions are validated under realistic driving conditions. To do so, four driving cycle tests are carried out: WLTP, US06, RWC1, and RWC2.

Figs. 4.22 and 4.23 show the experimental results obtained when the drive is operated under the WLTP driving cycle[4] at a constant total dc-link voltage of 520 V. This standardized driving cycle is utilized for bench-marking the energy consumption, range, pollutants, and CO_2 emissions of fuel, hybrid and electric vehicles. The WLTP driving cycle is divided into four parts with different average speeds: low, medium, high, and extra high. Table 4.3 summarizes the main features of the WLTP driving cycle.

As shown in Fig. 4.22(a), the generated electromagnetic torque successfully tracks the reference one. The performance of the current regulators is shown in Fig. 4.23(a), where i_{d1} and i_{q1} currents of the first winding set correctly track their references. Equivalent results are obtained for the second winding set [Fig. 4.23(b)]. These results validate both the set-point generation approach and the convenience of the utilized vector representation. What is more, the voltages of the cascaded dc-link capacitors are again kept balanced for the whole

---

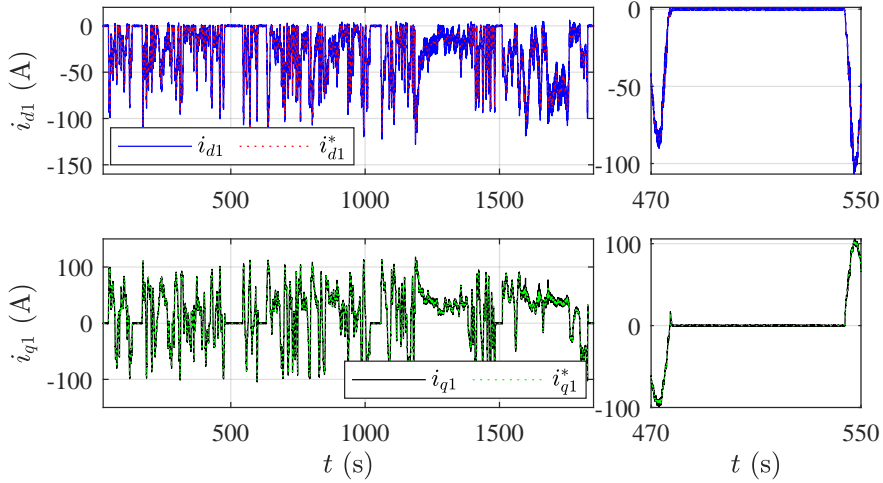[4]https://www.wltpfacts.eu/what-is-wltp-how-will-it-work/
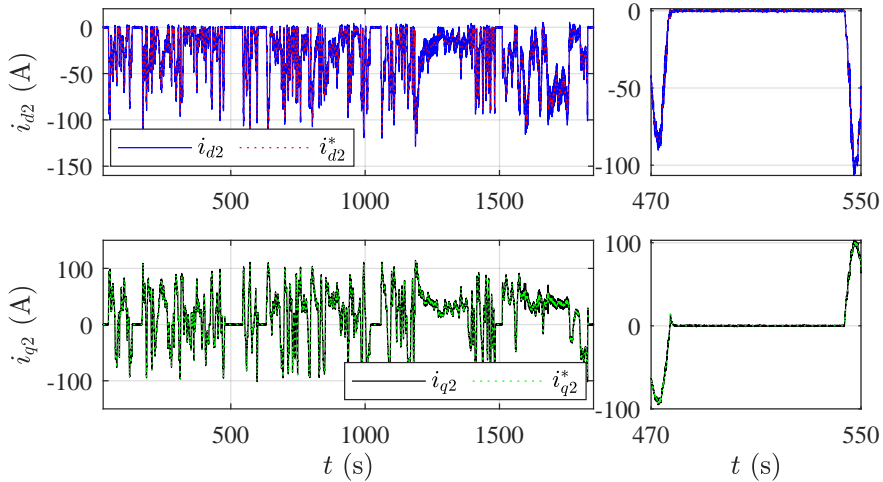
(a) Torque and speed.
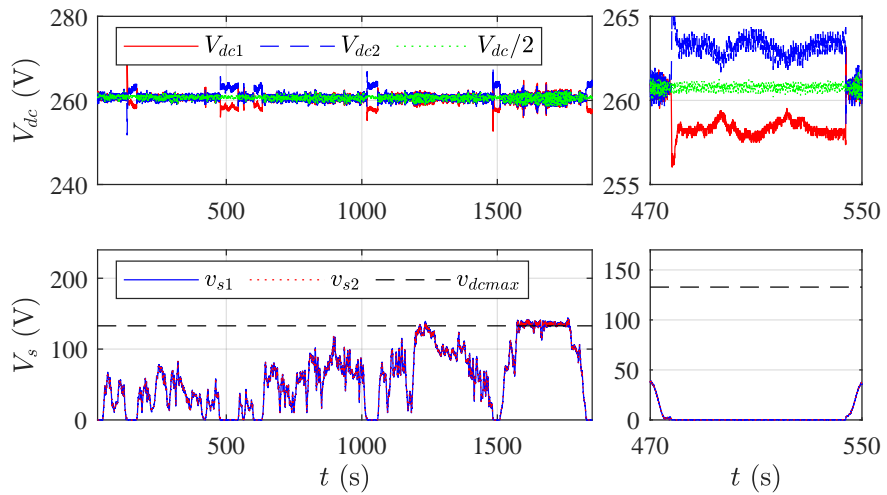
(b) Stator and dc-voltages.

Fig. 4.22: Experimental laboratory results obtained under the WLTP driving cycle and fixed dc-link voltage (I).

(a) Set 1 $d-q$ stator currents.

(b) Set 2 $d-q$ stator currents.

Fig. 4.23: Experimental laboratory results obtained under the WLTP driving cycle and fixed dc-link voltage (II).

147

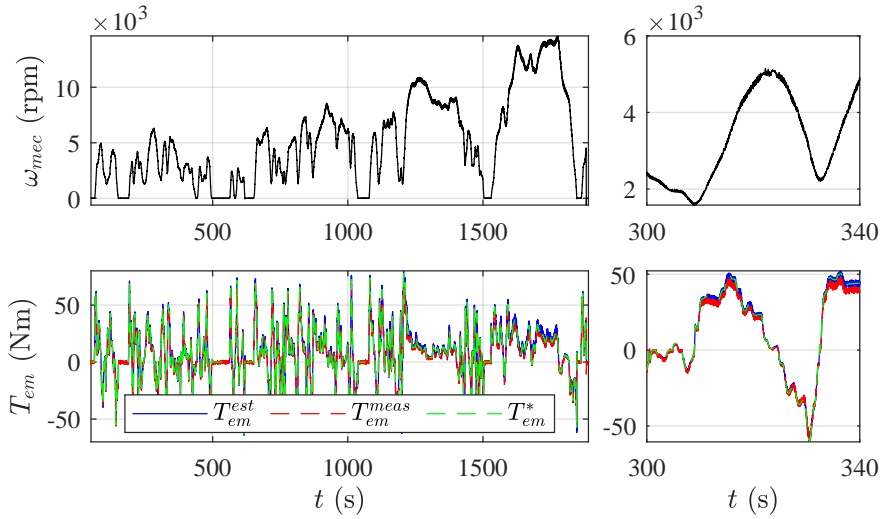Table 4.4: Summary of the main features of the RWC1 driving cycle.

Average speed	Low	Medium	High	Extra-high	Total
Duration (s)	304	316	900	640	2160
Standstill duration (s)	134	143	402	130	809
Distance (km)	0.5	1.3	3.3	4.2	9.3
% of time at standstill	44 %	45 %	44 %	20 %	37 %
Max speed (km/h)	33.5	44.3	48	62.5	62.5
Avg speed - stops (km/h)	10.2	24.2	26.6	29.7	24.8
Avg speed + stops (km/h)	5.7	13.36	14.5	23.68	15.5

trip thanks to the proposed balancing scheme [Fig. 4.22(b)]. In general, a dc-link voltage ripple of approximately 2 V is obtained. However, higher deviations are produced while the vehicle is at standstill (at zero speed and with zero torque command), as the balancing algorithm is disabled to avoid any torque production. The zoomed-in figures, right side of Figs. 4.23 and 4.22, show the detailed behavior of the drive during zero speed with zero torque command. Minor variations up to ±5 V with respect to the reference voltage are observed. However, the action of the balancing algorithm leads to a fast equilibration of both voltages once the machine produces torque again.

Next, the experimental results obtained when applying the WLTP driving cycle under a variable dc-link voltage are presented in Figs. 4.24 and 4.25. As previously described in the simulations section, this algorithm modifies the total dc-link voltage, in this case between 480 V and 700 V, according to the actual operating point of the drive. As Fig. 4.22(b) shows, the dc-link voltage applied by the dc/dc converter increases with the mechanical speed of the machine to extend the MTPA region and avoid, as much as possible, FW operation. As in the constant-voltage scenario, the proposed control solutions successfully regulate the drive during the entire driving cycle. The right-side zoomed-in of Figs. 4.24 and 4.25 illustrate the detailed operation of the electric drive during medium speed and torque variations.

Then, the Real World driving Cycle 1 (RWC1[5]) is applied to the test bench. This cycle allows assessing the electric drive performance during a real-world purely urban cycle driven in Turin (Italy). The RWC1 lasts 36 minutes and covers a distance of 9.3 km. Table 4.4 summarizes the features of the RWC1

---

[5]https://fitgen-project.eu/files/FITGEN_D1.1_Driving_cycles_specification_and_end-user_requirements_2019-05-23_FINAL.pdf
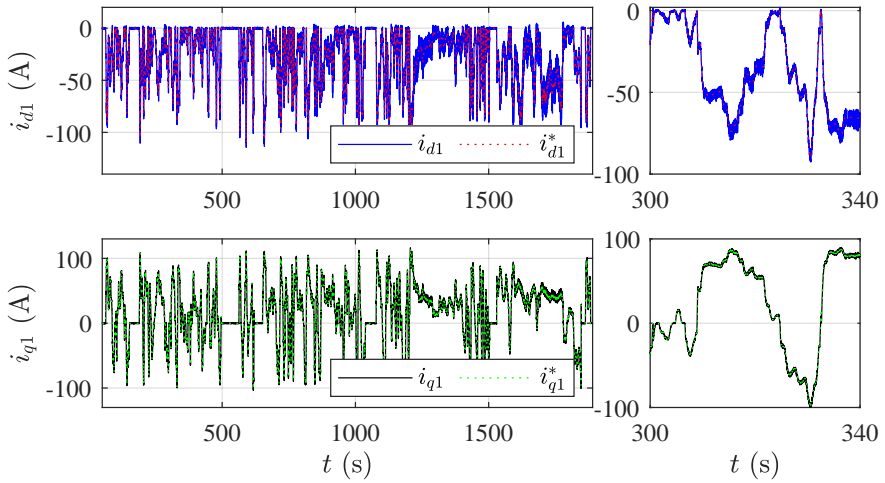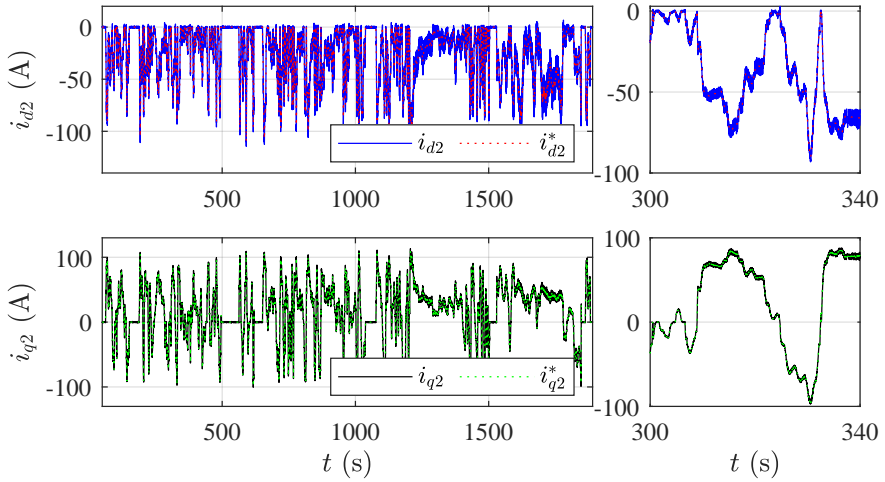
(a) Torque and speed.
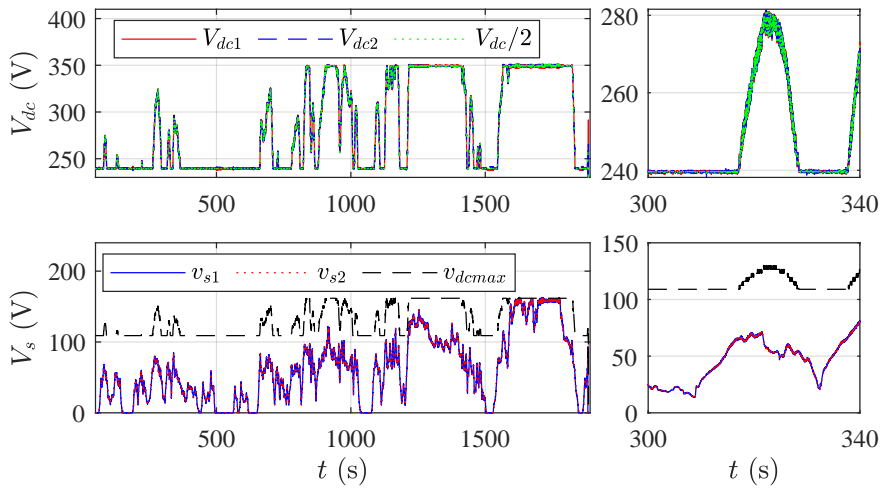
(b) Stator and dc-voltages.

Fig. 4.24: Experimental laboratory results obtained under the WLTP driving cycle and variable dc-link voltage (I).

(a) Set 1 $d-q$ stator currents.

(b) Set 2 $d-q$ stator currents.

Fig. 4.25: Experimental laboratory results obtained under the WLTP driving cycle and variable dc-link voltage (II).

Table 4.5: Summary of the main features of the RWC2 driving cycle.

| Average speed	Low	Medium	High	Extra-high	Total
Duration (s)	250	2039	1721	790	4800
Standstill duration (s)	159	168	94	148	569
Distance (m)	0.5	21.9	19.8	9.8	52
% of time at standstill	63 %	8.2 %	5.4 %	18 %	12 %
Max speed (km/h)	32.1	70.7	93.9	117	117
Avg speed - stops (km/h)	19.3	42.1	43.7	55.1	44.2
Avg speed + stops (km/h)	6.9	38.7	41.3	44.7	39

driving cycle. Low speeds and high torque requirements characterize this cycle.

Figs. 4.26 and 4.27 show the experimental laboratory results obtained under the RWC1 driving cycle and fixed dc-link voltage (480 V). During this cycle, the controller is able to track the current [Figs. 4.27(a) and 4.27(b)] and torque set-points [Fig. 4.26(a)]. As this is an intra-city cycle, only low speeds are observed, and, therefore, field weakening operation is not necessary [Fig. 4.24(b)]. The right side of Figs. 4.26 and 4.27 zoom in the dynamic response of the drive during the maximum torque command (130 Nm) of the cycle.

Next, the RWC1 driving cycle is applied again, but this time under variable dc-link voltage conditions. The results of this test are shown in Figs. 4.28 and 4.29. Once again, the electric drive provides the required torque during the trip while keeping the variable dc-link voltages balanced. In this instance, the plots on the right side present the detailed results when the machine operates at the maximum speed of the driving cycle. In particular, Fig. 4.28(b) shows how the balancing algorithm keeps the voltages balanced, although they change according to the actual operating point of the drive.

The third driving cycle is called Real World Driving Cycle 2 (RWC2[6]). This driving cycle combines different types of roads, such as urban, sub-urban flat, suburban with hill climbing, and highway in the surroundings of Turin, Italy. The features of this diving cycle are summarized in table 4.5. In general, this cycle considers high vehicle speeds. For instance, toward its end, the cycle reaches peak speed values just below 120 km/h, while, in its first part, the peak speeds are around 70 km/h. The traveled distance during the RWC2 driving cycle is more than 50 km, and it lasts 80 minutes.

---

[6]https://fitgen-project.eu/files/FITGEN_D1.1_Driving_cycles_specification_and_end-user_requirements_2019-05-23_FINAL.pdf
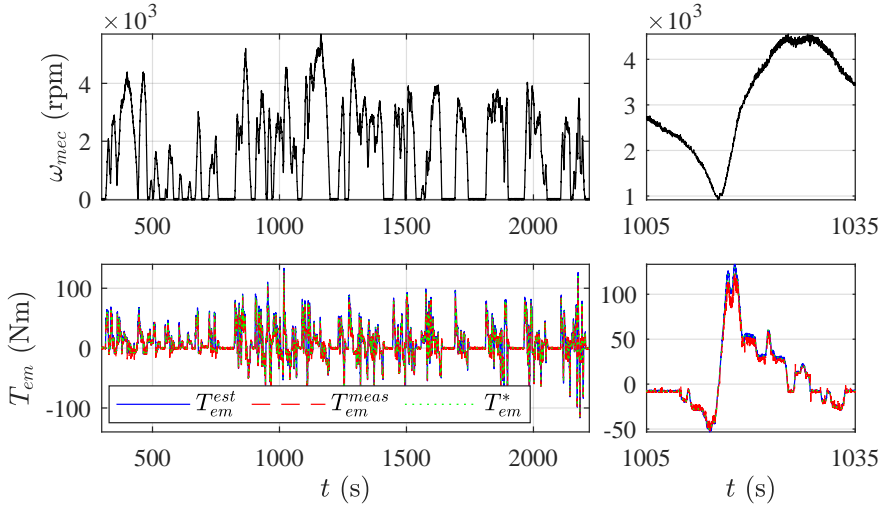
(a) Torque and speed.
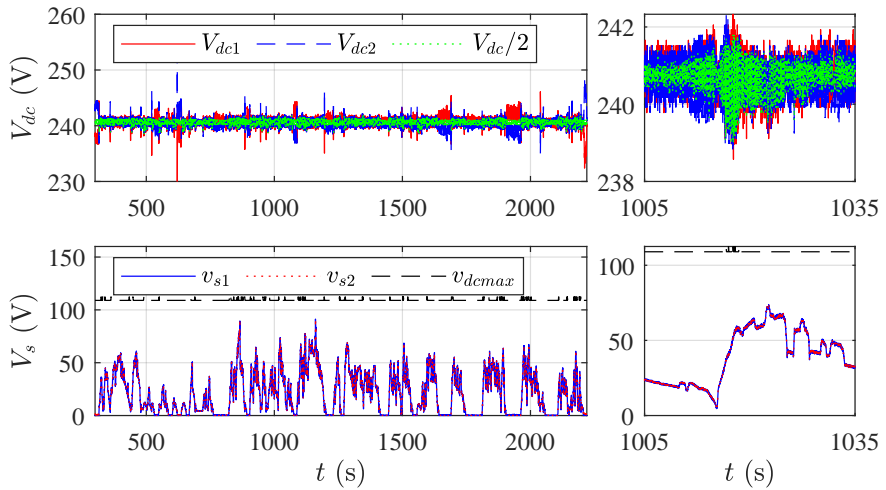
(b) Stator and dc-voltages.

Fig. 4.26: Experimental laboratory results obtained under the RWC1 driving cycle and fixed dc-link voltage (I).

(a) Set 1 $d-q$ stator currents.

(b) Set 2 $d-q$ stator currents.

Fig. 4.27: Experimental laboratory results obtained under the RWC1 driving cycle and fixed dc-link voltage (II).
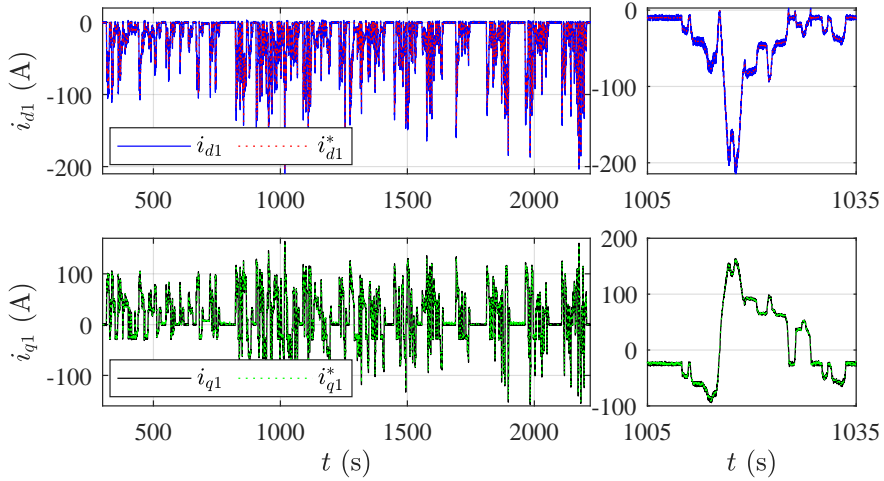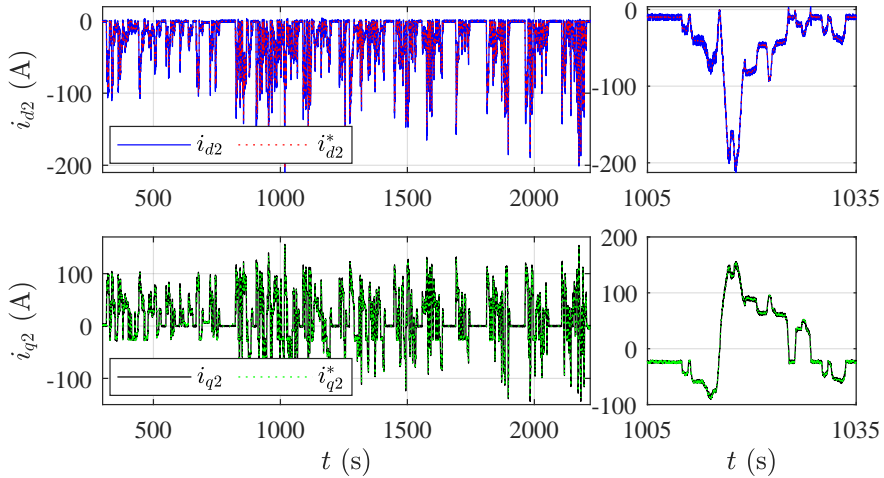
(a) Torque and speed.

(b) Stator and dc-voltages.

Fig. 4.28: Experimental laboratory results obtained under the RWC1 driving cycle and variable dc-link voltage (I).
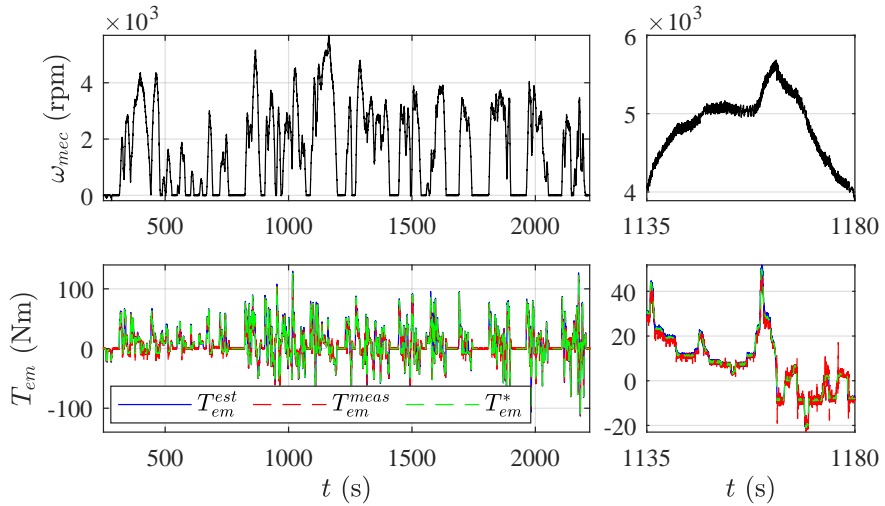
(a) Set 1 $d-q$ stator currents.

(b) Set 2 $d-q$ stator currents.

Fig. 4.29: Experimental laboratory results obtained under the RWC1 driving cycle and variable dc-link voltage (II).

Table 4.6: Summary of the main features of the US06 driving cycle.

Average speed	Medium	High	Extra-high	Total
Duration (s)	100	135	365	600
Standstill duration (s)	13	19	7	15.7
Distance (m)	1	2.5	12.2	23.27
% of time at standstill	13 %	14.1 %	1.9 %	6.5 %
Max speed (km/h)	101	138.6	157.5	157.5
Avg speed - stops (km/h)	40	77.9	122.9	100.8
Avg speed + stops (km/h)	34.7	66.9	120.6	94.2

Figs. 4.30 and 4.31 show the experimental results obtained under the RWC2 driving cycle and a variable dc-link voltage. During this long test, the electric drive response is stable and accurate. The zoomed-in charts depict the detailed response of the drive during the maximum speed of the RWC2 cycle. At this high speed, the dc/dc converter is commanded with the maximum dc-link voltage.

The last driving cycle used to test the proposal in the laboratory environment is the US06[7] or Supplemental Federal Test Procedure (SFTP). The US06 was developed to asses vehicle powertrains under high speed and high acceleration aggressive driving behavior. This cycle's duration is 10 minutes, and it travels a distance of 15.7 km at an average speed of 94.2 km/h. The main features of this driving cycle are summarized in table 4.6.

Figs. 4.32 and 4.33 illustrate the controller's response when the US06 cycle is emulated in the test bench. Despite the aggressive dynamics of this cycle, the drive generates the required torque while keeping the dc-link voltages balanced. As this driving schedule emulates high-speed routes, the electric machine operates more frequently in the FW region than in the previous cycles [Fig. 4.32(b)]. The right-side charts present a stretch of the US06 cycle at maximum speed, demonstrating accurate torque tracking during sharp torque commands, proper voltage balancing, and regulation of the stator voltages below the maximum admissible value [Figs. 4.32(a) and 4.32(b)].

Fig. 4.34 maps the tested driving cycle operating points and compares them to the rated torque-speed curve. This figure shows the ratio between vehicle and machine rotation speeds.

---

[7]https://www.epa.gov/vehicle-and-fuel-emissions-testing/dynamometer-drive-schedules
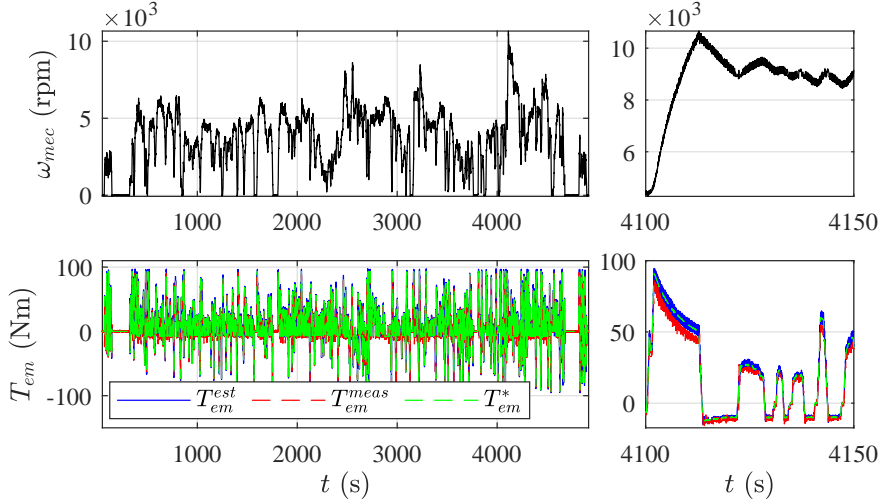
(a) Torque and speed.
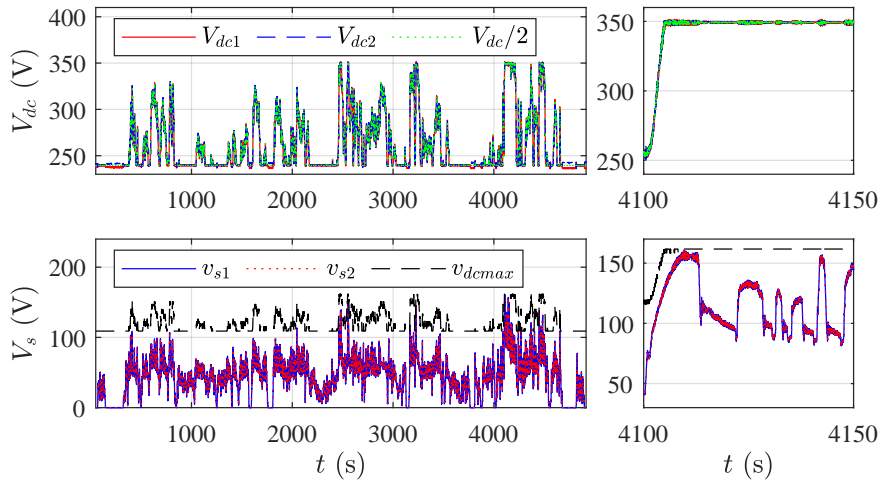
(b) Stator and dc-voltages.

Fig. 4.30: Experimental laboratory results obtained under the RWC2 driving cycle and variable dc-link voltage (I).

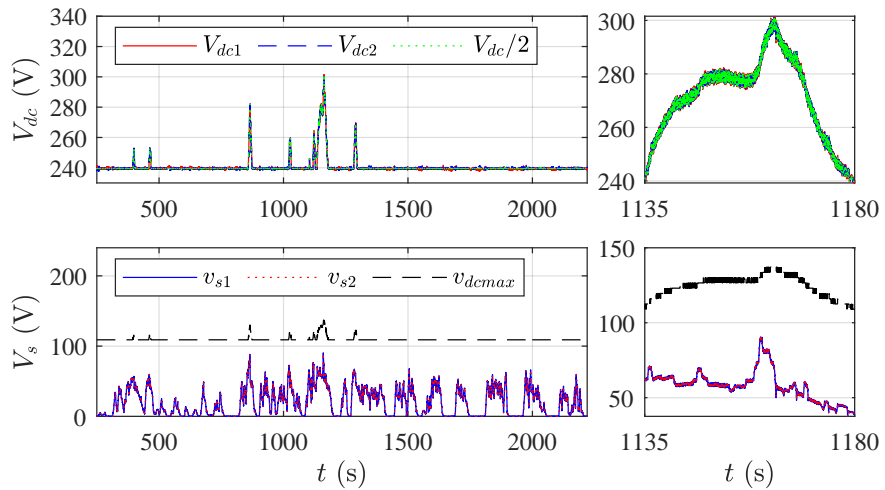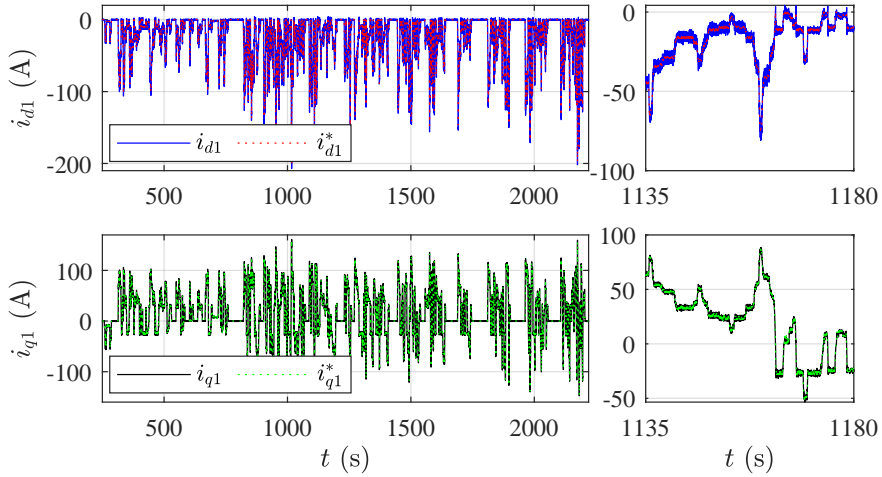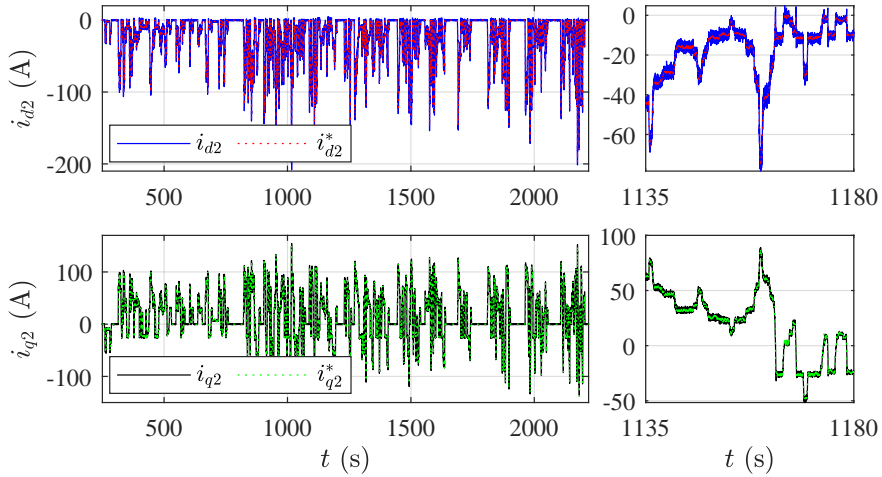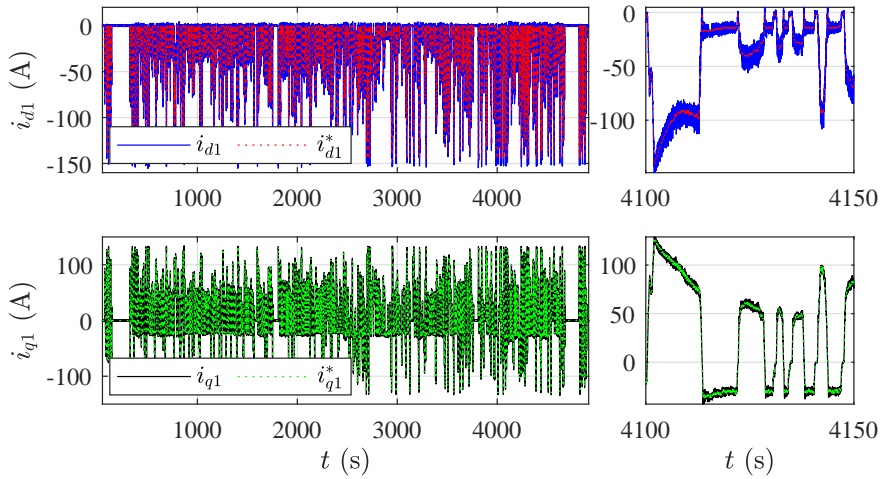(a) Set 1 $d - q$ stator currents.
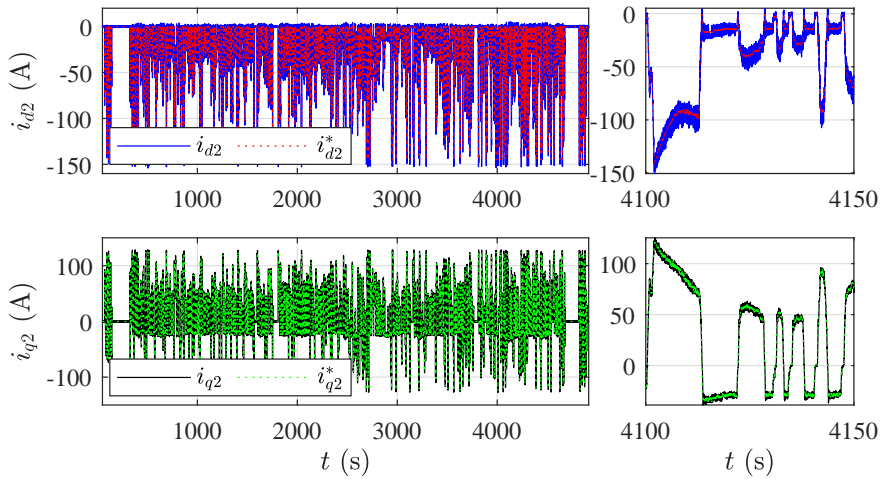
(b) Set 2 $d - q$ stator currents.

Fig. 4.31: Experimental laboratory results obtained under the RWC2 driving cycle and variable dc-link voltage (II).

(a) Torque and speed.
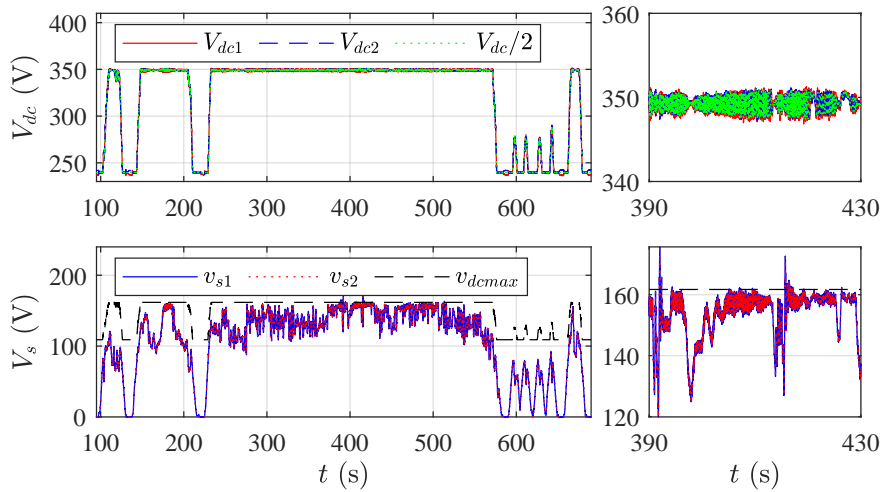
(b) Stator and dc-voltages.

Fig. 4.32: Experimental laboratory results obtained under the US06 driving cycle and variable dc-link voltage (I).
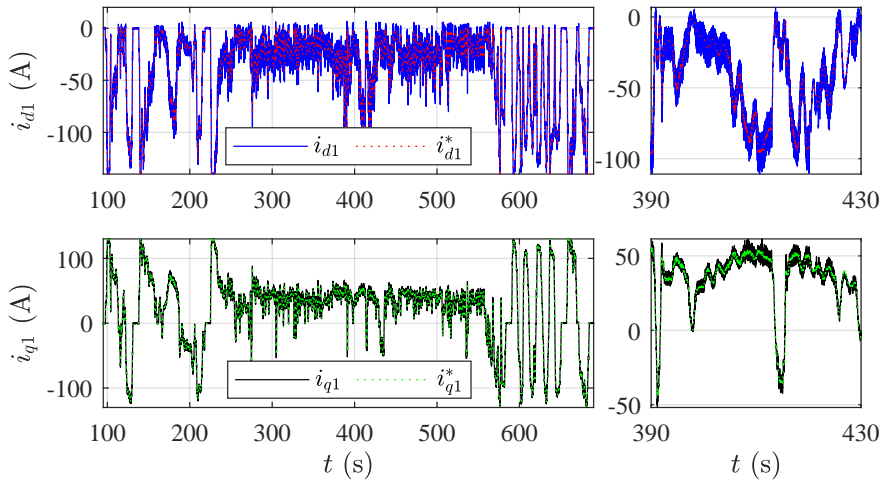
(a) Set 1 $d-q$ stator currents.
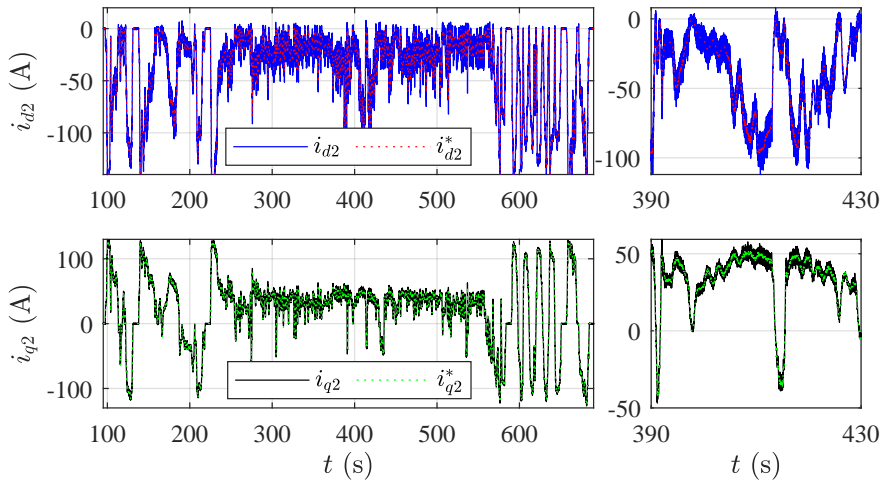
(b) Set 2 $d-q$ stator currents.

Fig. 4.33: Experimental laboratory results obtained under the US06 driving cycle and variable dc-link voltage (II).
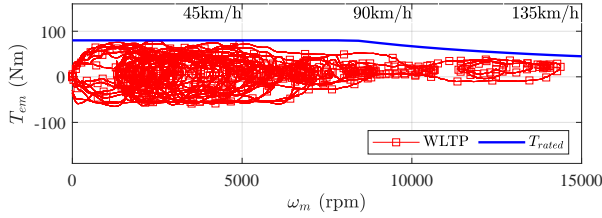
(a) WLTP.
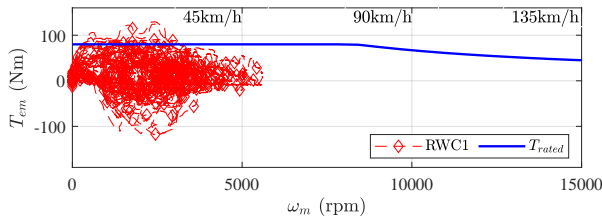
(b) RWC1.
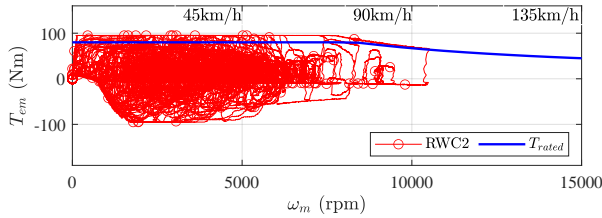
(c) RWC2.
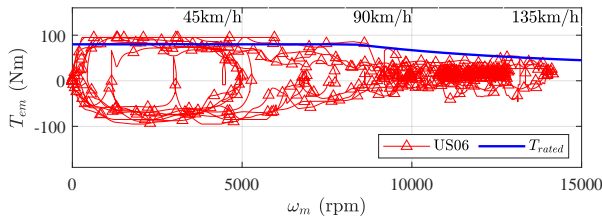
(d) US06.

Fig. 4.34: Comparison of the tested driving cycles operating points and the machine's rated torque-speed curve.

(a) Drive mounted

(b) Rear assembly

(c) Vehicle

Fig. 4.35: Electric vehicle used to carry out the verification of the proposed control approach under standardized driving cycles.

4.5.2 Experimental in-vehicle validation

Finally, the electric drive is integrated and validated in a real electric vehicle within the framework of the project FITGEN, led by the Centro Ricerche FIAT (CRF). In particular, the demonstration platform is a FIAT 500e[8], where the prototype is mounted on the rear axle. Tests are carried out both on-road and with the vehicle mounted over a dynamometer (Fig. 4.35). Therefore,

---

[8]https://www.fiat.com/500-electric/500-electric-hatchback/electric-features

the proposed control is validated at TRL-7 under realistic driving and harsh environmental conditions. The real industrial applicability of the proposal is demonstrated and represents a step forward to the commercial implementation of the proposed control technique.

Figs. 4.36 and 4.37 show the experimental results obtained when the vehicle, mounted on a dynamometer, is operated under the WLTP driving cycle. As shown in Fig. 4.36(a), the generated electromagnetic torque tracks the reference one satisfactorily. Note that, in-vehicle tests, there is no torquimeter. The performance of current regulators is shown in Fig. 4.37(a), where i_{d1} and i_{q1} currents of the first winding set track their references. Equivalent results are obtained for the second winding set [Fig. 4.37(b)]. These results again validate the adopted set-point generation approach and demonstrate the convenience of the used vector representation. Moreover, in this particular test, the drive operates with a variable dc-link voltage produced by the dc/dc converter. The voltages of the cascaded dc-link capacitors are again balanced for the whole trip thanks to the proposed balancing scheme [Fig. 4.36(b)]. Furthermore, during FW operation, the stator voltages of each three-phase set are kept below the safety limit.

The last test is carried out on-road, and Figs. 4.38 and 4.39 present the results. During this route, the vehicle covers a distance of 14.9 km at an average speed of 50.4 km/h. This cycle emulates the sub-urban scenario, where a maximum speed of about 100 km/h is reached, including several accelerations and deceleration phases. Again, all the obtained results are satisfactory. These on-road results demonstrate, at TRL-7, the accurate performance of the proposed torque controller for dual three-phase IPMSMs with voltage balancing capabilities.

In terms of efficiency and driving range, the e-axle exhibits a peak efficiency of 93.2 % (machine, inverter, and dc/dc combined), with a WLTP distance-specific energy consumption of 123 Wh/km, resulting in an overall efficiency of 75.6 %. In this context, a driving range of 321 km is obtained (i.e., 12×WLTP), with an average energy consumption of 39.6 kWh. Freeway constant speed driving tests exhibit a distance-specific energy consumption of 180 Wh/km at 110 km/h, and 224 Wh/km at 130 km/h, leading to a driving range of 210 km and 169 km, respectively, for a Usable Battery Energy (UBE) of 37.8 kWh. During rural driving conditions, the vehicle can travel a distance of 347 km at 70 km/h, with a distance-specific energy consumption of 109 Wh/km. Therefore, a freeway driving range from 840 to 1400 km with four battery charges is within reach, considering a speed range from 70 to 110 km/h, fulfilling the main objectives of the FITGEN project.
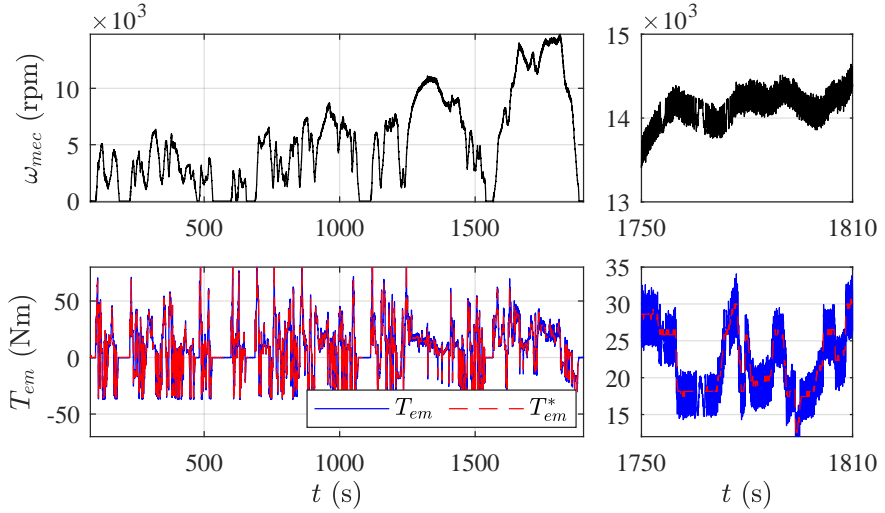
(a) Torque and speed.
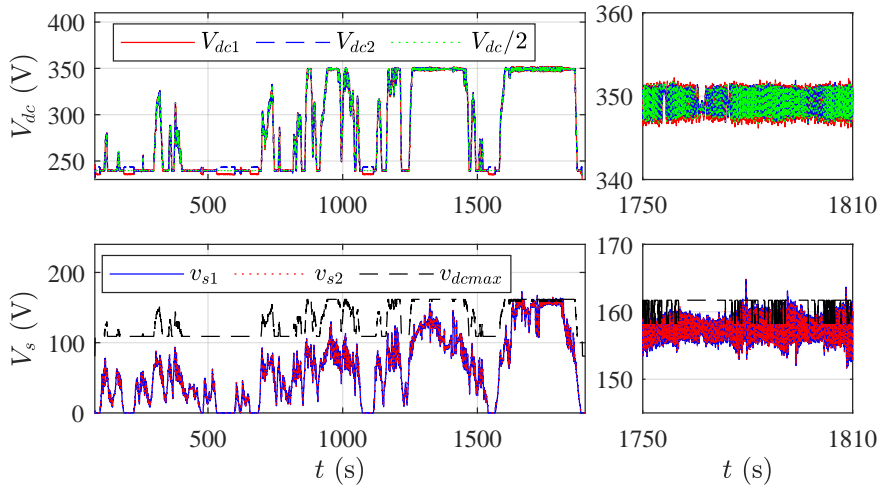
(b) Stator and dc-voltages.

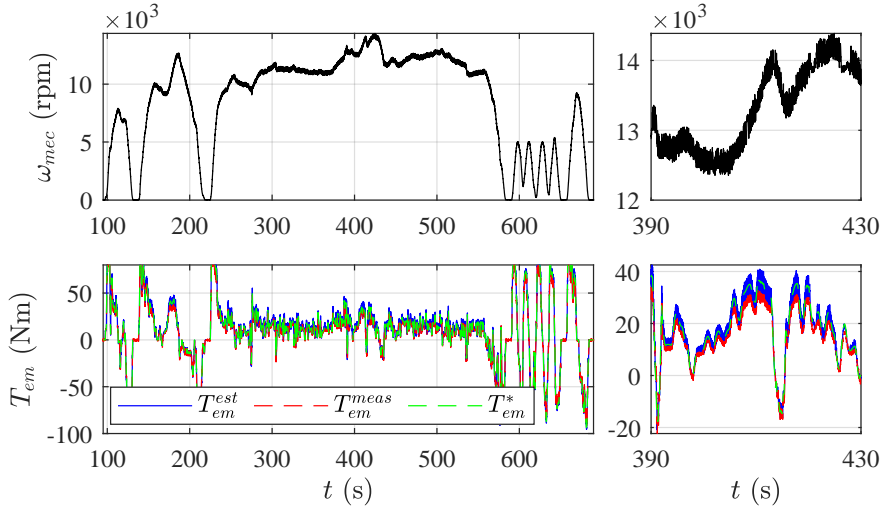Fig. 4.36: Experimental in-vehicle results obtained under the WLTP driving cycle (I).

164
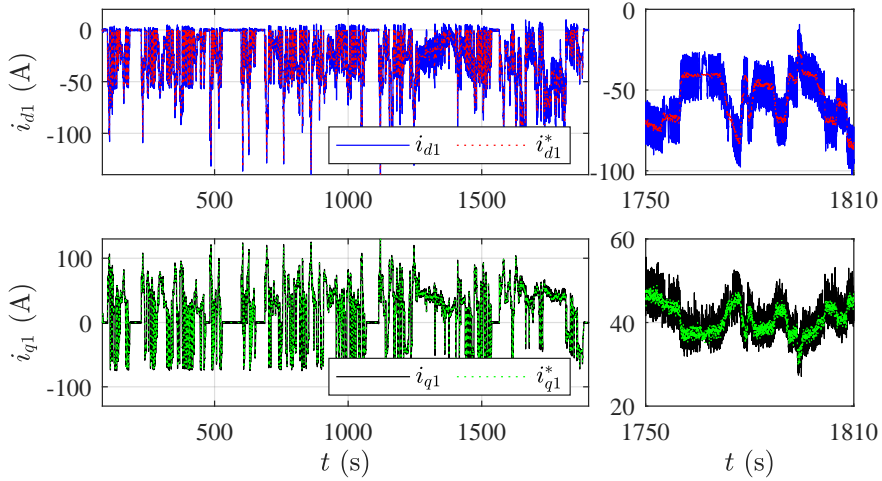
(a) Set 1 $d-q$ stator currents.
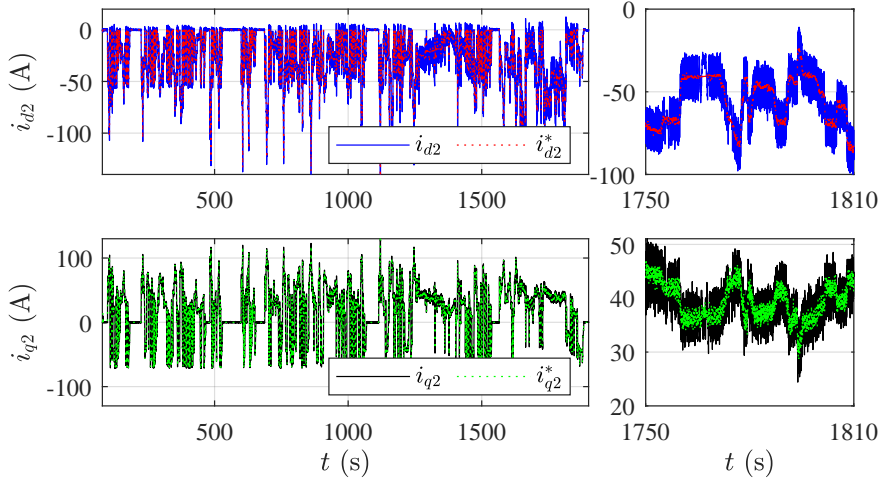
(b) Set 2 $d-q$ stator currents.

Fig. 4.37: Experimental in-vehicle results obtained under the WLTP driving cycle (II).
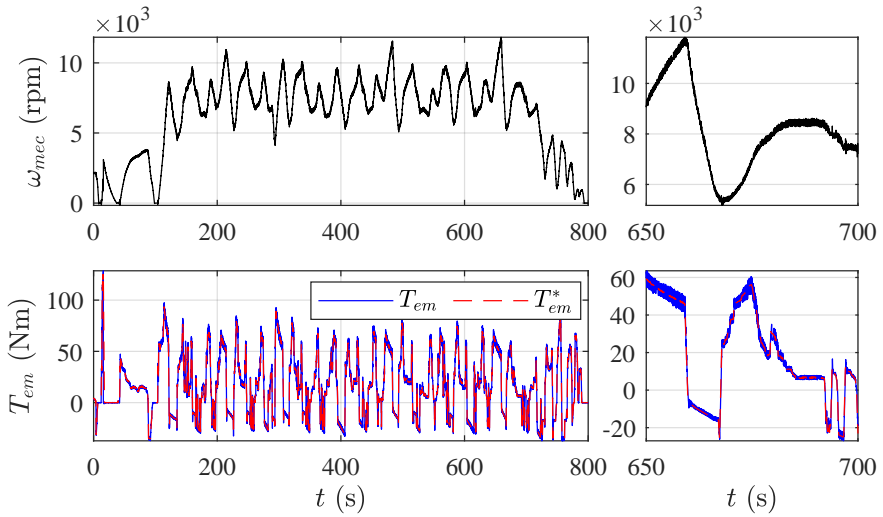
(a) Torque and speed.
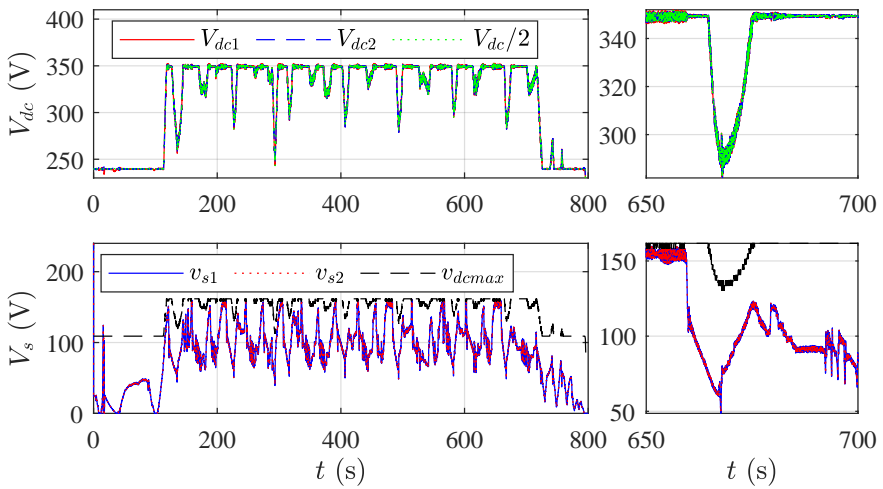
(b) Stator and dc-voltages.

Fig. 4.38: Experimental in-vehicle results obtained under on-road driving test (I).
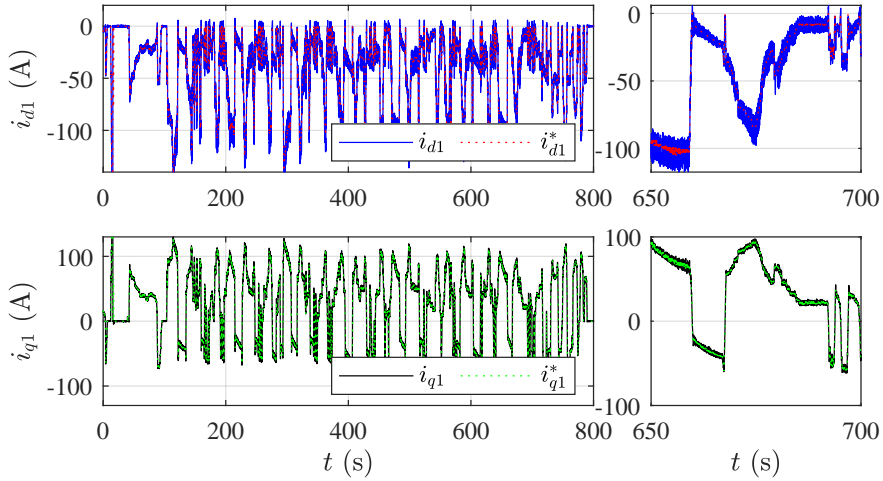
(a) Set 1 $d-q$ stator currents.
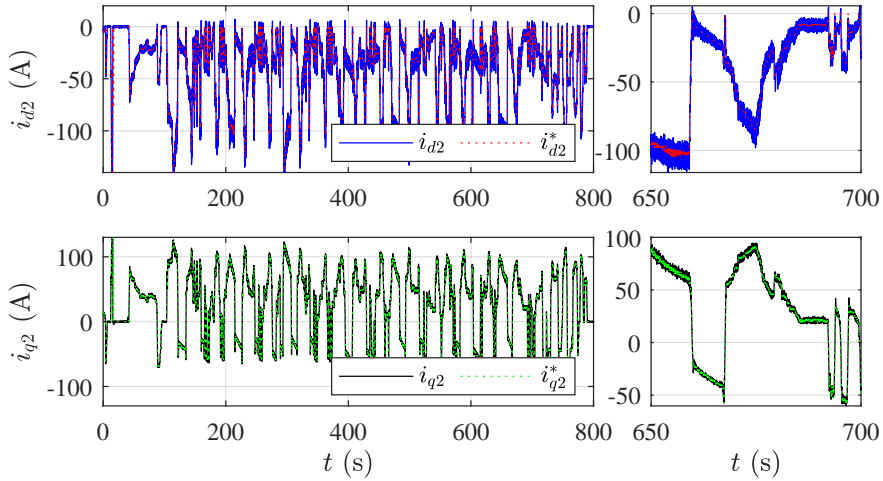
(b) Set 2 $d-q$ stator currents.

Fig. 4.39: Experimental in-vehicle results obtained under on-road driving test (II).

167

4.6 Conclusions

This chapter proposes a novel dc-link voltage balancing algorithm for automotive symmetrical dual three-phase IPMSM drives with a cascaded dc-link configuration, which regulates the q-axis current of each three-phase set, both in motoring and generation (regenerative braking) operation. In all the tested conditions, the balancing algorithm provides stable and reliable operation, correctly balancing the dc-link capacitor voltages without affecting or interfering with the performance of the machine's torque controller, neither in steady-state nor during transients. This aspect is crucial to make the cascaded dc-link configuration feasible to be implemented in future EV propulsion systems.

The vector regulation proposal, named *hybrid* torque controller, considers the inherent cross-coupling effects between the two three-phase sets. Thus, after conducting comprehensive theoretical and simulation analyses, this *hybrid* controller has been selected and combined with the balancing algorithm. This approach conveniently utilizes and takes advantage of two vector representations within the same vector controller, i.e., the *multiphase* ($\mathbf{T}_1$ matrix) and *double three-phase* ($\mathbf{T}_2$ matrix) representations. Thus, this vector control approach considers the voltage balancing requirements, making its integration straightforward and intuitive, and simultaneously meets the automotive requirements: torque control accuracy in the whole speed range, safe operation, and sufficiently low computational burden for automotive micro-controllers.

Using several driving cycles, the feasibility of the proposed control solutions has been demonstrated, at TRL-6, for the automotive scenario. The extensive laboratory testing allowed the fine-tuning of the control parameters. It proved the need to incorporate an interleaved PWM scheme to cancel high current ripple caused by overlapping the stator three-phase sets windings. Finally, a TRL-7 validation of the drive under test in a commercial EV platform has been completed. This way, the industrial applicability of the proposal is fully demonstrated, which can be of great interest to industrial engineers, researchers, OEMs, and vehicle manufacturers alike. To the best of the authors' knowledge, it is the first time that this type of cascaded dc-link configuration is successfully used for EV applications at full-scale level.

It is important to point out that although this control solution has been initially proposed for a symmetrical dual three-phase machine. However, the developed control solutions can be adapted and extended to asymmetrical dual three-phase machines or even to multiple three-phase machines by modifying the transformation matrices but keeping the general structure of the controllers.

Chapter 5

Conclusions and future work

5.1 Conclusions and summary of the most relevant contributions

In line with the state of the art, it can be concluded that multiphase systems are one of the most promising electric machine technologies for next-generation EV propulsion systems. When compared to standard three-phase technologies, multiphase machines offer higher torque and power density, reduced torque ripple, higher efficiency, higher reliability, and fault-tolerance. These features are relevant for future EVs to overcome key consumer performance barriers such as vehicles' driving range, safety, cost, and maneuverability, among other aspects. However, multiphase systems are more complex, and consequently, new software control systems are required. This leads to a broad research field on this topic.

Among multiphase technologies, the dual three-phase configuration is preferred as it allows a smooth transition from standard three-phase machines. Conventionally, within dual three-phase drives, the dc-link of each inverter unit is parallel connected to the battery pack. However, the incorporation of a dc/dc converter and a cascaded connected dc-link is gaining attention. Such configuration enables embedded super-fast charging capabilities, reduction of dc-link and power electronics components ratings and cost, minimization of overall system power losses, thanks to the incorporation of convenient control strategies,

reduction of current ripple, and increased power factor.

At the beginning of this thesis and as a set of secondary contributions, this work provides a comprehensive mathematical analysis regarding star-connected symmetrical PMSMs, in general, and dual three-phase IPMSMs, in particular.

As a first main contribution, this thesis proposes a novel *hybrid* vector torque control algorithm, which combines the utilization of the components from other two controllers within the same control scheme, i.e., the *multiphase* and *double three-phase* algorithms, to take advantage of both and overcome their weaknesses. This novel *hybrid* approach considers the inherent cross-coupling between the two three-phase sets while allowing uncomplicated power-sharing capabilities. The *hybrid* controller demonstrates to be superior with respect to the other control approaches when a cascaded dc-link architecture is considered. Simulation results showed that the proposed controller performs torque tracking more accurately than the other alternatives. Then, these preliminary results were corroborated during experimental tests, where a steady-state torque error (reference vs. actual, this last measured by a torquimeter) lower than 10 % was observed for all the torque/speed range of the drive. At the same time, the torque ripple was lower than 1 % thanks to the utilization of WBG semiconductors and high switching frequencies. The accuracy of the offline 2D-LUTs calculation algorithm was also demonstrated considering such figures, both for MTPA and field weakening. Additionally, the stator voltage vector modulus of each three-phase set was kept within the 10 % safety margin, demonstrating the correct performance of the FW algorithm that incorporates the speed normalization block and the VCT loop.

The second main contribution of this thesis is the proposal of a novel control system with dc-link voltage balancing capabilities for symmetrical dual three-phase IPMSMs. For this purpose, the controller incorporates a novel cascaded dc-link voltage balancing algorithm that regulates the q-axis current of each three-phase set, both in motoring and in generation (regenerative braking). To be able to perform the balancing tasks, it is mandatory to consider both operation modes, as regenerative braking permits to extend the driving range of the vehicle. This part of the controller takes advantage of the double three-phase representation of the machine and is crucial to make the cascaded dc-link configuration feasible for EV propulsion. Theoretical analysis, simulations, and experimental results show that input dc-voltages immediately become unbalanced, leading to a direct loss of control, which jeopardizes the integrity of the power system if the balancing algorithm were not active. Therefore, the incorporation of the balancing algorithm is mandatory to run all validation tests of the dual three-phase drive with cascaded dc-link configuration. Such tests in-

clude torque and speed steps, full speed range operation, sharp transient tests, such as torque and speed reversals, and driving cycles WLTP, US06, RWC1, and RWC2. First, the validation tests were performed under constant dc-link voltage. Then, an optimal variable dc-link voltage algorithm was incorporated. In all these scenarios, the controller proved to be able to keep the dc voltages balanced with a voltage ripple lower than 2%.

A third contribution of this doctoral research is the complete experimental verification of the proposal, not only in a laboratory test bench but also in a real electric vehicle under realistic driving and harsh environmental conditions. Tests have been carried out both on-road and with the vehicle mounted over a dynamometer. I.e., the solution is verified at TRL-7 in a real electric vehicle comprising an automotive 70 kW six-phase IPMSM drive and under realistic driving conditions. This way, the industrial applicability of the proposal is fully demonstrated, which can be of great interest to industrial engineers, researchers, OEMs, and vehicle manufacturers alike. Such TRL-7 validation of the e-axle proposed within project FITGEN, including the novel controller presented in this thesis, demonstrates the fulfillment of the project targets. Under WLTP driving conditions (urban and extra-urban), the distance range is 321 km with a distance-specific energy consumption of 123 Wh/km and 76 % of average efficiency. Under freeway driving conditions (110 km/h), the distance range is 210 km with a distance-specific energy consumption of 180 Wh/km. Finally, under rural driving conditions (70 km/h), the distance range is 347 km with a distance-specific energy consumption of 109 Wh/km. These results show that the control solution proposed successfully achieves the proper performance of the hardware of the electric drive (power converters and electric machine).

An additional contribution that is partially related to the content of this thesis is the development of a novel control solution for dual three-phase machines based on first-order sliding mode control techniques. This was developed within the framework of a scientific collaboration with researchers from the Universitat Politècnica de Catalunya. The proposed SMC controller incorporates the injection of triplen voltage harmonics, enhancing by 15 % the dc-link voltage utilization. Therefore, this controller matches the features of dc-voltage utilization of standard FOC + SVM controllers while improving the dynamic response of the current regulation loops. Initially, the first-order SMC was successfully validated through an experimental test bench based on a three-phase electric machine. The promising results of such preliminary validation allow proceeding in the future implementation of the SMC current regulation loops within the torque control of dual three-phase drives. Note that the incorporation of the SMC loops in the *hybrid* controller is relatively straightforward, as the *hybrid*

171

Table 5.1: Publications derived from this thesis and their correspondence with document chapters.

Chapter	Title	Publication
1	Introduction and contextualization	J5
2	Modeling of star-connected symmetrical multi-phase PMSMs	J4, C5, C7, C8, C9
3	Modeling and control of dual three-phase IPMSMs	J1, J3, C1, C6
4	Torque control of automotive dual three-phase IPMSM with a cascaded dc-link	J1, J2, C1, C2, C3
App. B	Sliding Mode Controller per three-phase set with harmonic injection capabilities	J3, C6

approach considers independent current regulation of each three-phase set.

5.2 Publications derived from this thesis

In the following, the publications related to the work carried out in this thesis are outlined. In this context, table 5.1 shows the correspondence between the thesis' chapters and the publications.

5.2.1 Publications in scientific journals

The following indexed (Journal Citation Reports, JCR) journal papers have been published, which are fully aligned with this thesis:

J1) **A. Sierra-Gonzalez**, P. Pescetto, F. Alvarez-Gonzalez, B. Heriz, E. Trancho, H. Lacher, E. Ibarra, G. Pellegrino, "*Full-speed range control of a symmetrical six-phase automotive IPMSM drive with a cascaded DC-link configuration*", IEEE Transactions on Industry Applications (ISSN: 0093-9994). Under review.

Ranking (2021): Q1 (Engineering, multidisciplinary 23/92).

Ranking (2021): Q2 (Engineering, electrical & electronic 83/276).

Journal Citations Reports (JCR) Impact Factor (2021): 4.198.

This paper presents the main contribution of this thesis, i.e., the novel hybrid vector controller for dual three-phase IPMSMs with dc voltage balancing capabilities. In this work, a cascaded dc-link configuration is considered for the power electronics of the electric drive. The article presents a mathematical model of this particular dc-link configuration, and a novel balancing scheme is proposed. Furthermore, experimental results in a variety of operational conditions are conducted, both in an experimental test bench and also in a real electric vehicle. The feasibility of the industrial utilization of the cascaded architecture and the proposed controller is verified this way.

J2) P. Pescetto, **A. Sierra-Gonzalez**, F. Alvarez-Gonzalez, H. Kapeller, E. Trancho, G. Pellegrino, "*Active Control of Variable DC-link for Maximum Efficiency of Traction Motor Drives*", IEEE Transactions on Industry Applications (ISSN: 0093-9994). Under review.

Ranking (2021): Q1 (Engineering, multidisciplinary 23/92).

Ranking (2021): Q2 (Engineering, electrical & electronic 83/276).

Journal Citations Reports (JCR) Impact Factor (2021): 4.198.

In this work, an active dc-link voltage control is proposed to minimize power losses within the electric drive by regulating a dc/dc converter placed between the battery pack and the cascaded dc-link bus. Thus, the hybrid vector controller proposed within this thesis deals with a dynamically changing variable dc-link voltage. In this paper, the novel electric machine controller is tested under such conditions. The experimental verification carried out in a full-scale test bench demonstrates the robustness and correct performance of the novel dual three-phase IPMSM control algorithm.

The aforementioned papers provide the latest results obtained within the FITGEN project, which concluded on September 30, 2022. Consequently, for the date on which the thesis was deposited, these works were under review for their consideration for future publication.

In addition, the content of the following indexed (JCR) papers is partially aligned with this thesis:

J3) V. Repecho, **A. Sierra-González**, E. Ibarra, D. Biel, A. Arias, "*Enhanced DC-link voltage utilization for sliding mode controlled PMSM drives*",

In this paper, a novel approach to incorporate third harmonic injection capabilities in PMSM drives controlled by using first-order SMC controllers is presented. The injection signals are generated from the control actions of the SMC. This new approach has been experimentally verified for a three-phase SM-PMSM drive. However, the incorporation of this scheme into the proposed hybrid vector controller is straightforward by substituting the PI-FOC blocks with the proposed two three-phase SMC controllers.

This work opens new research possibilities for fault-tolerant control of dual three-phase IPMSM drives that are considered in this thesis's future work section.

J4) M. Fernandez, **A. Sierra-González**, E. Robles, I. Kortabarria, E. Ibarra, J.L. Martin, "*New Modulation Technique to Mitigate Common Mode Voltage Effects in Star-Connected Five-Phase AC Drives*", Energies (ISSN: 1996-1073), vol. 13 (num. art. 607), pp. 1-19, 2020.

This article deals with the Common Mode Voltage (CMV) mitigation in multiphase (star-connected five-phase) PMSM drives. In particular, this work makes use of the simulation models developed within chapter 2 of this thesis.

Finally, the following paper has been published in a high-level science and technology dissemination journal, targeting both university students and specialists alike:

J5) **A. Sierra-González**, E. Ibarra, I. Kortabarria, J. Andreu, J. Lasa, "*Hegazkinen elektrifikazioa: aktuatzaile elektromekanikoak eta propultsio elektrikoa*"[1], Ekaia (ISSN 0214-9001), vol. 35, pp. 259-277, 2019.

---

[1]Aircraft electrification: electromechanical actuators and electric propulsion.

DOI: 10.1387/ekaia.19720.

In this work, the role of multiphase systems for transport electrification is reviewed from a science and technology dissemination perspective, mainly focusing on aerospace systems (electric propulsion and electromechanical actuators).

5.2.2 Conference publications

The following conference papers that are directly related to this thesis have been published in international forums:

C1) **A. Sierra-Gonzalez**, P. Peschetto, E. Trancho, E. Ibarra, G. Pellegrino, F. Alvarez-Gonzalez, "*Control of dual three-phase IPMSM drive with cascaded DC-link capacitors for third generation EV*", Proc. of the IEEE Energy Conversion Congress and Exposition (ECCE), ISBN: 978-1-7281-5135-9/21, pp. 4822-4829, Vancouver (Canada), 2021.

C2) P. Peschetto, **A. Sierra-Gonzalez**, E. Trancho, G. Pellegrino, F. Alvarez-Gonzalez, "*Variable dc-link control strategy for maximum efficiency of traction motor drives*", in Proc. of the IEEE Energy Conversion Congress and Exposition (ECCE), ISBN: 978-1-7281-5135-9/21, pp. 4815-4821, Vancouver (Canada), 2021.

C3) M. De Gennaro , J. H. Page, T. Wellerdieck, A. Lionetto, S. Herber, M. Abbenhaus, P. Pescetto, G. Pellegrino, A. Primon, P. A. Torres, **A. Sierra-Gonzalez**, F. Alvarez-Gonzalez, A. S. Koroma, D. Costa, "*Designing, prototyping, and testing an integrated e-axle for third-generation electric vehicles*", in Proc. of the Transport Research Arena 2022 (TRA), pp. 1-8, Lisbon (Portugal), 2022

On the other hand, the following national and international conference works are partially or indirectly related to the content of this thesis:

C4) A. R. Navarro, E. Ibarra, I. Kortabarria, **A. Sierra-Gonzalez**, B. Prieto, I. Elosegui, "*Normalised hybrid flux weakening strategy for automotive asymmetrical dual three-phase IPMSMs*", in Proc. of the Annual Conference of the Industrial Electronics Society (IECON), pp. 1-6, Brussels (Belgium), 2022.

C5) **A. Sierra-Gonzalez**, E. Ibarra, I. Kortabarria, E. Trancho, E. Otaola, "*Real-time simulation platform of an EMA landing gear*", in Proc. of the International Conference on Power Electronics, Machines and Drives (PEMD), ISBN: 978-1-83953-542-0, pp. 62-67, Nottingham (United Kingdom), 2020.

C6) V. Repecho, **A. Sierra-Gonzalez**, E. Ibarra, D. Biel, A. Arias, "*Control deslizante de máquinas síncronas de imanes permanentes para aplicaciones de electromovilidad*"[2], in Proc of Seminario Anual de Automática, Electrónica Industrial e Instrumentación (SAAEI), ISBN 978-84-122260-2-7, pp. 486-491, Ciudad Real (Spain), 2020.

C7) **A. Sierra-Gonzalez**, E. Ibarra, I. Kortabarria, J.I. Gárate, I. Eguizabal, "*Control vectorial de BLDC multifase para propulsión eléctrica en aplicaciones aeronáuticas*"[3], in Proc. of Seminario Anual de Automática, Electrónica Industrial e Instrumentación (SAAEI), ISBN: 978-84-17171-50-6, pp. 78-83, Cordoba (Spain), 2019.

C8) **A. Sierra-Gonzalez**, E. Ibarra, I. Kortabarria, I. Martínez de Alegría, E. Otaola, "*Modelado y simulación de tren de aterrizaje basado en actuador electromecánico con PMSM multifase*"[4], in proc. of Seminario Anual de Automática, Electrónica Industrial e Instrumentación (SAAEI), ISBN: 978-84-17171-50-6, pp. 72-77, Cordoba (Spain), 2019.

C9) **A. Sierra-Gonzalez**, E. Ibarra, I. Kortabarria, J. Andreu, J. Lasa, "*Evaluation of the intrinsic fault tolerance of an EMA landing gear based on a five-phase SM-PMSM*", in Proc. of More Electric Aircraft 2019 (MEA), pp. 1-4, Toulouse (France), 2019.

5.3   Future work

Considering the work carried out in this thesis, the author proposes the following research lines for future investigation:

---

[2]Sliding mode control for permanent magnet synchronous machines applied to transport electrification.

[3]Vector control for multiphase BLDC applied to aeronautic electric propulsion.

[4]Modeling and simulation of a landing gear based on a multiphase PMSM electromechanical actuator.

Migration of the developed technologies to aerospace applications

Currently and apart from EV applications, the Clean Powertrain group of Fundación Tecnalia Research and Innovation is incorporating new research activities focused on aerospace systems.

The multiphase configurations and the control solutions investigated in this thesis are appropriate for the aerospace context, as multiphase drives provide some level of intrinsic fault tolerance, improving safety and availability. Thus, the investigation of control solutions for dual three-phase machines (with or without cascaded dc-link configuration) is proposed considering both propelling and electromechanical actuation applications, particularizing the proposed solutions to the aircraft scenario.

Non-linear controllers for balancing the cascaded dc-link voltage

As demonstrated in chapter 4, the behavior of the dc-link voltages is not linear, and electrical parameters vary according to the operation point. Experimental and FEM data shows variations of more than 50% in the parameters of the dc-link model within some points of the full speed and torque range. Therefore, it is expected that the utilization of non-linear control techniques such as SMC, feedback-linearization, or gain-scheduling will allow improving the performance of the voltage balancing. Thus, it is proposed to investigate about advanced non-linear control techniques for the voltage balancing of dual three-phase IPMSMs with cascaded dc-link.

Fault tolerant control of dual three-phase IPMSM drives

As stated before, the SMC approach, including voltage injection capabilities, proposed during the collaboration with researchers of the Universitat Politècnica de Catalunya, can be directly incorporated into the novel *hybrid* vector controller for dual three-phase drives proposed in this thesis. This type of non-linear controller has sufficient dynamic response to follow fast-changing current set-points, which are common in post-fault regulation. In this context and in general, PI controllers do not have enough bandwidth to synthesize such references properly.

Considering the previous, it is proposed to investigate the development and implementation of a fault-tolerant controller based on SMC for the dual three-phase IPMSM with a cascaded configuration. This type of solution can be of great interest to both the automotive and the aerospace industry.

Fault tolerant control of star-connected multiphase PMSM drives

Similar to the previous point, using the knowledge acquired during the confection of chapter 2, the SMC controller can be adapted for star-connected multiphase PMSM drives, in general, and five-phase PMSMs, in particular. This could be of special interest for machines with a concentrated winding distribution, taking advantage of the harmonics in the back-EMF to increase torque density and following complex and fast current references for fault-tolerant operation.

Currently, there is a 5 kW five-phase PMSM prototype available at Tecnalia's facilities to start this new research line.

5.4 Acknowledgments

---

[5]Distributed advanced control for safety and energy efficiency of air transport.

Date: 2018-07-01 to 2019-12-31.

URL: https://www.spri.eus/es/ayudas/elkartek/

GRANT NUMBER: KK-2018/00082

Funded by: Basque Country Government (Vitoria, Spain).

P4) VEGAN (*Vehículo Eléctrico Basado en Gallium Nitride*)[6]

Date: 2021-07-01 to 2022-12-31.

URL: https://www.spri.eus/es/ayudas/elkartek/

GRANT NUMBER:KK-2021/00044

Funded by: Basque Country Government (Vitoria, Spain).

---

[6]Electric vehicle based on Gallium Nitride.

Appendix A

Voltage vector saturation

Herein, three voltage vector saturation algorithms are described for PMSM FOC controllers. The first one is known as the angle priority limiter, which is calculated as follows:

$$\text{if} \quad \sqrt{v_d^{*2} + v_q^{*2}} > v_{max}$$

$$v_{dlim}^* = v_d^* \frac{v_{max}}{\sqrt{v_d^{*2} + v_q^{*2}}} \quad \text{and} \quad v_{qlim}^* = v_q^* \frac{v_{max}}{\sqrt{v_d^{*2} + v_q^{*2}}}, \tag{A.1}$$

$$\text{else}$$

$$v_{dlim}^* = v_d^* \quad \text{and} \quad v_{qlim}^* = v_q^*,$$

where the angle of the voltage vector is invariant (Fig. A.1).

The second limiter is the one known as the d-axis voltage priority. In this case, if the reference magnitude is greater than the voltage constraint, the voltage is limited as follows:

$$\text{If} \quad |v_d^*| < v_{max}$$

$$v_{dlim}^* = v_d^*$$

$$\text{Else} \tag{A.2}$$

$$v_{dlim}^* = sign(v_d^*)v_{max},$$

where the q-axis component is $v_{qlim}^* = sign(v_q^*)\sqrt{v_{max}^2 - v_d^{*2}}$.

The last limiter is known as the q-axis voltage priority. In this case, the

voltage is limited as follows:

$$
\begin{aligned}
&\text{If} \quad |v_q^*| < v_{max} \\
&\qquad v_{qlim}^* = v_q^* \\
&\text{Else} \\
&\qquad v_{qlim}^* = sign(v_q^*)v_{max}.
\end{aligned}
\tag{A.3}
$$

where the d-axis component is $v_{dlim}^* = sign(v_d^*)\sqrt{v_{max}^2 - v_q^{*2}}$.

Fig. A.1 illustrates the differences between the three limiters described above. If d-axis priority is chosen, an improved d-axis current response is expected during voltage saturation, and FW operation [161]. If q-axis priority is selected, a fast dynamic torque response is expected. Finally, if the angle priority is chosen, a trade-off between the two previous options is achieved.
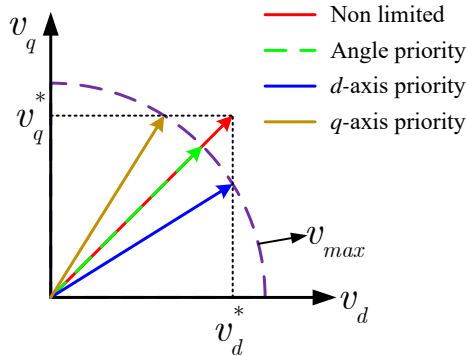
Fig. A.1: Comparison of the three described voltage limiters.

In particular, the FOC algorithms implemented in this thesis incorporate the angle priority limiter approach. Note that the limiter is an additional safety feature, which is not expected to act because the VCT loop must keep the stator voltages within the safety margin.

Appendix B

Sliding Mode Controller per three-phase set with harmonic injection capabilities

B.1 Operation principles of the SMC controller

SMC is a robust control technique against electrical parameter variations and uncertainties. At the same time, it provides fast transient response [162, 163], making it specially suitable for the implementation of fault-tolerant controllers in dual three-phase drives.

Fig. B.1 shows the general diagram of the proposed SMC controller, per a three-phase set, in the dq reference frame. This regulator aims to control the currents i_j ($j = \{a, b, c\}$) and, at the same time, the average voltage of the neutral point v_n. Thus, two of these three-phase regulation blocks should substitute the PI-FOC blocks of the *hybrid* controller proposed in chapter 3.

Considering general automotive operational requirements, SMC applied to EVs should take into account the following aspects:

- One of the main drawbacks of first-order SMC is that, in principle, it operates with variable switching frequency. However, it is possible to fix
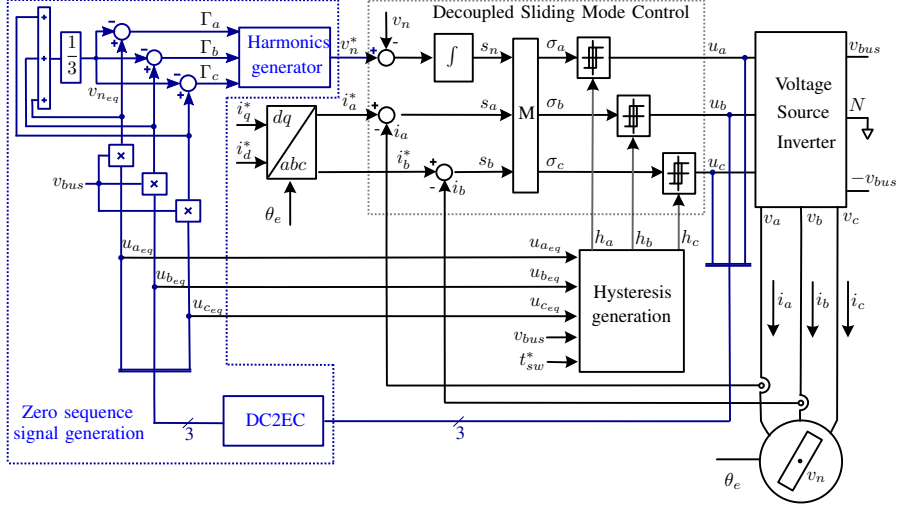
Fig. B.1: SMC block for a three-phase set, including harmonic injection, for a vector-controlled PMSM.

- such frequency by incorporating the dynamic hysteresis bands (hysteresis generation block) shown in Fig. B.1 and proposed in [164].

- As discussed in chapter 3, harmonic injection capabilities are required to extend the MTPA operation range of the drive as much as possible. This new proposal incorporates this feature into the non-linear controller.

- The VCT controller of chapter 3 requires the estimation of the modulus of the output voltage vector of each three-phase set, which is not directly provided by the SMC regulator.

The implemented SMC must take all these aspects into account.

The operation principles of the controller are as follows. In order to carry out a decoupled sliding mode current control, the sliding surface matrix **S** that will guarantee zero tracking error must be selected [165]. As in a star-connected three-phase set, only two of the currents are linearly independent; it is sufficient to control two out of three currents. This way, a remaining degree of freedom is

available to regulate the average value of v_n. This additional degree of freedom is used to generate harmonic injection.

Accordingly, the switching functions are defined as follows:

$$\mathbf{S} = \left[i_a^* - i_a, \ i_b^* - i_b, \ \int \left(v_n^* - v_n \right) dt \right]^T .$$ (B.1)

In order to design the control laws guaranteeing asymptotic convergence to the desired steady-state, a new set of sliding surfaces $\boldsymbol{\sigma} = \mathbf{MS}$ are defined. Neglecting the effects of saliency, magnetic saturation, and cross-coupling, the decoupling matrix $\mathbf{M}$ (Fig. B.1) that ensures the control decoupling [164], results in:

$$\mathbf{M} = \begin{bmatrix} L_a & 0 & 1 \\ 0 & L_b & 1 \\ -L_c & -L_c & 1 \end{bmatrix},$$ (B.2)

where L_a, L_b and L_c are the per-phase average inductances. As demonstrated in [166], not considering the aforementioned effects affect the performance of the decoupling. I.e., under loss of decoupling, the slopes of the switching functions are not perfectly triangular. However, the controller is able to regulate the electric machine while such effects are not very high. For the latter, (B.2) should be reformulated considering all these machine phenomena. This leads to an open future research line.

The following control law assures convergence to a vicinity of the zero value of the switching surfaces [164]:

$$u_x \begin{cases} -1 & \text{if} \quad \sigma_x < -h_x, \\ 1 & \text{if} \quad \sigma_x > h_x, \end{cases} \quad x \in \{a, b, c\} ,$$ (B.3)

where h_x is the hysteresis band of each controller. The hysteresis band generator (Fig. B.1) adjusts the hysteresis bands of the comparators to achieve fixed switching frequency operation [164].

B.2 Zero sequence signal generation under sliding mode

The block named Harmonics Generator (Fig. B.1) provides the reference signal v_n^* to be tracked by v_n in order to carry out voltage harmonics injection. As defined in chapter 3, in a FOC-PMSM scheme, the voltage injection is performed by applying a min-max algorithm or similar techniques. In all these cases, the

third harmonic signal is generated using the sinusoidal reference voltages v_a^*, v_b^*, and v_c^*. The SMC does not generate such voltages since it directly provides discontinuous control signals to the inverter. However, the equivalent controls can be determined for generating v_n^*.

From the SMC theory [165], the equivalent controls can be analytically determined by applying $\boldsymbol{\sigma} = 0$ and $\dot{\boldsymbol{\sigma}} = 0$. Hence, using $\boldsymbol{M}\dot{\boldsymbol{S}} = 0$, one gets:

$$u_{xeq} = \frac{1}{v_{bus}}(L_x \dot{i}_x^* + R_s i_x^* + e_x + v_n^*), \quad x \in \{a, b, c\}. \tag{B.4}$$

Knowing that when the neutral point is regulated to zero ($v_n^* = 0$), the equivalent control is sinusoidal, and the fundamental harmonic of the control can be identified in (B.4) as:

$$\Gamma_x = v_{bus} u_{xeq} - v_n^*, \quad x \in \{a, b, c\}. \tag{B.5}$$

When the reference v_n^* is not zero, under sliding motion, the equivalent controls are no longer purely sinusoidal, since v_n tracks v_n^* in average under sliding motion, see (B.1). However, the injection algorithm needs three purely sinusoidal signals to generate the zero sequence signals properly. Therefore, when $v_n^* \neq 0$, it is required to recover the Γ_x signals and use them for the zero sequence generation. Note that Γ_x could be determined from (B.5), but this procedure needs to know the v_n^* signal, which in turn is the output of the injection algorithm. To overcome this problem, the Γ_x signals are calculated using the following expression:

$$\Gamma_x = v_{bus} u_{xeq} - v_{n_{eq}}, \quad x \in \{a, b, c\}, \tag{B.6}$$

which corresponds to (B.5) replacing v_n^* by the averaged value of v_n, $v_{n_{eq}}$. Assuming that the stator windings are sinusoidally distributed along the stator, v_n can be calculated as:

$$v_n = \frac{v_{bus}}{3}(u_a + u_b + u_c), \tag{B.7}$$

, which is inherently discontinuous. Therefore, the averaged value of v_n can be approximated as

$$v_{n_{eq}} = \frac{v_{bus}}{3}\left(u_{a_{eq}} + u_{b_{eq}} + u_{c_{eq}}\right). \tag{B.8}$$

Finally, the equivalent controls of (B.6) are determined by low pass filtering the corresponding discontinuous control signals.
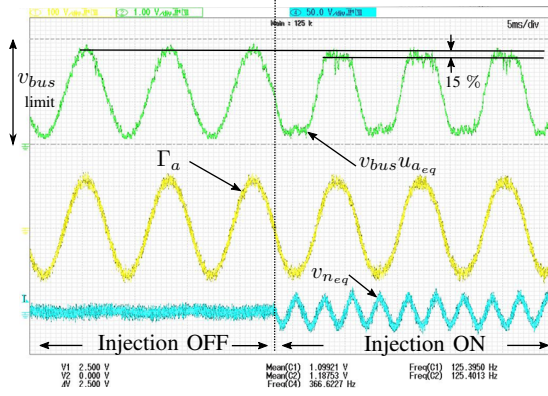
Fig. B.2: Harmonics injection in a three-phase PMSM (experimental results), improving the dc-link voltage utilization by 15 %.

Fig. B.1 shows the scheme used to generate the reference signal v_n^*. Firstly, the equivalent controls and $v_{n_{eq}}$ are obtained from the control signals. Subsequently, the Γ_x signals are derived applying (B.6) and, finally, knowing the bus voltage value, the reference signal v_n^* can be calculated by applying the min-max technique (Fig. B.2).

B.3 Field weakening control algorithm integration in the SMC

The field weakening controller requires the modulus of V_s to provide it as feedback to the VCT controller. As the equivalent controls are already determined for harmonics injection, the calculation of the voltage modulus in a three-phase system is straightforward:

$$V_s = \frac{2}{3}\sqrt{u_{a_{eq}}^2 + u_{b_{eq}}^2 + u_{c_{eq}}^2 - \Delta_{ueq}}, \tag{B.9}$$

where $\Delta_{ueq} = u_{a_{eq}}u_{b_{eq}} + u_{a_{eq}}u_{c_{eq}} + u_{b_{eq}}u_{c_{eq}}$.

This way, not only voltage harmonics injection capabilities but also robust field weakening control are provided to the drive (Fig. B.1).

Appendix B

Bibliography

[1] R. Bojoi, S. Rubino, A. Tenconi, and S. Vaschetto, "Multiphase electrical machines and drives: A viable solution for energy generation and transportation electrification," in *Proc. of the International Conference and Exposition on Electrical and Power Engineering (EPE)*, 2016. 13, 35, 36, 37, 63

[2] Y. Sui, P. Zheng, Y. Fan, and J. Zhao, "Research on the vector control strategy of five-phase permanent-magnet synchronous machine based on third-harmonic current injection," in *2017 IEEE International Electric Machines and Drives Conference (IEMDC)*. IEEE, may 2017, pp. 1–8. 17, 36, 67

[3] Z. Y. Gu, K. Wang, Z. Q. Zhu, Z. Z. Wu, C. Liu, and R. W. Cao, "Torque improvement in five-phase unequal tooth SPM machine by injecting third harmonic current," *IEEE Transactions on Vehicular Technology*, vol. 67, no. 1, pp. 206–215, Jan 2018. 17, 35, 36, 49, 67

[4] R. K. Pachauri, "Climate change 2014 synthesis report," IPCC, Tech. Rep., 2014. 33

[5] IEA. (2019) Global CO2 emissions by sector. [Online]. Available: https://www.iea.org/data-and-statistics/charts/global-co2-emissions-by-sector-2019 33, 34

[6] D. Ivanova, J. Barrett, D. Wiedenhofer, B. Macura, M. Callagham, and F. Creutzig, "Quantifying the potential for climate change mitigation of consumption options," *Environmental Research Letters*, vol. 15, no. 9, pp. 1–19, 2020. 34

[7] I. López, E. Ibarra, A. Matallana, J. Andreu, and I. Kortabarria, "Next generation electric drives for HEV/EV propulsion systems: Technology, trends and challenges," *Renewable and Sustainable Energy Reviews*, vol. 114(109336), pp. 1–23, 2019. 34, 35

[8] European Commission, Joint Research Centre, A. Tsakalidis, K. Gkoumas, M. Balen, F. Marques dos Santos, M. Grosso, A. Ortega Hortelano, and F. Pekár, *Research and innovation in transport electrification in Europe : an assessment based on the Transport Research and Innovation Monitoring and Information System (TRIMIS)*. Publications Office, 2020. 34

[9] A. Matallana, E. Ibarra, I. López, J. Andreu, J. Garate, X. Jorda, and J. Rebollo, "Power module electronics in HEV/EV applications: New trends in widebandgap semiconductor technologies," *Renewable and Sustainable Energy Reviews*, vol. 113, pp. 1–33, 2019. 34, 35, 37, 73

[10] Z. Li, A. Khajepour, and J. Song, "A comprehensive review of the key technologies for pure electric vehicles," *Energy*, vol. 182, pp. 824–839, 2019. 34

[11] A. S. Abdelrahman, Z. Erdem, Y. Attia, and M. Z. Youssef, "Wide bandgap devices in electric vehicle converters: A performance survey," *Canadian Journal of Electrical and Computer Engineering*, vol. 41, no. 1, pp. 45–54, 2018. 35

[12] T. Van Do, J. P. F. Trovão, K. Li, and L. Boulon, "Wide-bandgap power semiconductors for electric vehicle systems: Challenges and trends," *IEEE Vehicular Technology Magazine*, vol. 16, no. 4, pp. 89–98, 2021. 35

[13] A. K. Morya, M. C. Gardner, B. Anvari, L. Liu, A. G. Yepes, J. Doval-Gandoy, and H. A. Toliyat, "Wide bandgap devices in AC electric drives: Opportunities and challenges," *IEEE Transactions on Transportation Electrification*, vol. 5, no. 1, pp. 3–20, 2019. 35

[14] I. Husain, B. Ozpineci, M. S. Islam, E. Gurpinar, G.-J. Su, W. Yu, S. Chowdhury, L. Xue, D. Rahman, and R. Sahu, "Electric drive technology trends, challenges, and opportunities for future electric vehicles," *Proceedings of the IEEE*, vol. 109, no. 6, pp. 1039–1059, 2021. 35

[15] A. Tüysüz, F. Meyer, M. Steichen, C. Zwyssig, and J. W. Kolar, "Advanced cooling methods for high-speed electrical machines," *IEEE Transactions on Industry Applications*, vol. 53, no. 3, pp. 2077–2087, 2017. 35

[16] H. Behi, D. Karimi, R. Youssef, M. Suresh Patil, J. Van Mierlo, and M. Berecibar, "Comprehensive passive thermal management systems for electric vehicles," *Energies*, vol. 14, no. 13, 2021. 35

[17] D. Fodorean, L. Idoumghar, M. Brevilliers, P. Minciunescu, and C. Irima, "Hybrid differential evolution algorithm employed for the optimum design of a high-speed PMSM used for EV propulsion," *IEEE Transactions on Industrial Electronics*, vol. 64, no. 12, pp. 9824–9833, 2017. 35

[18] D. Gerada, A. Mebarki, N. L. Brown, C. Gerada, A. Cavagnino, and A. Boglietti, "High-speed electrical machines: Technologies, trends, and developments," *IEEE Transactions on Industrial Electronics*, vol. 61, no. 6, pp. 2946–2959, 2014. 35

[19] F. Savi, D. Barater, M. D. Nardo, M. Degano, C. Gerada, P. Wheeler, and G. Buticchi, "High-speed electric drives: a step towards system design," *IEEE Open Journal of the Industrial Electronics Society*, vol. 1, pp. 10–21, 2020. 35

[20] E. Trancho, E. Ibarra, A. Arias, I. Kortabarria, J. Jurgens, L. Marengo, and A. Fricasse, "PM-assisted synchronous reluctance machine flux weakening control for EV and HEV applications," *IEEE Transactions on Industrial Electronics*, vol. 65, no. 4, pp. 2986–2995, 2018. 35, 86, 87

[21] J.-R. Riba, C. López-Torres, L. Romeral, and A. Garcia, "Rare-earth-free propulsion motors for electric vehicles: A technology review," *Renewable and Sustainable Energy Reviews*, vol. 57, pp. 367–379, 2016. 35

[22] B. Poudel, E. Amiri, P. Rastgoufard, and B. Mirafzal, "Toward less rare-earth permanent magnet in electric machines: A review," *IEEE Transactions on Magnetics*, vol. 57, no. 9, pp. 1–19, 2021. 35

[23] I. Boldea, L. Tutelea, L. Parsa, and D. Dorrell, "Automotive electric propulsion systems with reduced or no permanent magnets: an overview," *IEEE Transactions on Industrial Electronics*, vol. 61, no. 10, pp. 5696–56 711, 2014. 35

[24] E. Levi, "Advances in converter control and innovative exploitation of additional degrees of freedom for multiphase machines," *IEEE Transactions on Industrial Electronics*, vol. 63, no. 1, pp. 433–448, jan 2016. 35

[25] F. Betin, G.-A. Capolino, D. Casadei, B. Kawkabani, R. I. Bojoi, L. Harnefors, E. Levi, L. Parsa, and B. Fahimi, "Trends in electrical machines control: Samples for classical, sensorless, and fault-tolerant techniques," *IEEE Industrial Electronics Magazine*, vol. 8, no. 2, pp. 43–55, jun 2014. 35

[26] C. Liu, K. T. Chau, C. H. T. Lee, and Z. Song, "A critical review of advanced electric machines and control strategies for electric vehicles," *Proceedings of the IEEE*, vol. 109, no. 6, pp. 1004–1028, 2021. 35

[27] A. Mohammadpour and L. Parsa, "Global fault-tolerant control technique for multiphase permanent-magnet machines," *IEEE Transactions on Industry Applications*, vol. 51, no. 1, pp. 178–186, 2015. 35

[28] A. G. Yepes, O. Lopez, I. Gonzalez-Prieto, M. J. Duran, and J. Doval-Gandoy, "A comprehensive survey on fault tolerance in multiphase AC drives, part 1: General overview considering multiple fault types," *Machines*, vol. 10, no. 3, 2022. 35

[29] F. Barrero and J. Duran, "Recent advances in the design, modelling and control of multiphase machines —part I," *IEEE Transactions on Industrial Electronics*, vol. 63, no. 1, pp. 449–458, 2016. 35, 36, 37, 45, 63, 102

[30] M. J. Duran and F. Barrero, "Recent advances in the design, modeling, and control of multiphase machines—part II," *IEEE Transactions on Industrial Electronics*, vol. 63, no. 1, pp. 459–468, jan 2016. 35, 45, 102

[31] E. Levi, "Multiphase electric machines for variable-speed applications," *IEEE Transactions on Industrial Electronics*, vol. 55, no. 5, pp. 1893–1909, may 2008. 35, 96

[32] F. Locment, E. Semail, and F. Piriou, "Design and study of a multiphase axial-flux machine," *IEEE Transactions on Magnetics*, vol. 42, no. 4, pp. 1427–1430, apr 2006. 35, 55

[33] E. Levi, R. Bojoi, F. Profumo, H. Toliyat, and S. Williamson, "Multiphase induction motor drives – a technology status review," *IET Electric Power Applications*, vol. 1, no. 4, p. 489, 2007. 35, 45, 55

[34] A. Tessarolo, "Accurate computation of multiphase synchronous machine inductances based on winding function theory," *IEEE Transactions on Energy Conversion*, vol. 27, no. 4, pp. 895–904, Dec 2012. 35, 48

[35] M. Riera-Guasp, J. A. Antonino-Daviu, and G.-A. Capolino, "Advances in electrical machine, power electronic, and drive condition monitoring and fault detection: State of the art," *IEEE Transactions on Industrial Electronics*, vol. 62, no. 3, pp. 1746–1759, mar 2015. 35

[36] L. Parsa and H. Toliyat, "Fault-tolerant interior-permanent-magnet machines for hybrid electric vehicle applications," *IEEE Transactions on Vehicular Technology*, vol. 56, no. 4, pp. 1546–1552, jul 2007. 35, 36, 63

[37] H. A. Toliyat, M. M. Rahimian, and T. A. Lipo, "dq modeling of five phase synchronous reluctance machines including third harmonic of airgap mmf," in *Conference Record of the 1991 IEEE Industry Applications Society Annual Meeting*, 1991, pp. 231–237. 35, 45, 59

[38] Y. Hu, Y. Feng, and X. Li, "Fault-tolerant hybrid current control of dual three-phase PMSM with one phase open," *IEEE Journal of Emerging and Selected Topics in Power Electronics*, vol. 10, no. 3, pp. 3418–3426, 2022. 35

[39] R. Bojoi, A. Cavagnino, A. Tenconi, A. Tessarolo, and S. Vaschetto, "Multiphase electrical machines and drives in the transportation electrification," in *Proc. of the IEEE 1st International Forum on Research and Technologies for Society and Industry Leveraging a better tomorrow (RTSI)*, 2015. 35, 63

[40] M. Trabelsi, N. Nguyen, and E. Semail, "Real-time switches fault diagnosis based on typical operating characteristics of five-phase permanent magnetic synchronous machines," *IEEE Transactions on Industrial Electronics*, pp. 1–1, 2016. 35

[41] A. G. Yepes, I. Gonzalez-Prieto, O. Lopez, M. J. Duran, and J. Doval-Gandoy, "A comprehensive survey on fault tolerance in multiphase AC drives, part 2: Phase and switch open-circuit faults," *Machines*, vol. 10, no. 3, 2022. 35

[42] B. Aslan, J. Korecki, T. Vigier, and E. Semail, "Influence of Rotor Structure and Number of Phases on Torque and Flux Weakening Characteristics of V-Shape Interior PM Electrical Machine," *Journal of Energy and Power Engineering*, pp. 1461–1471, Sep. 2012. 35, 55

[43] H. Zahr, J. Gong, E. Semail, and F. Scuiller, "Comparison of optimized control strategies of a high-speed traction machine with five phases and

bi-harmonic electromotive force," *Energies*, vol. 9, no. 12, p. 952, nov 2016. 35, 36, 49, 67

[44] A. S. Abdel-Khalik, A. M. Massoud, and S. Ahmed, "An improved torque density pseudo six-phase induction machine using a quadruple three-phase stator winding," *IEEE Transactions on Industrial Electronics*, vol. 67, no. 3, pp. 1855–1866, 2020. 35

[45] Z. Liu, Y. Li, and Z. Zheng, "A review of drive techniques for multiphase machines," *CES Transactions on Electrical Machines and Systems*, vol. 2, no. 2, pp. 243–251, 2018. 36, 37

[46] W. Cao, B. Mecrow, G. Atkinson, J. Bennet, and D. Atkinson, "Overview of electric motor technologies used for more electric aircraft (MEA)," *IEEE Transactions on Industrial Electronics*, vol. 59, no. 9, pp. 3523–3531, sep 2012. 36

[47] L. Parsa and H. A. Toliyat, "Multi-phase permanent magnet motor drives," in *38th IAS Annual Meeting on Conference Record of the Industry Applications Conference, 2003.*, vol. 1, Oct 2003, pp. 401–408 vol.1. 36, 49, 58

[48] X. Kestelyn and E. Semail, "A vectorial approach for generation of optimal current references for multiphase permanent-magnet synchronous machines in real time," *IEEE Transactions on Industrial Electronics*, vol. 58, no. 11, pp. 5057–5065, nov 2011. 36

[49] S. Dwari and L. Parsa, "Fault-tolerant control of five-phase permanent-magnet motors with trapezoidal back EMF," *IEEE Transactions on Industrial Electronics*, vol. 58, no. 2, pp. 476–485, feb 2011. 36

[50] N. Bianchi, S. Bolognani, and M. Dai Pre, "Strategies for the fault-tolerant current control of a five-phase permanent-magnet motor," *IEEE Transactions on Industry Applications*, vol. 43, no. 4, pp. 960–970, 2007. 36

[51] H. Guzman, M. J. Duran, F. Barrero, B. Bogado, and S. Toral, "Speed control of five-phase induction motors with integrated open-phase fault operation using model-based predictive current control techniques," *IEEE Transactions on Industrial Electronics*, vol. 61, no. 9, pp. 4474–4484, 2014. 36

[52] J. Li, B. Du, T. Zhao, S. Wu, and S. Cui, "Current sensor fault-tolerant control for five-phase PMSM drives based on third-harmonic space," *IEEE Transactions on Industrial Electronics*, vol. 69, no. 10, pp. 9827–9837, 2022. 36

[53] G. Liu, Z. Lin, W. Zhao, Q. Chen, and G. Xu, "Third harmonic current injection in fault-tolerant five-phase permanent-magnet motor drive," *IEEE Transactions on Power Electronics*, vol. 33, no. 8, pp. 6970–6979, Aug 2018. 36, 49, 67

[54] M. Slunjski, M. Jones, and E. Levi, "Analysis of a symmetrical nine-phase machine with highly non-sinusoidal back-electromotive force," in *IECON 2018 - 44th Annual Conference of the IEEE Industrial Electronics Society*, Oct 2018, pp. 6229–6234. 36, 67

[55] M. Villani, M. Tursini, G. Fabri, and L. Castellini, "High reliability permanent magnet brushless motor drive for aircraft application," *IEEE Transactions on Industrial Electronics*, vol. 59, no. 5, pp. 2073–2081, may 2012. 36

[56] A. Sierra-González, E. Ibarra, I. Kortabarria, E. Trancho, and E. Otaola., "Real-time simulation platform of an EMA landing gear," in *Proc. of the 11th IET International Conference on Power Electronics, Machines and Drives (PEMD 2020)*, 2020, pp. 1–6. 36

[57] M. Jones, S. N. Vukosavic, D. Dujic, and E. Levi, "A synchronous current control scheme for multiphase induction motor drives," *IEEE Transactions on Energy Conversion*, vol. 24, no. 4, pp. 860–868, 2009. 36

[58] S. S. R. Bonthu, M. Z. Islam, A. Arafat, and S. Choi, "Five-phase external rotor permanent magnet assisted synchronous reluctance motor for in-wheel applications," in *Proc. of the IEEE Transportation Electrification Conference and Expo (ITEC)*, 2017. 36

[59] N. K. Nguyen, F. Meinguet, E. Semail, and X. Kestelyn, "Fault-tolerant operation of an open-end winding five-phase PMSM drive with short-circuit inverter fault," *IEEE Transactions on Industrial Electronics*, vol. 63, no. 1, pp. 595–605, 2016. 37

[60] L. Zhang, Y. Fan, R. D. Lorenz, A. Nied, and M. Cheng, "Design and comparison of three-phase and five-phase FTFSCW-IPM motor open-end

winding drive systems for electric vehicles applications," *IEEE Transactions on Vehicular Technology*, vol. 67, no. 1, pp. 385–396, 2018. 37

[61] L. Rovere, A. Formentini, G. L. Calzo, P. Zanchetta, and T. Cox, "Zero-sequence voltage elimination for dual-fed common DC-link open-end winding pmsm high-speed starter–generator—part i: Modulation," *IEEE Transactions on Industry Applications*, vol. 55, no. 6, pp. 7804–7812, 2019. 37

[62] K. Rajashekara and Y. Jia, "An induction generator based auxiliary power unit for power generation and management system for more electric aircraft," in *Proc. of the IEEE Energy Conversion Congress and Exposition (ECCE)*, 2016, pp. 1–7. 37

[63] D. Vizireanu, S. Brisset, X. Kestelyn, P. Brochet, Y. Milet, and D. Laloy, "Investigation on multi-star structures for large power direct-drive wind generator," *Electric Power Components and Systems*, vol. 35, no. 2, pp. 135–152, feb 2007. 37

[64] M. Benkhoris, *Control of the Double-star Synchronous Machine Supplied by PWM Inverters.* John Wiley & Sons, Ltd, 2012, ch. 4, pp. 125–159. 37, 77, 78, 82, 95, 100, 120

[65] R. H. Nelson and P. C. Krause, "Induction machine analysis for arbitrary displacement between multiple winding sets," *IEEE Transactions on Power Apparatus and Systems*, vol. PAS-93, no. 3, pp. 841–848, 1974. 37

[66] R. Bojoi, M. Lazzari, F. Profumo, and A. Tenconi, "Digital field oriented control for dual three-phase induction motor drives," in *Conference Record of the 2002 IEEE Industry Applications Conference. 37th IAS Annual Meeting (Cat. No.02CH37344)*, vol. 2, 2002, pp. 818–825 vol.2. 37

[67] D. Dujic, A. Iqbal, and E. Levi, "A space vector pwm technique for symmetrical six-phase voltage source inverters," *EPE Journal*, vol. 17, no. 1, pp. 24–32, 2007. [Online]. Available: https://doi.org/10.1080/09398368.2007.11463639 37

[68] W. N. W. A. Munim, M. J. Duran, H. S. Che, M. Bermúdez, I. González-Prieto, and N. A. Rahim, "A unified analysis of the fault tolerance capability in six-phase induction motor drives," *IEEE Transactions on Power Electronics*, vol. 32, no. 10, pp. 7824–7836, 2017. 37

[69] A. Salem and M. Narimani, "A review on multiphase drives for automotive traction applications," *IEEE Transactions on Transportation Electrification*, vol. 5, no. 4, pp. 1329–1348, 2019. 37, 63, 73

[70] European Union funded Project. (2019) FITGEN, Functionally integrated e-axle ready for mass market third generation electric vehicles. [Online]. Available: https://fitgen-project.eu/ 38

[71] S. S. Gjerde and T. Undeland, "Power conversion system for transformerless offshore wind turbine," in *Proceedings of the 2011 14th European Conference on Power Electronics and Applications*, 2011, pp. 1–10. 39, 121

[72] S. S. Gjerde, P. K. Olsen, and T. M. Undeland, "A transformerless generator-converter concept making feasible a 100 kV low weight offshore wind turbine part ii - the converter," in *2012 IEEE Energy Conversion Congress and Exposition (ECCE)*, 2012, pp. 253–260. 39

[73] S. S. Gjerde and T. M. Undeland, "A modular series connected converter for a 10 MW, 36 kV, transformer-less offshore wind power generator drive," *Energy Procedia*, vol. 24, pp. 68–75, 2012, selected papers from Deep Sea Offshore Wind R & D Conference, Trondheim, Norway, 19-20 January 2012. 39

[74] S. S. Gjerde, P. K. Olsen, K. Ljøkelsøy, and T. M. Undeland, "Control and fault handling in a modular series-connected converter for a transformerless 100 kV low-weight offshore wind turbine," *IEEE Transactions on Industry Applications*, vol. 50, no. 2, pp. 1094–1105, 2014. 39, 113, 121

[75] P. K. Olsen, S. Gjerde, R. M. Nilssen, J. Hoelto, and S. Hvidsten, "A transformerless generator-converter concept making feasible a 100 kV light weight offshore wind turbine: Part i - the generator," in *2012 IEEE Energy Conversion Congress and Exposition (ECCE)*, 2012, pp. 247–252. 39

[76] Z. Xiang-Jun, Y. Yongbing, Z. Hongtao, L. Ying, F. Luguang, and Y. Xu, "Modelling and control of a multi-phase permanent magnet synchronous generator and efficient hybrid 3L-converters for large direct-drive wind turbines," *IET Electric Power Applications*, vol. 6, pp. 322–331(9), July 2012. 39, 113, 120

[77] H. S. Che, W. P. Hew, N. A. Rahim, E. Levi, M. Jones, and M. J. Duran, "A six-phase wind energy induction generator system with series-connected DC-links," in *Proc. of the 3rd IEEE International Symposium*

on Power Electronics for Distributed Generation Systems (PEDG), 2012, pp. 26–33. 39, 120, 121

[78] H. S. Che, E. Levi, M. Jones, M. J. Duran, W.-P. Hew, and N. A. Rahim, "Operation of a six-phase induction machine using series-connected machine-side converters," *IEEE Transactions on Industrial Electronics*, vol. 61, no. 1, pp. 164–176, 2014. 39, 113, 117, 120, 121, 132

[79] S. M. Dabour, A. S. Abdel-Khalik, S. Ahmed, and A. M. Massoud, "A new dual series-connected nine-switch converter topology for a twelve-phase induction machine wind energy system," in *Proc. of the 11th IEEE International Conference on Compatibility, Power Electronics and Power Engineering (CPE-POWERENG)*, 2017, pp. 139–144. 39, 113, 120, 121

[80] S. Norrga, L. Jin, O. Wallmark, A. Mayer, and K. Ilves, "A novel inverter topology for compact EV and HEV drive systems," in *IECON 2013 - 39th Annual Conference of the IEEE Industrial Electronics Society*, 2013, pp. 6590–6595. 40

[81] M. Nikouie, O. Wallmark, L. Jin, L. Harnefors, and H.-P. Nee, "DC-link stability analysis and controller design for the stacked polyphase bridges converter," *IEEE Transactions on Power Electronics*, vol. 32, no. 2, pp. 1666–1674, 2017. 40, 113, 117, 120

[82] L. Jin, S. Norrga, O. Wallmark, and N. Apostolopoulos, "Communication-based distributed control of the stacked polyphase bridges converter," *IEEE Transactions on Industrial Electronics*, vol. 65, no. 2, pp. 1011–1020, 2018. 40, 120

[83] Y. Han, "Design, modeling, and control of multilevel converter motor drive with modular design and split winding machine," in *2014 IEEE 15th Workshop on Control and Modeling for Power Electronics (COMPEL)*, 2014, pp. 1–10. 40, 113, 132

[84] J. Wang, Y. Li, and Y. Han, "Evaluation and design for an integrated modular motor drive (IMMD) with GaN devices," in *2013 IEEE Energy Conversion Congress and Exposition*, 2013, pp. 4318–4325. 40

[85] H. Zhang, O. Wallmark, M. Leksell, S. Norrga, M. N. Harnefors, and L. Jin, "Machine design considerations for an MHF/SPB-converter based electric drive," in *Proc. of the 40th Annual Conference of the IEEE Industrial Electronics Society (IECON)*, 2014, pp. 3849–3854. 40, 132

[86] L. Jin, S. Norrga, O. Wallmark, and N. Apostolopoulos, "Modulation and power losses of a stacked polyphase bridge converter," *IEEE Journal of Emerging and Selected Topics in Power Electronics*, vol. 5, no. 1, pp. 409–418, 2017. 40

[87] D. White and H. Woodson, *Electromechanical Energy Conversion*, ser. [The M.I.T. core curriculum program in electrical engineering]. John Wiley & Sons, 1959. 45

[88] S. A. Nasar, "Electromechanical energy conversion in nm-winding double cylindrical structures in presence of space harmonics," *IEEE Transactions on Power Apparatus and Systems*, vol. PAS-87, no. 4, pp. 1099–1106, April 1968. 45, 51

[89] E. Klingshirn, "High phase order induction motors - part i-description and theoretical considerations," *IEEE Transactions on Power Apparatus and Systems*, vol. PAS-102, no. 1, pp. 47–53, jan 1983. 45, 59

[90] ——, "High phase order induction motors - part ii-experimental results," *IEEE Transactions on Power Apparatus and Systems*, vol. PAS-102, no. 1, pp. 54–59, jan 1983. 45, 59

[91] Y. Zhao and T. Lipo, "Space vector PWM control of dual three-phase induction machine using vector space decomposition," *IEEE Transactions on Industry Applications*, vol. 31, no. 5, pp. 1100–1109, 1995. 45, 55

[92] E. Semail, A. Bouscayrol, and J.-P. Hautier, "Vectorial formalism for analysis and design of polyphase synchronous machines," *The European Physical Journal Applied Physics*, vol. 22, no. 3, pp. 207–220, may 2003. 45, 50, 55, 56, 58

[93] L. Parsa and H. Toliyat, "Five-phase permanent-magnet motor drives," *IEEE Transactions on Industry Applications*, vol. 41, no. 1, pp. 30–37, jan 2005. 45, 49, 59, 60, 66

[94] A. Tessarolo, "Modeling and simulation of multiphase machines in the matlab/simulink environment," in *Engineering Education and Research Using MATLAB*. InTech, oct 2011. 45, 48, 50, 59, 62, 63, 77

[95] M. A. Rahman, *Power Electronics and Motor Drives*. CRC Press, 2016, ch. Permanent Magnet Machines, pp. 5–1, 5–10. 47, 48, 76

[96] R. M. Gray, "Toeplitz and circulant matrices: A review," *Foundations and Trends® in Communications and Information Theory*, vol. 2, no. 3, pp. 155–239, 2006. 48

[97] C. Concordia, *Synchronous machines: theory and performance*, ser. General Electric series.   Wiley, 1951. 48

[98] E. Levi, *Power Electronics and Motor Drives.*   CRC Press, 2016, ch. Multiphase AC Machines, pp. 3–1, 3–30. 48, 55, 56, 77

[99] F. Yu, X. Zhang, and S. Wang, "Five-phase permanent magnet synchronous motor vector control based on harmonic eliminating space vector modulation," in *2005 International Conference on Electrical Machines and Systems.*   IEEE, 2005. 48

[100] E. Semail, X. Kestelyn, and A. Bouscayrol, "Sensitivity of a 5-phase brushless DC machine to the 7th harmonic of the back-electromotive force," in *IEEE 35th Annual Power Electronics Specialists Conference (IEEE Cat. No.04CH37551).*   IEEE, 2004. 49, 55, 58

[101] ——, "Right harmonic spectrum for the back-electromotive force of a n-phase synchronous motor," in *Conference Record of the 2004 IEEE Industry Applications Conference, 2004. 39th IAS Annual Meeting.*   IEEE, 2004. 49, 55, 58

[102] X. Kestelyn and E. Semail, "Vectorial modeling and control of multiphase machines with non-salient poles supplied by an inverter," in *Control of Non-conventional Synchronous Motors*, J.-P. Louis, Ed.   John Wiley & Sons, Inc, feb 2013, pp. 161–206. 50, 55, 56, 58, 78

[103] A. Tessarolo, "On the modeling of poly-phase electric machines through vector-space decomposition: Theoretical considerations," in *2009 International Conference on Power Engineering, Energy and Electrical Drives.*   IEEE, mar 2009. 50, 55, 59

[104] P. Vas, *Vector Control of AC Machines (Monographs in Electrical and Electronic Engineering).*   Oxford University Press, 1990. 55, 96

[105] A. Tessarolo, "On the modeling of poly-phase electric machines through vector-space decomposition: Numeric application cases," in *International Conference on Power Engineering, Energy and Electrical Drives.*   IEEE, mar 2009. 55, 59

[106] O. Dordevic, E. Levi, and M. Jones, "A vector space decomposition based space vector PWM algorithm for a three-level seven-phase voltage source inverter," *IEEE Transactions on Power Electronics*, vol. 28, no. 2, pp. 637–649, feb 2013. 55

[107] J. Kelly, E. Strangas, and J. Miller, "Multiphase space vector pulse width modulation," *IEEE Transactions on Energy Conversion*, vol. 18, no. 2, pp. 259–264, jun 2003. 55

[108] J. Figueroa, J. Cros, and P. Viarouge, "Generalized transformations for polyphase phase-modulation motors," *IEEE Transactions on Energy Conversion*, vol. 21, no. 2, pp. 332–341, jun 2006. 55, 59

[109] A. Tessarolo, L. Branz, and M. Bortolozzi, "Stator inductance matrix diagonalization algorithms for different multi-phase winding schemes of round-rotor electric machines part ii. examples and validations," in *IEEE EUROCON 2015 - International Conference on Computer as a Tool (EUROCON)*, Sept 2015, pp. 1–6. 55

[110] ——, "Stator inductance matrix diagonalization algorithms for different multi-phase winding schemes of round-rotor electric machines part i. theory," in *IEEE EUROCON 2015 - International Conference on Computer as a Tool (EUROCON)*, Sept 2015, pp. 1–6. 55

[111] X. Kestelyn, E. Semail, and J. Hautier, "Vectorial multi-machine modeling for a five-phase machine," in *International Congress on Electrical Machines (ICEM'02)*, 2002. 55

[112] E. Semail, X. Kestelyn, and F. Locment, "Fault tolerant multiphase electrical drives: the impact of design," in *IET Colloquium on Reliability of Electromagnetic Systems*. IEE, 2007. 55

[113] X. Kestelyn, F. Locment, Y. Crevits, and E. Semail, "Easy-to-implement integral numerical simulation of multi-phase drives under fault supply condition," in *2007 IEEE International Electric Machines & Drives Conference*. IEEE, may 2007. 55

[114] F. Locment, E. Semail, and X. Kestelyn, "Vectorial approach-based control of a seven-phase axial flux machine designed for fault operation," *IEEE Transactions on Industrial Electronics*, vol. 55, no. 10, pp. 3682–3691, oct 2008. 55

[115] H. Zahr, E. Semail, and F. Sciuller, "Five-phase version of 12 slots/8 poles three-phase synchronous machine for marine-propulsion," in *2014 IEEE Vehicle Power and Propulsion Conference (VPPC)*.   IEEE, oct 2014. 55

[116] F. Sciuller and E. Semail, "Inductances and back-EMF harmonics influence on the torque/speed characteristic of five-phase SPM machine," in *2014 IEEE Vehicle Power and Propulsion Conference (VPPC)*.   IEEE, oct 2014. 55

[117] F. Sciuller, H. Zahr, and E. Semail, "Maximum reachable torque, power and speed for five-phase SPM machine with low armature reaction," *IEEE Transactions on Energy Conversion*, vol. 31, no. 3, pp. 959–969, sep 2016. 55

[118] K.-T. Tang, *Mathematical Methods for Engineers and Scientists 1, Complex Analysis, Determinants and Matrices*.   Springer Berlin Heidelberg, 2006. 55

[119] A. A. Rockhill and T. A. Lipo, "A generalized transformation methodology for polyphase electric machines and networks," in *2015 IEEE International Electric Machines & Drives Conference (IEMDC)*.   IEEE, may 2015. 56

[120] E. Clarke, "Circuit analysis of AC systems, symmetrical and related components," *General Electric Co., Schenectady, New York*, 1950. 57

[121] S. Kallio, "Modeling and parameter estimation of double-star permanent magnet synchronous machines," phdthesis, Lappeenranta University of Technology, 2014. 57

[122] M. Cheng, F. Yu, K. T. Chau, and W. Hua, "Dynamic performance evaluation of a nine-phase flux-switching permanent-magnet motor drive with model predictive control," *IEEE Transactions on Industrial Electronics*, vol. 63, no. 7, pp. 4539–4549, jul 2016. 59

[123] L. Parsa and H. Toliyat, "Five-phase permanent magnet motor drives for ship propulsion applications," in *IEEE Electric Ship Technologies Symposium, 2005*.   IEEE, 2005. 66

[124] S. Kallio, M. Andriollo, A. Tortella, and J. Karttunen, "Decoupled $d - q$ model of double-star interior-permanent-magnet synchronous machines," *IEEE Transactions on Industrial Electronics*, vol. 60, no. 6, pp. 2486–2494, 2013. 73, 77, 78, 79, 94, 102, 104

[125] J. Karttunen, S. Kallio, P. Peltoniemi, P. Silventoinen, and O. Phyronen, "Decoupled vector control scheme for dual three-phase permanent magnet synchronous machines," *IEEE Transactions on Industrial Electronics*, vol. 61, no. 5, pp. 2185–2196, 2014. 77, 78, 79, 94, 102, 104, 120

[126] Y. Hu, Z. Q. Zhu, and M. Odavic, "Comparison of two-individual current control and vector space decomposition control for dual three-phase PMSM," *IEEE Transactions on Industry Applications*, vol. 53, no. 5, pp. 4483–4492, 2017. 78, 82, 94, 95, 100, 102, 104, 120

[127] A. Sierra-Gonzalez, P. Pescetto, E. Trancho, E. Ibarra, G. Pellegrino, and F. Alvarez-Gonzalez, "Control of dual three-phase IPMSM drive with cascaded DC-link capacitors for third generation EV," in *Proc. of the IEEE Energy Conversion Congress and Exposition (ECCE)*, 2021, pp. 4822–4829. 80, 84, 100

[128] J. Karttunen, S. Kallio, P. Peltoniemi, P. Silventoinen, and O. Pyrhonen, "Dual three-phase permanent magnet synchronous machine supplied by two independent voltage source inverters," in *Proc. of the International Symposium on Power Electronics Power Electronics, Electrical Drives, Automation and Motion (SPEEDAM)*, 2012, pp. 741–747. 82, 84, 100, 120

[129] E. Trancho, E. Ibarra, A. Arias, C. Salazar, I. Lopez, A. D. de Guereñu, and A. Peña, "IPMSM torque control strategies based on LUTs and VCT feedback for robust control under machine parameter variations," in *IECON 2016 - 42nd Annual Conference of the IEEE Industrial Electronics Society*, 2016, pp. 2833–2838. 86, 87

[130] S. Xiao and A. Griffo, "PWM-based flux linkage and rotor temperature estimations for permanent magnet synchronous machines," *IEEE Transactions on Power Electronics*, vol. 35, no. 6, pp. 6061–6069, 2020. 86

[131] E. Trancho, "Field weakening and sensorless control solutions for synchronous machines applied to electric vehicles," Ph.D. dissertation, University of the Basque Country, 2018. 86, 87

[132] E. Armando, R. Bojoi, P. Guglielmi, G. Pellegrino, and M. Pastorelli, "Experimental identification of the magnetic model of synchronous machines," *IEEE Transactions on Industry Applications*, vol. 49, no. 5, pp. 2116–2125, 2013. 92

[133] P. Pescetto and G. Pellegrino, "Sensorless magnetic model and PM flux identification of synchronous drives at standstill," in *Proc. of the IEEE International Symposium on Sensorless Control for Electrical Drives (SLED)*, 2017, pp. 79–84. 92

[134] S. A. Odhano, P. Pescetto, H. A. A. Awan, M. Hinkkanen, G. Pellegrino, and R. Bojoi, "Parameter identification and self-commissioning in AC motor drives: A technology status review," *IEEE Transactions on Power Electronics*, vol. 34, no. 4, pp. 3603–3614, 2019. 92

[135] A. Visioli, *Practical PID Control*, ser. Advances in Industrial Control. Springer London, 2006. 96

[136] A. Tapia, G. Tapia, J. Ostolaza, and J. Saenz, "Modeling and control of a wind turbine driven doubly fed induction generator," *IEEE Transactions on Energy Conversion*, vol. 18, no. 2, pp. 194–204, 2003. 96

[137] K. Åström and R. Murray, *Feedback Systems: An Introduction for Scientists and Engineers, Second Edition*. Princeton University Press, 2021. 96, 122

[138] S. Kouro, J. Leon, L. Franquelo, J. Rodriguez, and B. Wu, *DC-AC converters*. CRC Press, 2016, ch. 14, pp. 1–49. 96, 97, 98

[139] D. G. Holmes and T. A. Lipo, *Modulation of Three Phase Voltage Source Inverters*. IEEE, 2003, ch. 5, pp. 215–257. 96, 97

[140] S.-H. Kim, "Chapter 7 - Pulse width modulation inverters," in *Electric Motor Control*, S.-H. Kim, Ed. Elsevier, 2017, pp. 265–340. 96, 98

[141] R. Bojoi, A. Tenconi, F. Profumo, G. Griva, and D. Martinello, "Complete analysis and comparative study of digital modulation techniques for dual three-phase AC motor drives," in *Proc. of the 33rd Annual IEEE Power Electronics Specialists Conference (Cat. No.02CH37289)*, vol. 2, 2002, pp. 851–857. 96, 142

[142] S. Sue and C. Pan, "Voltage-constraint-tracking-based field-weakening control of IPM synchronous motor drives," *IEEE Transactions on Industrial Electronics*, vol. 55, no. 1, pp. 340–347, Jan 2008. 96

[143] T. Schoenen, A. Krings, D. van Treek, and R. De Doncker, "Maximum DC-link voltage utilization for optimal operation of IPMSM," in *IEEE*

International Elctric Machines and Drives Conference, 2009, pp. 1547–1550. 97, 114

[144] J. A. Houldsworth and D. A. Grant, "The use of harmonic distortion to increase the output voltage of a three-phase PWM inverter," *IEEE Transactions on Industry Applications*, vol. IA-20, no. 5, pp. 1224–1228, 1984. 97

[145] E. Levi, F. Barrero, and M. J. Duran, "Multiphase machines and drives - revisited," *IEEE Transactions on Industrial Electronics*, vol. 63, no. 1, pp. 429–432, jan 2016. 102

[146] M. De Gennaro, P. Scheuermann, T. Wellerdieck, V. Ravello, G. Pellegrino, and E. Trancho, "The H2020 project FITGEN: preliminary results and design guidelines of an integrated e-axle for the third-generation electric vehicles," in *Proc. of the 8th Transport Research Arena (TRA)*, 2020, pp. 1–10. 111

[147] J. O. Estima and A. J. Marques Cardoso, "Efficiency analysis of drive train topologies applied to electric/hybrid vehicles," *IEEE Transactions on Vehicular Technology*, vol. 61, no. 3, pp. 1021–1031, 2012. 114, 115

[148] T. Schoenen, M. S. Kunter, M. D. Hennen, and R. W. De Doncker, "Advantages of a variable DC-link voltage by using a DC-DC converter in hybrid-electric vehicles," in *2010 IEEE Vehicle Power and Propulsion Conference*, 2010, pp. 1–5. 114, 115

[149] J. Kacetl, J. Fang, T. Kacetl, N. Tashakor, and S. Goetz, "Design and analysis of modular multilevel reconfigurable battery converters for variable bus voltage powertrains," *IEEE Transactions on Power Electronics*, vol. 38, no. 1, pp. 130–142, 2023. 114, 115

[150] P. Pescetto, A. Sierra-Gonzalez, E. Trancho, and G. Pellegrino, "Variable DC-link control strategy for maximum efficiency of traction motor drives," in *Proc. of the IEEE Energy Conversion Congress and Exposition (ECCE)*, 2021, pp. 4815–4821. 114, 115, 129

[151] H. Chen, H. Kim, R. Erickson, and D. Maksimović, "Electrified automotive powertrain architecture using composite DC–DC converters," *IEEE Transactions on Power Electronics*, vol. 32, no. 1, pp. 98–116, 2017. 114, 115

[152] K. K. Prabhakar, M. Ramesh, A. Dalal, C. U. Reddy, A. K. Singh, and P. Kumar, "Efficiency investigation for electric vehicle powertrain with variable DC-link bus voltage," in *IECON 2016 - 42nd Annual Conference of the IEEE Industrial Electronics Society*, 2016, pp. 1796–1801. 114, 115

[153] W. Qian, H. Cha, F. Z. Peng, and L. M. Tolbert, "55-kW variable 3X DC-DC converter for plug-in hybrid electric vehicles," *IEEE Transactions on Power Electronics*, vol. 27, no. 4, pp. 1668–1678, 2012. 115

[154] J. Kolar and S. Round, "Analytical calculation of the RMS current stress on the DC-link capacitor of voltage-PWM converter systems," *IEE Proceedings - Electric Power Applications*, vol. 153, pp. 535–543(8), July 2006. 116

[155] X. Pei, W. Zhou, and Y. Kang, "Analysis and calculation of DC-link current and voltage ripples for three-phase inverter with unbalanced load," *IEEE Transactions on Power Electronics*, vol. 30, no. 10, pp. 5401–5412, 2015. 116

[156] V. Blasko, "Analysis of a hybrid PWM based on modified space-vector and triangle-comparison methods," *IEEE Transactions on Industry Applications*, vol. 33, no. 3, pp. 756–764, 1997. 132

[157] Y. Huang, Y. Xu, W. Zhang, and J. Zou, "PWM frequency noise cancellation in two-segment three-phase motor using parallel interleaved inverters," *IEEE Transactions on Power Electronics*, vol. 34, no. 3, pp. 2515–2525, 2019. 132

[158] K. Cui, C. Wang, M. Zhou, and S. Sun, "Comprehensive investigation of space-vector PWM including novel switching sequences for dual three-phase motor drives," *IEEE Transactions on Transportation Electrification*, pp. 1–1, 2022. 132

[159] Y. Miyama, M. Ishizuka, H. Kometani, and K. Akatsu, "Vibration reduction by applying carrier phase-shift PWM on dual three-phase windings permanent-magnet synchronous motor," in *Proc. of the IEEE International Electric Machines and Drives Conference (IEMDC)*, 2017, pp. 1–6. 132

[160] Y. Miyama and K. Akatsu, "Dual three-phase-winding permanent-magnet synchronous motors: An investigation of the optimal carrier phase-shift

angle," *IEEE Industry Applications Magazine*, vol. 27, no. 6, pp. 12–21, 2021. 132

[161] K. T. Nagaoka, K. O. Nagaoka, and T. Kanmachi, "Fine servo system based on new over-modulation with priority given to d-axis voltage for IPMSM," in *IECON Proc. of the 36th Annual Conference on IEEE Industrial Electronics Society*, 2010, pp. 2230–2235. 182

[162] Q. Wang, H. Yu, M. Wang, and X. Qi, "An improved sliding mode control using disturbance torque observer for permanent magnet synchronous motor," *IEEE Access*, vol. 7, pp. 36 691–36 701, 2019. 183

[163] J. Liu, H. Li, and Y. Deng, "Torque ripple minimization of PMSM based on robust ILC via adaptive sliding mode control," *IEEE Transactions on Power Electronics*, vol. 33, no. 4, pp. 3655–3671, 2018. 183

[164] V. Repecho, D. Biel, and A. Arias, "Fixed switching period discrete-time sliding mode current control of a PMSM," *IEEE Transactions on Industrial Electronics*, vol. 65, no. 3, pp. 2039–2048, 2018. 184, 185

[165] V. Utkin, J. Guldner, and J. Shi, *Sliding mode control in electromechanical systems*. CRC Press, 2009. 184, 186

[166] V. Repecho, J. Waqar, D. Biel, and A. Doria-Cerezo, "Zero speed sensorless scheme for permanent magnet synchronous machine under decoupled sliding-mode control," *IEEE Transactions on Industrial Electronics*, vol. 69, no. 2, pp. 1288–1297, 2022. 185